12-2011

Modeling of a novel solar down beam test facility utilizing Newtonian optics

Ryan J. Hoffmann
University of Nevada, Las Vegas

Repository Citation

Hoffmann, Ryan J., "Modeling of a novel solar down beam test facility utilizing Newtonian optics" (2011). *UNLV Theses, Dissertations, Professional Papers, and Capstones*. 1397.
https://digitalscholarship.unlv.edu/thesesdissertations/1397

MODELING OF A NOVEL SOLAR DOWN BEAM TEST FACILITY UTILIZING NEWTONIAN OPTICS

By

Ryan J Hoffmann

A thesis submitted in partial fulfillment
of the requirements for the

Master of Science Degree in Mechanical Engineering

Department of Mechanical Engineering
Howard R. Hughes College of Engineering
The Graduate College

University of Nevada, Las Vegas
December 2011

THE GRADUATE COLLEGE

We recommend the thesis prepared under our supervision by

Ryan J. Hoffmann

entitled

Modeling of a Novel Solar Down Beam Test Facility Utilizing Newtonian Optics

be accepted in partial fulfillment of the requirements for the degree of

Master of Science in Mechanical Engineering
Department of Mechanical Engineering

Yi Tung Chen, Committee Chair

Robert Boehm, Committee Member

Suresh Sadineni, Committee Member

Allen Johnson, Graduate College Representative

Ronald Smith, Ph. D., Vice President for Research and Graduate Studies
and Dean of the Graduate College

December 2011

ABSTRACT

Modeling of a Novel Solar Down Beam Test Facility Utilizing Newtonian Optics

by

Ryan Hoffmann

Dr. Yitung Chen, Examination Committee Chair
Professor of Department of Mechanical Engineering
University of Nevada, Las Vegas

As advances in concentrated solar energy progress there will inevitably be an increase in the demand of resources for testing new conceptions. Currently, there are limited facilities available for taking concentrated solar energy concepts from the laboratory bench scale to the engineering test scale. A proposed solution is a scientific and developmental facility that provides highly concentrated solar energy at ground level. The design presented is a solar down beam test facility utilizing a Newtonian optics approach with a flat rectangular down beam mirror to reflect and concentrate the sun's rays at ground level.

Literature review suggests a hyperbolic reflector implementation for down beam reflector systems. An alternative Newtonian design uses a planar mirror to direct converging light from the heliostat field to a convenient focus at ground level. A flat mirror has the advantage of relatively cheap construction, and the intrinsic capability to host multiple experiments. Additionally, in comparison to a convex down beam mirror, there is significantly less optical distortion of the solar energy collected on a solar receiver at the top of a tower. The Newtonian design inherently preserves the focus of the heliostat field, mimicking the behavior of tower top geometry. The planar mirror

geometry simply reflects the rays to ground level, and thus has little effect on the achievable concentration ratio other than the additional reflective losses.

The presented work focuses on the optical analysis and modeling of such a novel test facility. System examination was accomplished utilizing the commercially available ray tracing software Advanced Systems Analysis Program (ASAP®). ASAP® is able to simulate the interaction of the sun's rays with the designed optical system by utilizing Monte Carlo ray tracing techniques. This allowed for all optical losses to be simulated within the model; including cosine, blocking, shadowing, attenuation, and reflective losses.

In order to achieve a high level of concentration with a planar down beam reflector, converging heliostats were utilized. Parallel rays were implemented to identify the focusing conditions of the heliostats. A realistic sun source was developed within ASAP® to simulate the maximum 0.5° angular divergence characteristics of the sun's rays. This allowed for practical concentration ratios to be simulated within the model. Algorithms were developed and implemented in MATLAB® to properly simulate the sun's position as well as the heliostat field layout and orientation for any given hour of the year. A Sun Position Orientation (SPO) algorithm was constructed to determine the relative location of the sun source for any given hour within the ASAP® model. A Heliostat Reflection Orientation Position Vector (HROPV) algorithm was developed to properly orientate each heliostat to reflect to the proper aim point (AP) of the heliostat filed. Additionally, a North-South Cornfield Heliostat Field Layout (NSCHFL) algorithm was established to tightly pack heliostats within the utilizable range of the down beam reflector.

Utilizing a tightly packed North-South (N-S) cornfield heliostat field layout the optical performance of the facility was demonstrated for a day in each of the four seasons, providing a general performance trend over the course of the year. Extensive ray tracing establishes the achievability of the targeted 1MW, 1,000 suns concentration at ground level for several hours of the day over the course of the year. Furthermore, the simulation results demonstrate nearly 2 MW and 4,000 suns concentration is achievable for optimal orientation hours in which the tower, sun, and center of the heliostat field are all co-linear.

Future system analysis should examine modifications of optical geometry parameters such as heliostat dimensions, heliostat field layouts, and down beam reflector heights as well as orientations. Additionally, the effect of varying focal points needs to be investigated. The implications of heliostat pointing inaccuracies should also be accounted for.

ACKNOWLEDGMENTS

I would like to express my sincere gratitude and appreciation to Dr. Yitung Chen for his guidance and efforts during the course of the research presented. Dr. Chen’s work ethic and technical competency is admirable. Without his support and encouragement this work would never have been completed. Furthermore, the amount of time and effort that Dr. Chen put into reviewing and contributing to the work presented will never be forgotten. When I first came to UNLV Dr. Chen took me under his wing and provided me with an opportunity that would never have been available to me without his consideration. For that I am forever grateful.

I would also like to express the utmost appreciation to Dr. Allen Johnson. His ingenuity and motivation behind the development of such a facility is what allowed this research to come to fruition. Dr. Johnson has been a source of moral, technical, and financial support throughout the course of the work presented. He has been a mentor during my time here at UNLV. Without Dr. Johnson’s guidance this work could never have been completed. His efforts will never be forgotten.

I am also extremely thankful to Dr. Robert Boehm for his refined passion in ongoing endeavors of renewable energy research at UNLV. The courses that I have taken from Dr. Boehm have greatly contributed to my ability to perform the work presented. Specifically, the knowledge gained from the course entitled ‘Computational Aspects of Solar Energy’ is what allowed me to develop an approach to modeling of the facility.

I also wish to acknowledge Dr. Suresh Sadineni for his efforts in being a committee member, and offering valuable insight during my course of study at UNLV.

Additionally, I wish to acknowledge my colleagues at UNLV, both in the Center for Energy Research lab and at the Harry Reid Center. They have made my experience at UNLV an enjoyable one, and created a collaborative working environment that will always be appreciated.

Furthermore, I wish to thank my friends and family for their ongoing support and encouragement during my time at UNLV and over the course of the research presented.

I dedicate this thesis to Abby Jo Morlock for her continual support and confidence in me.

TABLE OF CONTENTS

ABSTRACT iii
ACKNOWLEDGMENTS vi
TABLE OF CONTENTS viii
LIST OF TABLES xi
LIST OF FIGURES xii
CHAPTER 1 INTRODUCTION 1
  1.1 Motivation 1
  1.2 Concentrated Solar Power 2
    1.2.1 Technology Overview 2
    1.2.2 Linear Concentrator Systems 6
    1.2.3 Dish/Engine Systems 9
    1.2.4 Solar Power Towers 10
  1.3 Tower Reflector Systems 14
    1.3.1 Concept Overview 14
    1.3.2 Optics of Down Beam Towers 16
    1.3.3 Weizmann Institute 19
    1.3.4 Masdar Tower 23
  1.4 Thesis Incentive and Scope 24
CHAPTER 2 FACILITY DESCRIPTION AND DESIGN 27
  2.1 Conceptual Design 27
  2.2 Targeted Output 29
  2.3 Site Details 31
    2.3.1 Reflector Design 31
    2.3.2 Tower Design 32
    2.3.3 Heliostat Field 35
    2.3.4 Ground Collector Element 38
    2.3.5 Utilities 39
    2.3.6 Land Specifications 40
CHAPTER 3 MODELING THE NCSETF 42
  3.1 Modeling Approach 42

3.2 Software and Modeling Tools 43

3.2.1 MATLAB® 43

3.2.2 ASAP® 43

3.2.3 TMY Weather Data 45

3.3 Simulating the Sun 47

3.3.1 Sun's Position 47

3.3.2 Modeling the Sun's Rays 50

3.3.3 Realistic Solar Disk 53

3.4 Optical Geometry 56

3.4.1 Down Beam Reflector 56

3.4.2 Heliostats 59

3.5 Heliostat Reflection Equations 61

3.6 Converging Heliostats 67

3.7 Heliostat Field Layouts 71

3.7.1 Methodology 71

3.7.2 Radially Staggered Heliostat Field Layout (RSHFL) Algorithm 72

3.7.3 N-S Cornfield Heliostat Field Layout (NSCHFL) Algorithm 74

3.8 Algorithm Integration 77

CHAPTER 4 SIMULATION RESULTS & DISCUSSION 80

4.1 DNI Model Validation 80

4.2 Simulation DNI Data 83

4.3 Radially Staggered Simulations with Parallel Rays 85

4.4 N-S Cornfield Simulations with Parallel Rays 89

4.4.1 Presentation Overview 89

4.4.2 TMY3 July 12, 1991 Simulation 89

4.4.3 TMY3 September 23, 1987 Simulation 93

4.4.4 TMY3 December 22, 1979 95

4.4.5 TMY3 March 22, 1982 97

4.4.6 Time Dependent Results 101

4.5 N-S Cornfield Simulations with Realistic Solar Disk 104

4.5.1 Sun Source Verification 104

4.5.2 Presentation Overview 105
4.5.3 TMY3 July 12, 1991 Simulation 106
4.5.4 TMY3 September 23, 1987 Simulation 109
4.5.5 TMY3 December 22, 1979 112
4.5.6 TMY3 March 22, 1982 114
4.5.7 Time Dependent Results 116
4.6 Observations of Simulations 124
CHAPTER 5 CONCLUSION & CONTINUING WORK 127
5.1 Conclusion 127
5.2 Model Improvements 128
5.3 Future System Analysis 129
APPENDIX A 131
APPENDIX B 134
APPENDIX C 137
APPENDIX D 140
REFERENCES 143
VITA 148

LIST OF TABLES

Table 1.1 Performance data of various CSP technologies [1] 6
Table 4.1 Statistical data of DNI gauging simulation... 81
Table 4.2 TMY3 hourly DNI (W/m^2) for simulation days of NCSETF........................... 84
Table 4.3 Simulated power output (W) for N-S cornfield algorithm 101
Table 4.4 Simulated power output (W): N-S cornfield with diverging rays 117
Table 4.5 Simulated concentration range (W/m^2): Diverging rays................................. 120
Table 4.6 Simulated detector center concentration (W/m^2): Diverging rays.................. 121

LIST OF FIGURES

Figure 1.1 Concentrating solar power prospects for southwest United States [4] 3
Figure 1.2 Theoretical efficiency of CSP systems for generating mechanical work [1] 5
Figure 1.3 Parabolic trough single-axis tracking operation schematic [7] 7
Figure 1.4 Parabolic trough power plant schematic incorporating thermal storage [8]...... 8
Figure 1.5 Linear Fresnel reflector power plant schematic [9].. 9
Figure 1.6 Dish/engine power system [10] 10
Figure 1.7 Central receiver power tower system [12].. 11
Figure 1.8 External receiver utilized at Solar One facility in Barstow, CA [13]............. 12
Figure 1.9 Cavity central receiver with four apertures [13]... 13
Figure 1.10 Solar tower reflector optical overview: (a) hyperbolic mirror; (b) elliptical mirror [17] 16
Figure 1.11 Effects of translating TR height for hyperbolic (a)-(b) and elliptical (c)-(d) down beam mirror [17].. 18
Figure 1.12 (a) Shifting of hyperbolic mirror to favor northern heliostat field; (b) shifting of elliptical mirror to favor northern heliostat field [17]............... 19
Figure 1.13 Solar down beam facility at Weizmann Institute of Science [19]................. 20
Figure 1.14 Top of tower at Weizmann Institute of Science [19] 21
Figure 1.15 Description of hyperbolic multi-faceted down beam mirror at Weizmann Institute of Science [19] 22
Figure 1.16 Down beam demo facility in Masdar, Abu Dhabi [22] 23
Figure 2.1 NCSETF site layout utilizing temporary infrastructure 28
Figure 2.2 Steel lattice truss tower design for NCSETF.. 33
Figure 2.3 NCSETF schematic with 3 column tower 35
Figure 2.4 Cosine losses as applied to extraterrestrial horizontal irradiance.................... 36
Figure 2.5 Site plan for proposed NCSETF... 41
Figure 3.1 Solar zenith angle, θ_z, and solar azimuth angle, γ_s [29] 48
Figure 3.2 Divergence characteristics of solar rays 53
Figure 3.3 ASAP® scattering surface for diverging solar rays 55
Figure 3.4 Optical geometry for NSCETF down beam reflector [unit: m] 58
Figure 3.5 Trapezoid demonstrating utilizable placement of heliostats 60
Figure 3.6 Plane of reflection for heliostats [31] 61
Figure 3.7 Vector position geometry for target, heliostat, and sun.................................. 62
Figure 3.8 Triangle in spherical coordinates [31].. 63
Figure 3.9 Spherical triangles created by heliostat, sun, and target position vectors 64
Figure 3.10 Non-imaging focusing heliostat schematic [33]... 68
Figure 3.11 Faceted converging heliostat ASAP® schematic.. 69
Figure 3.12 Ray trace demonstrating converging heliostats in ASAP® 71
Figure 3.13 Radially staggered configuration [35] 72
Figure 3.14 RSHFL algorithm prompt and heliostat field layout.................................... 74
Figure 3.15 NSCHFL algorithm prompt and heliostat field layout 76
Figure 3.16 Refined N-S cornfield (a) heliostat field layout; (b) ray trace....................... 77
Figure 3.17 Algorithm flow chart for simulating NCSETF... 79
Figure 4.1 (a) 2D DNI gauging contour plot; (b) 3D DNI gauging irradiance plot 82

Figure 4.2 TMY3 DNI for NCSETF simulation hours 85
Figure 4.3 NCSETF ray trace utilizing radially staggered heliostat field layout 86
Figure 4.4 (a) 2D collector irradiance plot; (b) 3D collector irradiance plot 87
Figure 4.5 (a) Detector contour plot; (b) Isometric distribution of flux plot 88
Figure 4.6 NCSETF ray trace utilizing N-S cornfield with parallel rays 90
Figure 4.7 NCSETF July 12, 12:00 p.m. (a) Detector insolation plot; (b) Detector contour plot 91
Figure 4.8 NCSETF July 12, 9:00 a.m. (a) Detector insolation plot; (b) Detector contour plot 91
Figure 4.9 NCSETF July 12, 4:00 p.m. (a) Detector insolation plot; (b) Detector contour plot 92
Figure 4.10 NCSETF Sept 23, 9:00 a.m. (a) Detector insolation plot; (b) Detector contour plot 93
Figure 4.11 NCSETF Sept 23, 12:00 p.m. (a) Detector insolation plot; (b) Detector contour plot 94
Figure 4.12 NCSETF Sept 23, 4:00 p.m. (a) Detector insolation plot; (b) Detector contour plot 94
Figure 4.13 NCSETF Dec 22, 9:00 a.m. (a) Detector insolation plot; (b) Detector contour plot 95
Figure 4.14 NCSETF Dec 22, 12:00 p.m. (a) Detector insolation plot; (b) Detector contour plot 96
Figure 4.15 NCSETF Dec 22, 4:00 p.m. (a) Detector insolation plot; (b) Detector contour plot 96
Figure 4.16 NCSETF March 22, 9:00 a.m. (a) Detector insolation plot; (b) Detector contour plot 98
Figure 4.17 NCSETF March 22, 12:00 p.m. (a) Detector insolation plot; (b) Detector contour plot 98
Figure 4.18 NCSETF March 22, 4:00 p.m. (a) Detector insolation plot; (b) Detector contour plot 99
Figure 4.19 Optical coma due to off-axis light source [37] 100
Figure 4.20 Simulated power output: N-S cornfield with parallel rays 102
Figure 4.21 Simulated optical efficiency: N-S cornfield with parallel rays 103
Figure 4.22 Single heliostat sun spot: Focal length = 125.6 m 105
Figure 4.23 NCSETF ray trace utilizing NSCHFL algorithm with diverging rays 106
Figure 4.24 NCSETF July 12, 12:00 p.m. (a) Detector insolation plot; (b) Detector contour plot 107
Figure 4.25 NCSETF July 12, 9:00 a.m. (a) Detector insolation plot; (b) Detector contour plot 108
Figure 4.26 NCSETF July 12, 4:00 p.m. (a) Detector insolation plot; (b) Detector contour plot 108
Figure 4.27 NCSETF Sept 23, 9:00 a.m. (a) Detector insolation plot; (b) Detector contour plot 110
Figure 4.28 NCSETF Sept 23, 12:00 p.m. (a) Detector insolation plot; (b) Detector contour plot 110
Figure 4.29 NCSETF Sept 23, 4:00 p.m. (a) Detector insolation plot; (b) Detector contour plot 111

Figure 4.30 NCSETF Dec 22, 9:00 a.m. (a) Detector insolation plot; (b) Detector contour plot........ 112
Figure 4.31 NCSETF Dec 22, 12:00 p.m. (a) Detector insolation plot; (b) Detector contour plot........ 113
Figure 4.32 NCSETF Dec 22, 4:00 p.m. (a) Detector insolation plot; (b) Detector contour plot........ 113
Figure 4.33 NCSETF March 22, 9:00 a.m. (a) Detector insolation plot; (b) Detector contour plot........ 115
Figure 4.34 NCSETF March 22, 12:00 p.m. (a) Detector insolation plot; (b) Detector contour plot........ 115
Figure 4.35 NCSETF March 22, 4:00 p.m. (a) Detector insolation plot; (b) Detector contour plot........ 116
Figure 4.36 Simulated power output: N-S cornfield configuration with diverging rays 118
Figure 4.37 Simulated optical efficiency: N-S cornfield configuration with diverging rays 119
Figure 4.38 Simulated minimum concentration: N-S cornfield with diverging rays 122
Figure 4.39 Simulated maximum concentration: N-S cornfield with diverging rays..... 122
Figure 4.40 Simulated detector center concentration: N-S cornfield with diverging rays 123

CHAPTER 1

INTRODUCTION

1.1 Motivation

Modern society relies on energy as a fundamental component to everyday functionality. Since the industrial revolution, energy has been essential in the development of economic and social fortune throughout the world. Coupled with the tendency towards growth in world population and general standards of living, it is conceivable that the demand for energy will only increase. The International Energy Agency (IEA) predicts that by the year 2030 there will be a 50% increase in the world's energy consumption in comparison to current trends [1].

The development of energy technologies has allowed world civilizations to flourish to an unprecedented extent. The consumption of world fossil fuels, however, has come at a price. Greenhouse gas levels in the atmosphere have risen, and noticeable climate changes have been documented. In the past one hundred years global temperatures have been driven up by over 0.7°C and sea levels have risen more than 20 cm [1]. There is little doubt that emissions due to non-clean energy sources have contributed to such effects. Furthermore, finite fossil fuels are being consumed at a much quicker pace than they are produced. The current challenge, as well as the challenge that lies ahead, is renovating our energy sources and how we utilize them. One must consider renewable energy technologies in order to meet these challenges.

The sun, as a source of energy, is nearly inexhaustible and offers a pollutant free alternative to fossil fuels. The rate that energy from the sun is received on the earth's atmosphere is 5.4 x 10^{24} J/year. This equates to 170 trillion kW, an estimated 27,000 times the amount of energy produced by all of the man-made systems across the world [2]. Although not all of this energy is utilizable on the earth's surface, the sun is a precious source of energy, particularly in locations such as southern Nevada. Large scale power generation from solar energy has been demonstrated in various forms of concentrated solar power (CSP) facilities. Improving the utilization and efficiency of such facilities will play a key role in the solar and renewable energy future.

1.2 Concentrated Solar Power

1.2.1 Technology Overview

CSP facilities utilize high temperature heat in order to generate electrical power. Concentrating solar collectors, in the form of various sun tracking mirror configurations, concentrate sunlight onto a receiver that collects the solar energy and converts it to heat. In the second part of the system, the heat drives a turbine or heat engine which powers a conventional generator producing electricity. CSP systems can be utilized to generate power in a conventional power cycle by either entirely replacing, or by supplementing the burning of fossil fuels. The utilization of thermal storage has long been an area of focus in CSP systems, with aspirations for CSP facilities to produce electricity during clouding periods or hours of the night.

The optics of most concentrated systems can only make use of direct beam radiation, rendering diffuse solar radiation produced by scattering in the atmosphere non-utilizable. Consequently, CSP technologies are particularly appealing in the southwest United States as well as other sunbelt regions across the globe where direct normal irradiance (DNI) values are high [3]. Figure 1.1 presents a map depicting the amount of direct normal solar radiation as a function of location in the southwest United States. The map also portrays the available transmission lines, which is crucial in the location of CSP plants because it demonstrates the ease of accessibility for tying power produced from solar concentrating facilities into the electrical grid of the United States.

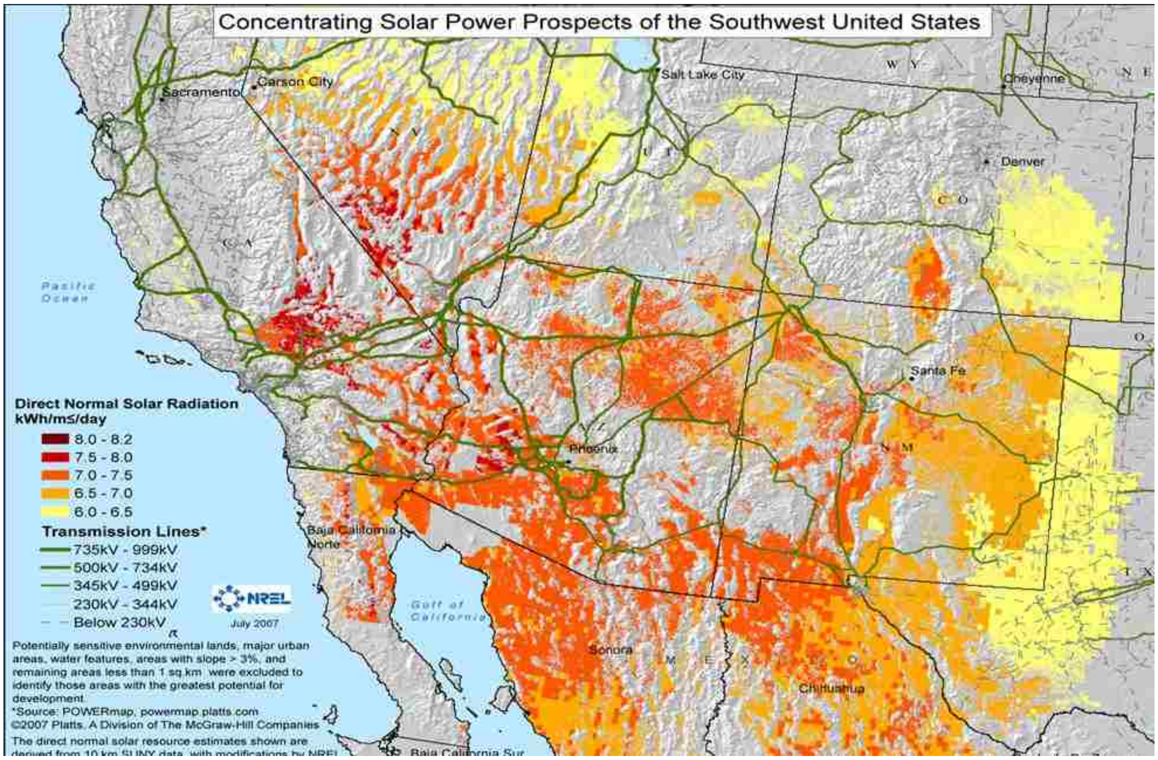

Figure 1.1 Concentrating solar power prospects for southwest United States [4]

The map portrays southern Nevada as an ideal location for CSP technologies, due to the high levels of DNI over the course of the year. In order to achieve high levels of concentration, CSP systems require tracking of the sun throughout the course of the day. The concentration is attained by redirecting the sunlight onto a heat exchanger, in the form of a receiver/absorber, where the heat is utilized to increase the temperature of a heat transfer fluid (HTF). Depending on the design of the system, the HTF can either be used directly in the power cycle, such as directly boiling water to produce steam, or by circulating the HTF through an intermediate cycle, such as in thermal oil or molten salt systems [1]. Utilizing an intermediate secondary cycle requires an additional heat transfer interaction process in the production of electrical power.

The higher the temperature the more efficiently heat engine power cycles are capable of converting thermal to mechanical energy, which is justified according to the principles of thermodynamics. Conversely, at higher temperatures there are greater heat rejection losses at the receiver, resulting in collector efficiency deficits as temperatures increase at the absorber. The result is that for any given concentration factor an ideal operating temperature exists for which the highest efficiency of converting solar energy to mechanical work is achieved [1]. Figure 1.2 demonstrates the theoretical total efficiency of high temperature solar concentrating systems in the generation of mechanical work as a function of receiver temperatures for varying concentration ratios. It is essential to recognize that the figure depicts an ideal solar concentrator combined with a perfect, Carnot, power cycle efficiency. Since an ideal absorber does not exist and perfect Carnot cycle efficiency is unachievable, optimum operation temperatures will be slightly lower than those presented in the theoretical figure. The plot demonstrates that at higher concentration levels, higher total efficiencies are achievable.

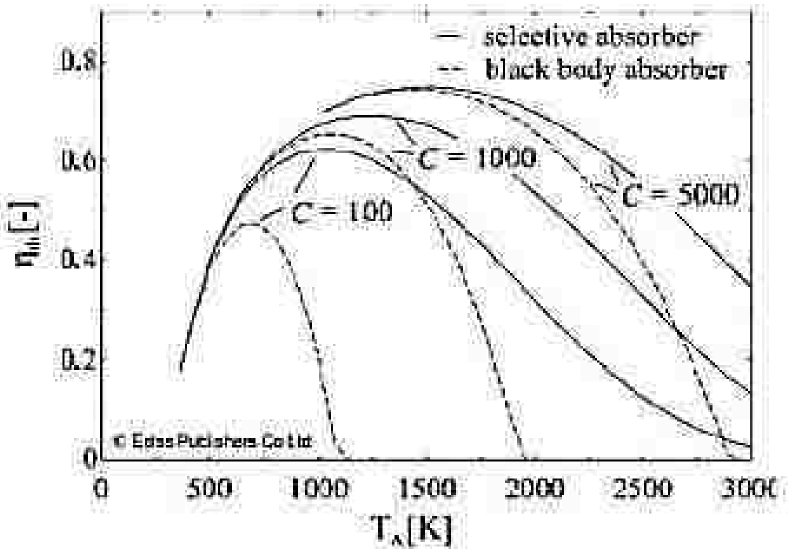

Figure 1.2 Theoretical efficiency of CSP systems for generating mechanical work [1]

The United States Department of Energy (DOE) has shown a renowned vigor in ongoing CSP research, development, and deployment efforts. The goal of the DOE is to increase the use of CSP technologies in the United States, in an effort to make CSP competitive in the intermediate power market by 2015. Additionally, the DOE is dedicating efforts to developing advanced technologies that will reduce systems and storage costs, enabling CSP to be competitive in the baseload power market by the year 2020 [5]. The DOE views CSP as a significant player in the renewable energy future, and has declared CSP one of the four subprograms within the Solar Energy Technologies Program (SETP). SETP is targeted towards developing the advancement of solar energy technologies to make solar electricity a more cost effective solution as compared to conventional forms of electricity generation [6].

CSP systems can be distinguished and categorized according to their technologies or optical arrangement of concentrating reflectors. Line focusing systems require only single-axis tracking of the sun in order to focus concentrated sunlight onto an absorber tube. Point focusing systems, on the other hand, require dual-axis tracking in order to focus the sun's radiation onto a thermal receiver. Currently, CSP technologies can be categorized into three primary types of systems: linear concentrators, dish/engine systems, and power towers. Table 1.1 compares performance data for varying forms of CSP systems. Most significantly for the scope of the research presented, is the capacity and concentration ratio of each type of technology. Additional insight as to how each form of CSP system is designed and operates is presented below.

Table 1.1 Performance data of various CSP technologies [1]

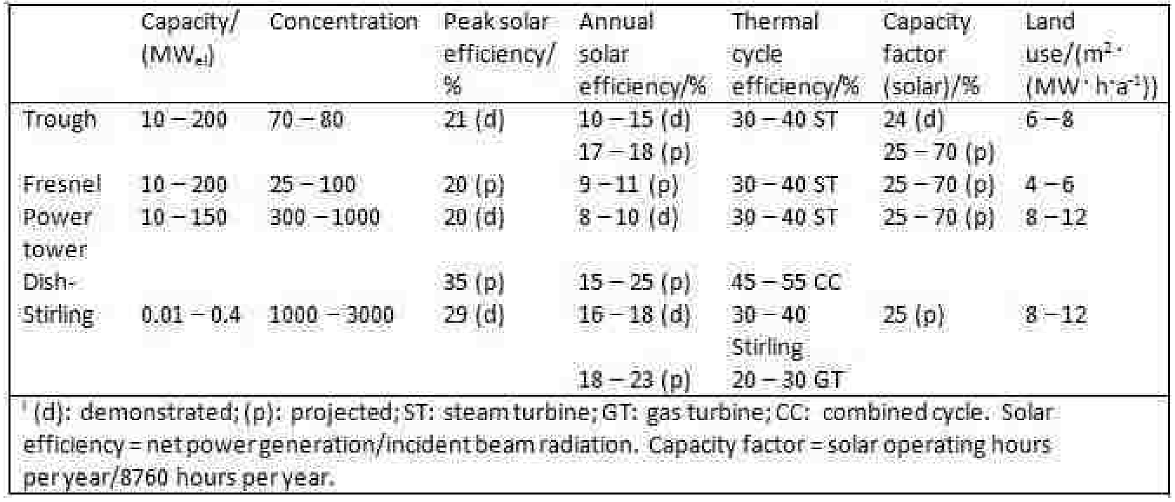

	Capacity/ (MW_{el})	Concentration	Peak solar efficiency/ %	Annual solar efficiency/%	Thermal cycle efficiency/%	Capacity factor (solar)/%	Land use/$(m^2\cdot(MW\cdot h\cdot a^{-1}))$
Trough	10 – 200	70 – 80	21 (d)	10 – 15 (d) 17 – 18 (p)	30 – 40 ST	24 (d) 25 – 70 (p)	6 – 8
Fresnel	10 – 200	25 – 100	20 (p)	9 – 11 (p)	30 – 40 ST	25 – 70 (p)	4 – 6
Power tower	10 – 150	300 – 1000	20 (d)	8 – 10 (d)	30 – 40 ST	25 – 70 (p)	8 – 12
Dish-Stirling	0.01 – 0.4	1000 – 3000	35 (p) 29 (d)	15 – 25 (p) 16 – 18 (d) 18 – 23 (p)	45 – 55 CC 30 – 40 Stirling 20 – 30 GT	25 (p)	8 – 12

[1] (d): demonstrated; (p): projected; ST: steam turbine; GT: gas turbine; CC: combined cycle. Solar efficiency = net power generation/incident beam radiation. Capacity factor = solar operating hours per year/8760 hours per year.

1.2.2 Linear Concentrator Systems

Linear concentrating systems consist of both parabolic trough as well as linear Fresnel reflector systems. Trough systems utilize parabolic shaped mirrors that focus the sun's radiation to a tube carrying a fluid down the focal point of the trough's parabola. The tube runs the length of the reflective trough and a HTF, usually oil, is used to generate electricity in a conventional steam generator. Parallel rows of troughs, typically aligned on a north-south axis, comprise a collector field. Aligned on a north-south axis, the troughs are then able to track the motion of the sun on an east-west axis throughout the course of the day. Parabolic trough designs can also incorporate thermal storage by setting aside a portion of the HTF during its hot phase. This allows for the energy of the fluid to be harnessed in electricity production during interruptions of solar irradiance. Figure 1.3 depicts the operating structure of a single-axis sun tracking parabolic trough system, while Figure 1.4 presents a schematic of a parabolic trough power plant that incorporates thermal energy storage.

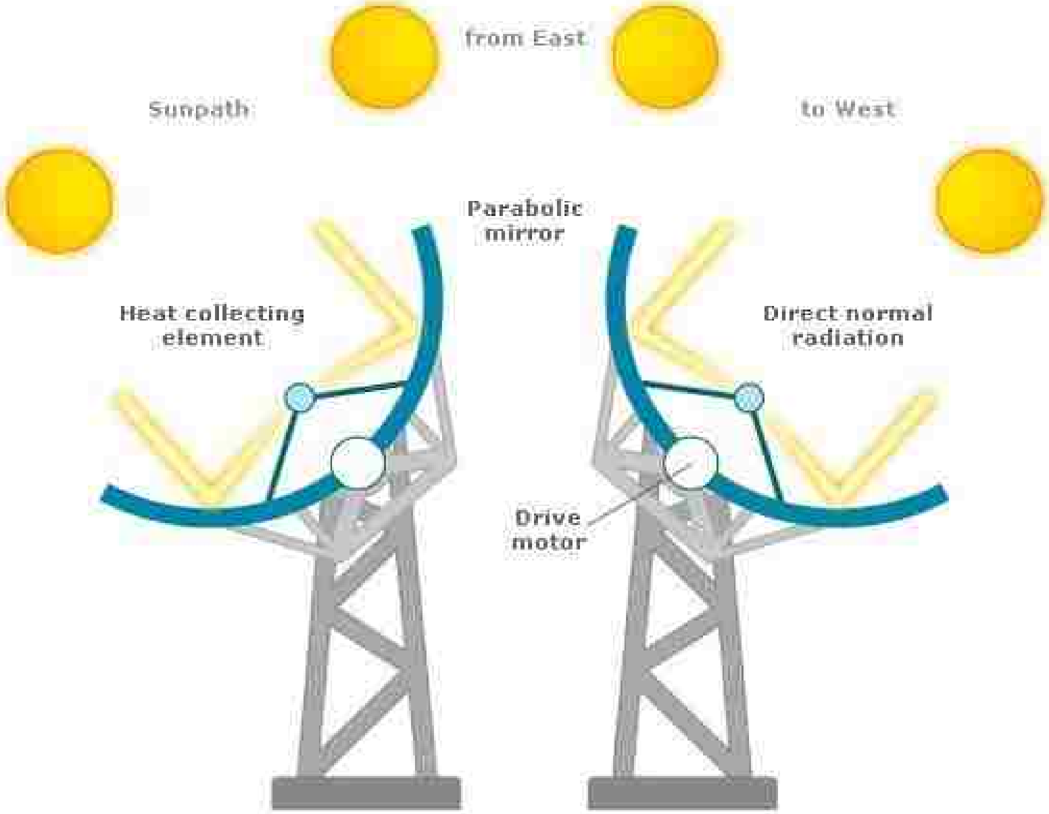

Figure 1.3 Parabolic trough single-axis tracking operation schematic [7]

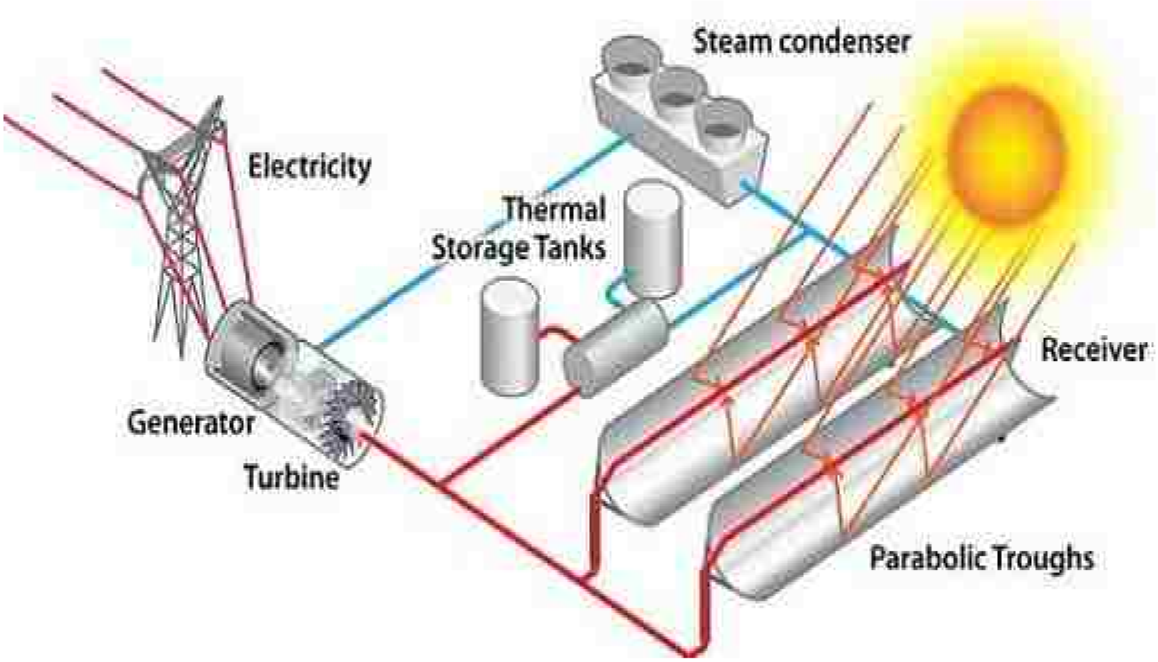

Figure 1.4 Parabolic trough power plant schematic incorporating thermal storage [8]

With parabolic trough systems the heat collection element (HCE) located at the focal point of the parabola moves with the concentrating collectors as the sun is tracked on a single- axis throughout the course of the day. Linear Fresnel systems are similar to parabolic trough systems, except they utilize flat or slightly curved mirrors mounted on ground level trackers to reflect sunlight onto a fixed receiver located above the mirrors. Unlike parabolic troughs, linear Fresnel systems utilize a stationary absorber which eliminates the need for flexible fluid joints required by trough systems [1]. Additionally, low-cost flat glass can be used and curved elastically due to the larger radius of curvature of the glass facets. Furthermore, linear Fresnel systems allow for varying aiming strategies in which the mirrors can be aimed at different absorbers throughout the course of the day. On the down side, the flat mirror arrangements of the reflectors lead to intrinsic optical aberrations, cosine losses, which can reduce the output by 20-30% in comparison to parabolic trough systems [1]. Linear Fresnel systems become economically feasible at the point in which reduced optical performance is offset by the lower investment costs required for the production of such systems. Figure 1.5 depicts a linear Fresnel reflector power plant schematic.

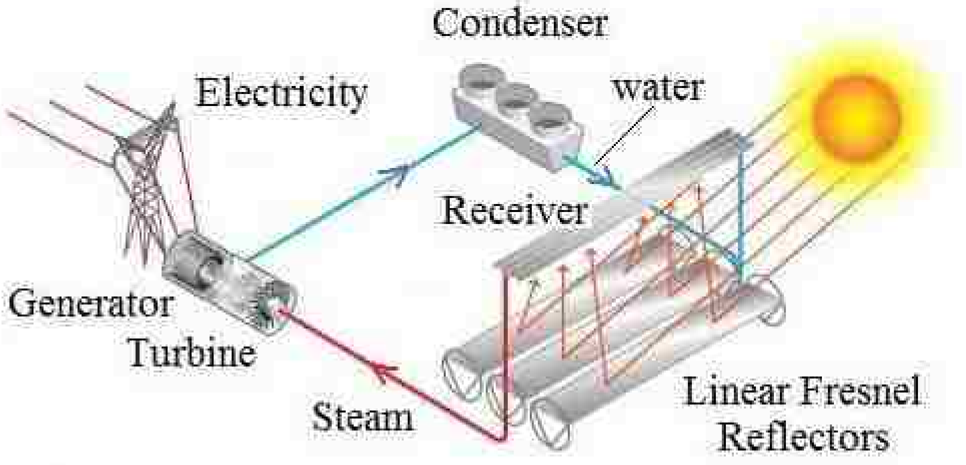

Figure 1.5 Linear Fresnel reflector power plant schematic [9]

1.2.3 Dish/Engine Systems

Solar dish/engine systems consist of two primary components, the solar concentrator and the power conversion unit. The concentrator is a parabolic dish of mirrors that concentrate the radiation from the sun onto a thermal receiver located at the dish's focal point. The power conversion unit consists of the thermal receiver and the engine/generator. The thermal receiver absorbs the concentrated solar energy, converts it to heat, and then transfers the heat to the engine/generator. The engine/generator subsystem is responsible for converting the heat into electricity. Dish/engine systems are limited in size to about 100-400 m^2, a practical limitation attributed to the constraints of high wind loads. As a result of their size limitation, dish systems generally produce anywhere from 9 to 25 kW_e. Dish systems have relatively high efficiencies among CSP technologies, which can be accredited to their high concentration ratios typically ranging from 1,000-3,000 suns [1]. Such a trend is expected and predicted in Figure 1.2.

Various forms of thermal receivers exist for dish systems. One form is a bank of tubes utilizing a cooling fluid, generally hydrogen or helium, which operates as a working fluid for the engine as well as a heat transfer medium. Another form is a heat pipe, in which the boiling and condensing of an intermediate fluid is utilized to transfer heat to the engine. The most common type of engine utilized to convert the heat to power is the Stirling cycle engine. A heated fluid is utilized to propel pistons and create mechanical work. The mechanical work, or rotation of the engine crankshaft, in return drives a generator producing electrical power [10]. Figure 1.6 depicts a Dish/Engine power system.

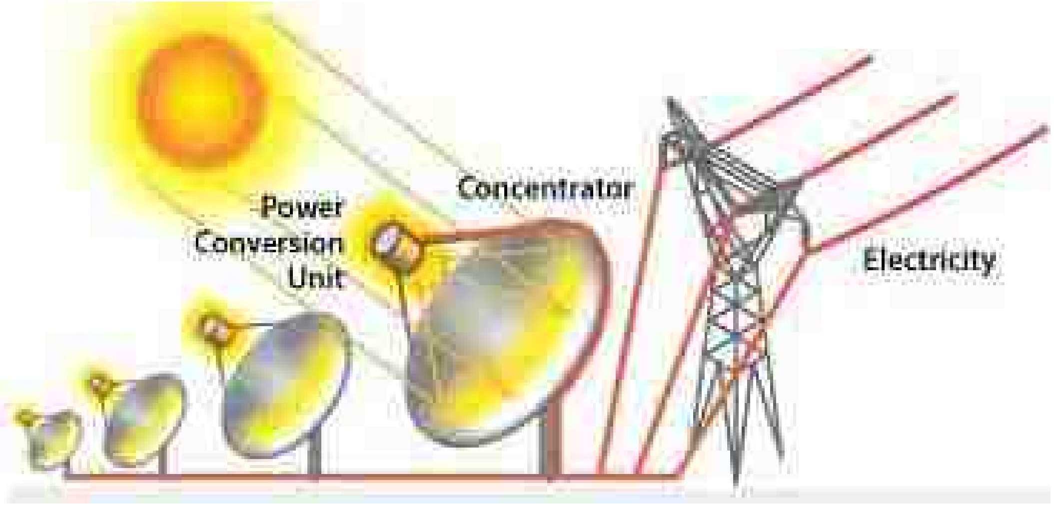

Figure 1.6 Dish/engine power system [10]

1.2.4 Solar Power Towers

The final form of CSP technology commonly utilized, and the form most pertinent to the scope of research presented in this thesis, is solar power towers or central receiver systems. Central receiver systems utilize large dual-axis sun tracking mirrors known as heliostats to focus the sun's radiation onto a central receiver at the apex of a tower. The concentrated sunlight heats a HTF flowing through the receiver which is used to generate steam. The steam is then utilized in a conventional turbine-generator to produce electricity.

The concept of central receiver systems was first introduced by scientists from the USSR in the 1950s. In 1965, near Genova, Italy Professor Giovanni Francia produced the first full scale size experiment in which 120 'tea-table' size round mirrors were focused on a steam generator located at the top of a steel frame. As a resulting product, Francia was able to generate superheated steam at 500°C, 10 MPa [11]. Presented in Figure 1.7 is a plant schematic representation of a solar power tower central receiver system.

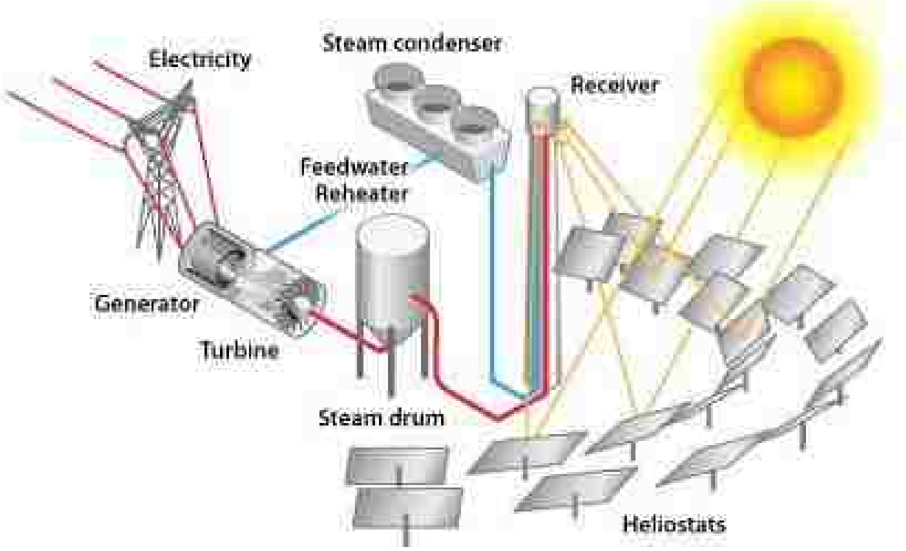

Figure 1.7 Central receiver power tower system [12]

Different HTFs are incorporated into various solar power tower plant designs. Common HTFs include water/steam, as well as molten salt. Due to its heat transfer and thermal storage capabilities molten salt is often considered a good thermal energy storage medium, providing the additional benefit of being able to produce power at times of no sunlight, such as cloudy weather or night.

Two primary types of receivers are utilized in solar power tower systems, external receivers and cavity receivers. External receivers generally consist of vertical tubes welded side by side to produce a cylindrical shape tube bundle heat exchanger. The cylindrical shape of the receiver allows for a 360° acceptance angle, enabling heliostats to be placed completely around the tower. At the top and bottom of the tubes are headers that supply and collect the HTF. The total area of external receivers is typically kept at a minimum in order to reduce the effect of heat losses. The minimum size limit of an external receiver is specified by the maximum temperature of the tubes, and consequently the heat removal capability of the HTF. Common height to width ratios for external tube receivers are in the range of 1:1 to 2:1 [13]. Figure 1.8 demonstrates the external receiver originally utilized at the Solar One central receiver facility located in Barstow, CA.

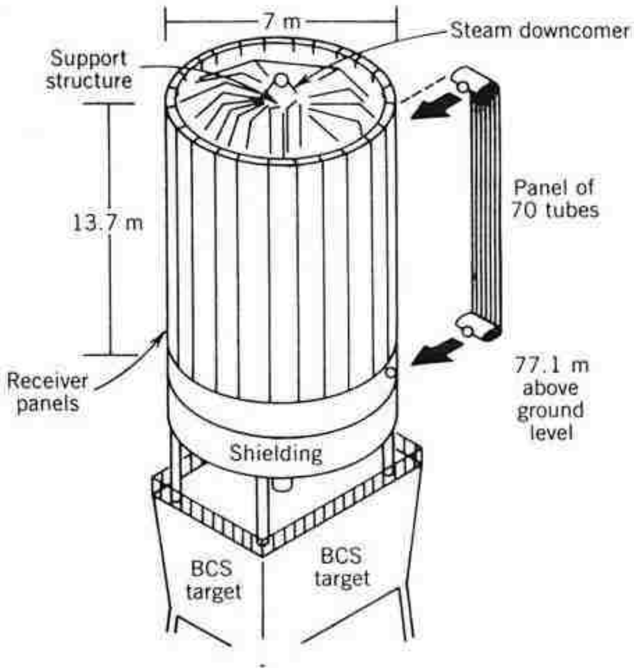

Figure 1.8 External receiver utilized at Solar One facility in Barstow, CA [13]

Cavity receivers are utilized in place of external receivers in an effort to reduce the total heat losses from the receiver. In such a system, the solar flux absorbing surface is located within an insulated cavity, effectively reducing the convective heat losses from the absorber material. An absorbing material forms the walls of the cavity so that solar flux reflected from the heliostat field is reflected through an aperture and onto an absorbing surface. Consequently, cavity receivers are limited to the acceptance angle of the aperture, typically in the range of 60° to 120° [13]. Since the acceptance angle is limited, the location of the heliostat field becomes limited as well. Often times multiple cavities are located on one receiver to broaden the acceptance angle, and subsequently the location in which heliostats can effectively be placed. It is common for cavity receivers to have an aperture area on the order of one-third to one-half the internal absorbing surface area [13]. Figure 1.9 illustrates a cavity receiver with four apertures to increase the acceptance angle of concentrated rays.

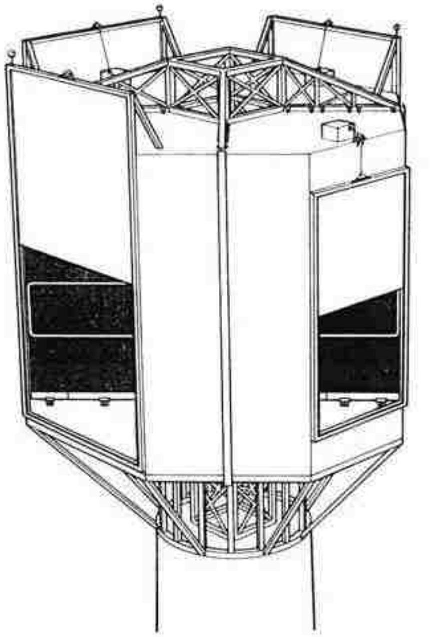

Figure 1.9 Cavity central receiver with four apertures [13]

Due to the high temperatures that central receiver systems are able to obtain, solar power towers accomplish more efficient thermodynamic steam cycles in comparison to trough technologies [1]. In central receiver systems the energy conversion takes place at a single fixed focal point located at the top of a tower, which requires dual-axis tracking. This is a distinguishing difference from linear concentrating systems that focus to a line instead of a point, thus requiring only single-axis tracking. Central receiver systems consolidate the energy transport network, allowing the design emphasis to be placed on improving the energy conversion process, thus creating a more cost effective solution [11]. Such factors make solar power towers an ideal candidate for mid-term cost reduction of electricity among CSP technologies.

Amongst CSP technologies, central receiver systems are often predicted to be the most economically feasible solution for producing solar-generated electricity or hydrogen on a grand scale. Furthermore, approximately half of the cost of central receiver systems is in the collector arrangement, implying the heliostat field [14]. Such a condition indicates two things. First, it is justifiable to utilize an efficient engine that can convert the largest possible amount of energy received by the collector array to utilizable electricity. Second, by reducing the cost and improving the performance of heliostats the economic viability of solar towers becomes consistently more realizable.

1.3 Tower Reflector Systems

1.3.1 Concept Overview

The concept of a solar down beam tower was first proposed by Rabl [15] in 1976. A tower reflector (TR) system utilizes a reflective mirror at the top of a tower, replacing the receiver of traditional tower power systems, to redirect the radiation from the sun onto a focal point at ground level. The motivation for the TR configuration originated from the problems associated with the heat transfer process from the thermal receiver at the top of a tower to the power block at ground level. Traditional solar towers require the pumping of a HTF to the top of a tower. With towers reaching hundreds of meters in height depending on configurations, pumping a HTF to the top of a tower is not a mundane task. Rabl [15] proposed it was desirable to transport energy in the form of solar radiation all the way to the power block at ground level. Rabl [15] also suggested the concept of a secondary receiver concentrator (RC) located at ground level, in the form of a compound parabolic concentrator (CPC), to further focus and concentrate the down beam rays. If the optical losses can be limited the concept of a TR system becomes feasible.

Yogev [16] illustrates the benefits of a ground level plant configuration. Primarily, all major hardware (Receiver, CPC, Power Block, etc.) is located at or near ground level. A down beam optical configuration eliminates the need for long and extensive piping, as well as a gigantic and expensive tower. Furthermore, the requirement and frequency for facility personnel to access the top of the tower is drastically reduced. Yogev [16] presents the results of a technical feasibility study for a TR system. It was found that supporting a reflector at the top of a tower is technically viable from a practicality perspective. Additionally, the results demonstrated that the cost of a tower to support down beam optics is significantly less than the cost required to construct a conventional solar tower. The conclusion appears reasonable, since the tower is supporting only a reflector component allowing it to be lightweight and relatively cheap.

1.3.2 Optics of Down Beam Towers

Various optical configurations for down beam systems have been investigated. Segal [17] performed an in-depth optical comparison of hyperboloid and ellipsoid shaped down beam mirrors. From an optical perspective, a hyperbolic down beam mirror allows for the aim point (AP) of the heliostat field to be located above the TR. Conversely, an elliptical down beam mirror requires an AP below the height of the TR. Presented in Figure 1.10 is an optical comparison of a hyperbolic and elliptic down beam mirror.

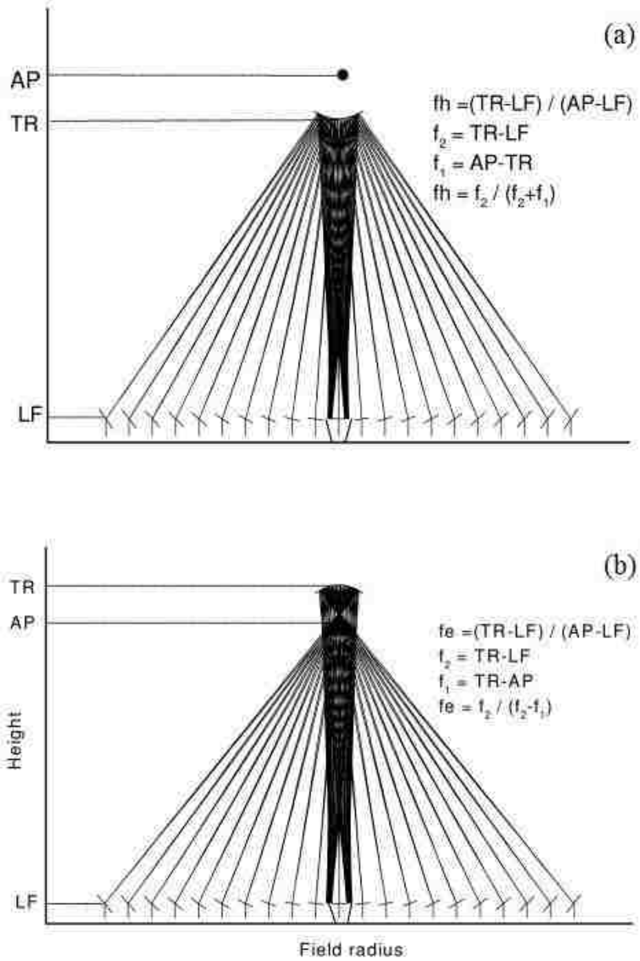

Figure 1.10 Solar tower reflector optical overview: (a) hyperbolic mirror; (b) elliptical mirror [17]

In Figure 1.10, LF portrays the lower focus height, or height of the secondary RC. F_1 is the distance from the TR to the AP, while f_2 is the distance from the TR to the secondary concentrator. Consequently, fh can be described as the fractional position of the vertex of the hyperboloid from the height of the AP, and fe as the fractional position of the ellipsoidal upper vertex to the AP [17]. It was demonstrated that the maximum concentration at the entrance to the secondary receiver for a hyperbolic mirror is in the range of fh = 0.7 to fh = 0.75. Similarly, maximum concentration on an equal scale for an elliptical down beam mirror was demonstrated at fe = 1.5 to 1.75. The conclusion that can be drawn is that for an equivalent concentration, the location of an elliptical mirror is much higher than the required location of a hyperbolic mirror [17].

It was determined that moving up the elliptical mirror away from, or down the hyperbolic mirror towards, the focal point resulted in a smaller image size. Such a transition also results in two adverse side effects. First, the required size of the down beam mirror is increased. Second, if a secondary concentrator is utilized, the acceptance angle into the RC is increased. Figure 1.11 demonstrates the effects of such phenomena. Since the ability for a RC to further concentrate solar radiation is directly proportional to the acceptance angle for which the rays enter the RC, the rate of convergence from the down mirror to the RC is a significant design parameter [17].

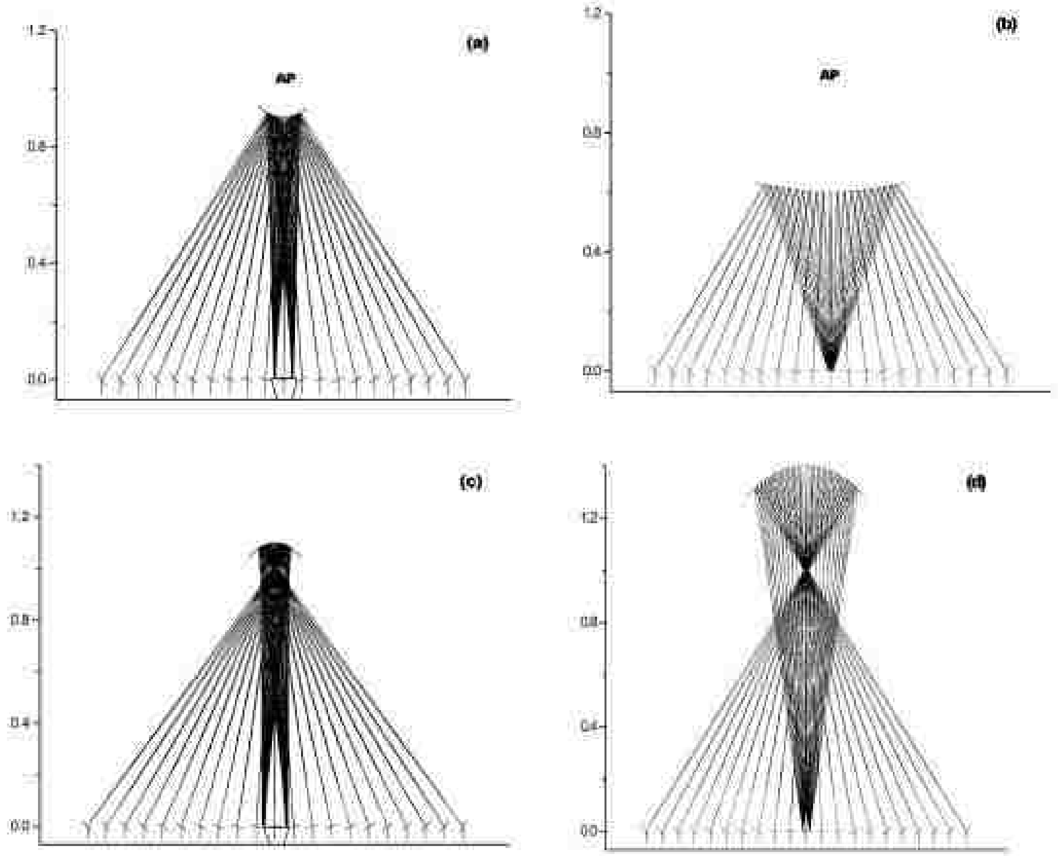

Figure 1.11 Effects of translating TR height for hyperbolic (a)-(b) and elliptical (c)-(d) down beam mirror [17]

For down beam systems located in the Northern Hemisphere, including southern Nevada, heliostat fields are commonly designed asymmetrically around the tower with the majority of the heliostats being located on the north side of the tower [17]. Such a heliostat field configuration requires the down beam mirror axis to be tilted so that rays still reach the RC from a vertical direction. In the case of a hyperbolic mirror, the tilt is accomplished by moving the lower focus north relative to the targeted AP. Conversely, for an elliptical down beam mirror the lower focus is moved south relative to the targeted AP [17]. Figure 1.12 demonstrates the required mirror adjustments for a hyperbolic and elliptical down beam mirror favoring a northern asymmetric heliostat field.

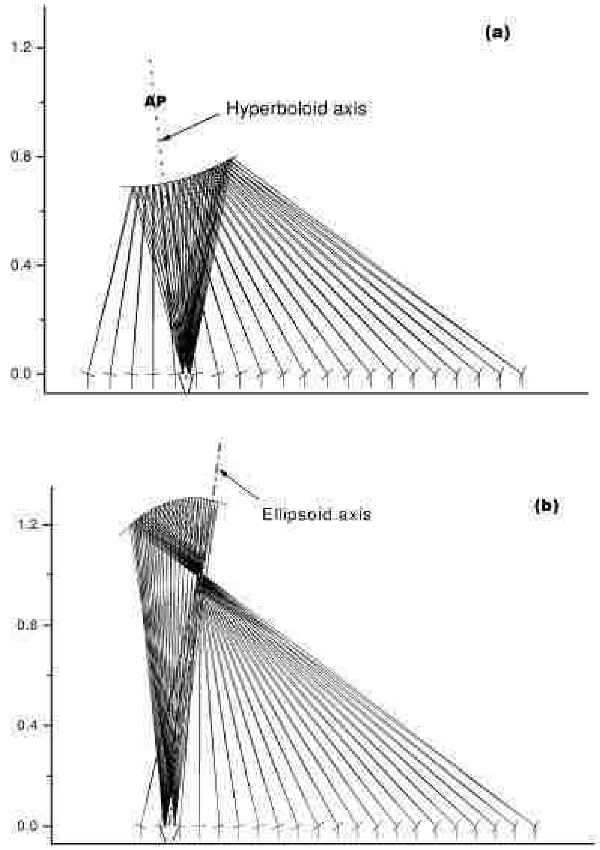

Figure 1.12 (a) Shifting of hyperbolic mirror to favor northern heliostat field; (b) shifting of elliptical mirror to favor northern heliostat field [17]

The conclusions that can be drawn from the work of Segal [17] are influential in the design and development of down beam optical systems. Most significantly, a hyperbolical surface is more promising for a solar down beam mirror in comparison to an ellipsoidal mirror. An ellipsoidal mirror is non-favorable because the AP of the heliostat field is always below the down beam mirror, requiring a higher tower. A hyperbolic mirror not only has the advantage of allowing for a shorter tower, but also requires less reflector surface area for the same level of concentration [17].

1.3.3 Weizmann Institute

The realization of down beam optics has been demonstrated at the Weizmann Institute of Science in Rehovot, Israel. In 1995 the Solar Research Facility added down beam optics to its previously existing solar tower developed in 1988 for concentrating solar energy research. The tower measures 54 m tall and is surrounded by 64 multi-faceted heliostats with dimensions of 7 x 8 m. The tower contains 5 separate experimental levels, which allows for different experiments to be implemented by focusing the heliostats on various levels. The down beam mirror of the tower was installed at the 45 m height of the tower. The facility has recently been in the process of improving the optical performance of the heliostat field by replacing the mirrors, an approximated one million dollar renovation [18]. Figure 1.13 displays the configuration of the solar tower facility at the Weizmann Institute of Science, while Figure 1.14 is a depiction of the upper portion of the tower containing the various levels for testing along with the down beam reflector.

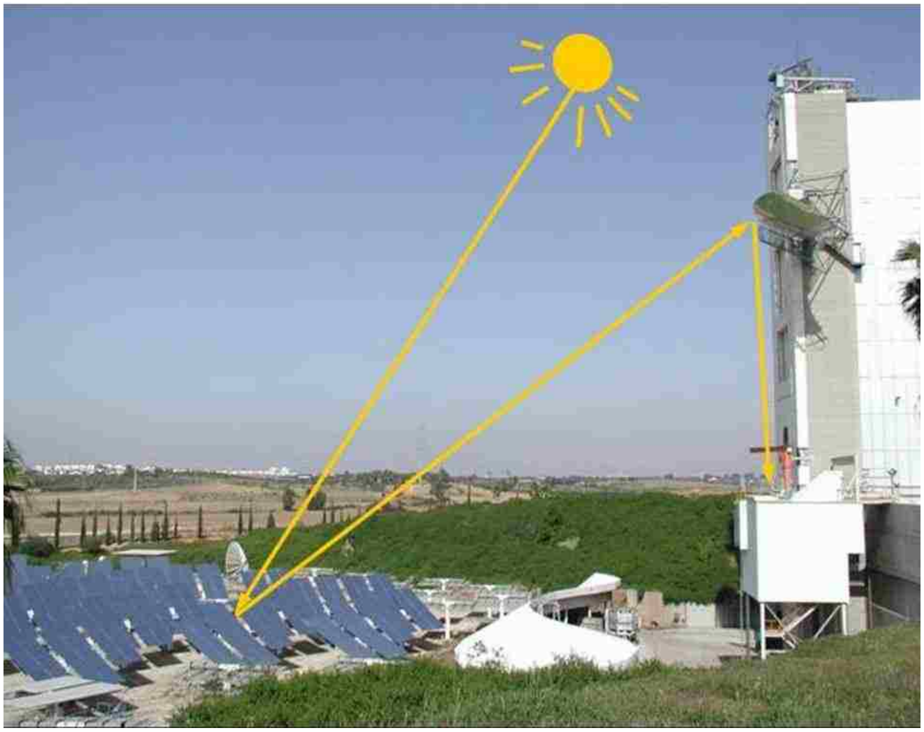

Figure 1.13 Solar down beam facility at Weizmann Institute of Science [19]

Figure 1.14 Top of tower at Weizmann Institute of Science [19]

The down beam mirror at the Weizmann Institute of Science measures 72 m^2 and is in the form of a hyperbolic design. The reflector is a large monolithic mirror constructed of 858 separate facets. The TR is comprised of 22 rows each containing 39 facets. The facets are consistent in height at 0.3 m, but range in width from 0.17 m to 0.4 m. The facets were first installed at ground level; the entire mirror was then lifted and placed on the tower [19]. Figure 1.15 identifies the dimensions of the down beam mirror utilized at the Weizmann Institute of Science.

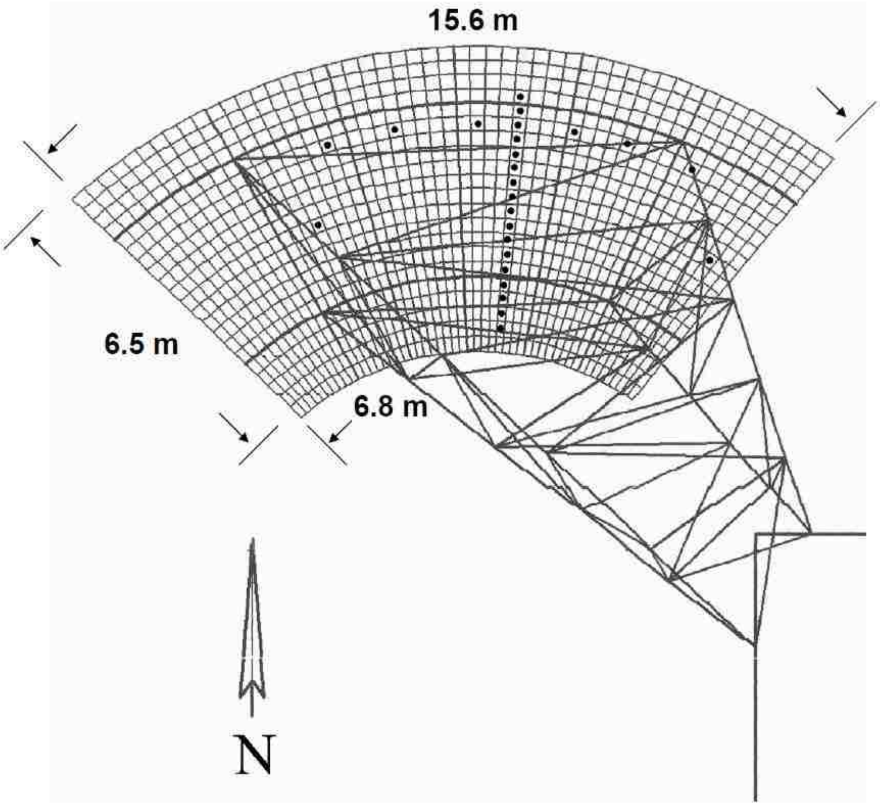

Figure 1.15 Description of hyperbolic multi-faceted down beam mirror at Weizmann Institute of Science [19]

The Weizmann Institute of Science has developed the down beam system to explore the concepts of power production, alternative fuels, solar driven thermal and chemical processes, and long term storage and transportation options [20]. The production of electricity is certainly a key area of focus for the institute, but they have found many other areas of interest in which the facility has shown useful as well. For example, the production of hydrogen has been an extensive topic of interest at the Weizmann Institute of Science solar facility. Hydrocarbon reforming, methane decomposition, and thermal-electrochemical dissociation of water at high temperatures have all been investigated using solar energy. Processes have been analyzed for developing means to use solar energy to convert biomass to fuel in a procedure called biomass gasification. The facility has been used as a resource for developing high temperature stable catalysts for steam reforming of methane and for the solar reduction of metal oxides. The production of zinc from zinc oxide in an effort to fuel a fuel cell and produce hydrogen is a specific area of interest at the Weizmann Institute of Science solar facility [18].

1.3.4 Masdar Tower

The Masdar Institute of Science and Technology, along with Cosmo Oil Company from Japan and the Tokyo Institute of Technology have recently developed a solar down beam facility in Masdar, Abu Dhabi. The current facility in Masdar is a 100 kW_e demo site and is operated by students at the Masdar Institute of Science and Technology. The relatively small scale facility utilizes a 20 m high tower, with a multi-ring TR comprised of 48 mirrors capable of achieving 98% reflectivity [21]. The Masdar facility is predominantly centered towards research in the production of electricity, with little emphasis on solar chemistry expressed. Figure 1.16 is a picture of the demo down beam facility established in Masdar, Abu Dhabi.

Figure 1.16 Down beam demo facility in Masdar, Abu Dhabi [22]

The Masdar demo facility is a small scale implementation similar in scope to the design presented by Tamaura [23]. Tamaura proposed a multi-ring TR of space truss design supported in three sections by cubic truss columns forming an equilateral triangle. Significant mechanical advantages in comparison to the more traditional hyperbolic shaped reflector are presented. In terms of mechanical integrity, the multi-ring central reflector offers a feasible solution to wind force issues, and has a wider range of focus [23]. Furthermore, when compared to the hyperbolic shape reflector, the total cost of the multi-ring system, including reflector, supporting truss columns, and foundation is approximately half [23].

Tamaura describes a feasibility study for a beam down system pilot plant to be constructed in Almeria, Spain. The goal was to assess the viability of a commercial plant utilizing beam down optics. Preliminary results demonstrated that a beam down system commercial plant would fall short of Solar Tres in terms of profitability. There were, however, indicators of design improvements that could significantly improve overall plant efficiency as well as profitability. Increasing heliostat efficiencies and reducing heliostat costs were among the most promising methods of plant improvements. Furthermore, significant potential was expressed for the advantages presented by utilizing a multi-tower system in which a mixing of heliostat fields allows heliostats to shift focal towers in an effort to improve optical efficiency [23].

1.4 Thesis Incentive and Scope

As CSP technologies progress and solar chemistry experiments are further established, there will inevitably be a need for diversified testing facilities in which such technologies and research objectives can be evaluated. In the present state, there are limited resources available for testing advanced CSP technologies, particularly solar tower technologies. This thesis investigates using down beam optics as a solution for bridging the gap between the laboratory bench scale and the engineering test scale in the development of such technologies. Down beam optics are ideal for such a facility because testing can be conducted at ground level, instead of at the top of a 100 m tower. A solar beam down test facility offers a tool for improving the process of developing CSP technologies. In order for CSP to become a revolutionary player in the renewable energy future, research and development of CSP technologies will require a rapid turnaround of ideas and solutions. The facility proposed looks to alleviate some of the problems traditional tower facilities demonstrate in terms of testing, in an effort to produce a more seamless process for the development of CSP technologies.

Southern Nevada shows promise as a location for constructing a solar down beam test facility, due to the high levels of DNI throughout the course of the year as displayed in Figure 1.1. Coupled with relatively cheap land prices, and the establishment of several large scale solar projects within close vicinity, southern Nevada shows great potential for the realization of a down beam solar test facility. Construction of a solar test facility in southern Nevada would provide a multitude of benefits to Nevada as well as the nation. It would support collaborative studies amongst experimenters, the facility, the University of Nevada Las Vegas (UNLV), and local entities. It would allow local contractors and students to gain further expertise in the development and operation of solar facilities. Furthermore, the facility could demonstrate additional visibility for Nevada as a solar energy hot zone. Contractors, collaborators, and all involved parties would exhibit ongoing learning efforts and expertise in various solar energy endeavors.

The scope of the work presented is twofold. A preliminary feasibility design is presented for a solar down beam test facility to be implemented in southern Nevada. A model is then developed to demonstrate the optical performance of the facility. Utilizing ray tracing techniques, an estimated output can be made, i.e. power and concentration, for a down beam facility located in southern Nevada. The development of, results of, and conclusions drawn from the comprehensive model capable of simulating the facility on an hourly basis is the heart of the research performed.

In Chapter 2 the methodology behind the conceptual design of the proposed facility is presented. This includes the minimalistic utilization of permanent onsite infrastructure and a planar Newtonian optic system in an effort to keep the facility simplistic in design. Chapter 3 pertains to the development of the model utilized to simulate the optical performance of the facility. More specifically, Chapter 3 provides the algorithms established to calculate the orientation and layout of the heliostat field along with the construction of the ray tracing simulation. Chapter 4 presents the results of the simulated models. Outputs are portrayed in the form of time dependent power and concentration curves. Furthermore, irradiance plots and statistical simulation data is obtained. In Chapter 5 final conclusions are presented along with proposed future improvements of the designed model.

CHAPTER 2

FACILITY DESCRIPTION AND DESIGN

2.1 Conceptual Design

The solar test facility, referred to as the Nevada Concentrated Solar Energy Test Facility (NCSETF), is conceptually envisioned to be simplistic in design. Optically, a Newtonian system utilizes a flat planar down beam mirror, simplifying the geometry of the down beam reflector. As a means to minimizing investment costs, it is intended that the majority of the infrastructure is to be rented. Therefore, power, water, cooling, and sanitation are all to be leased. Furthermore, since the heliostat field comprises a large portion of the initial investment cost in such a facility, it may also be leased depending on the contractor.

Many experimental user facilities are low cost to utilize, but require significant upkeep to maintain operating conditions. The NCSETF is intended to be developed with minimum experimental infrastructure, with users capable of bringing in stand-alone experiments they can test under the output conditions of the facility. The concept originated from UNLV research staff Dr. Johnson's discussions with research scientists from General Atomics Corp., for the possibility of evaluating thermochemical energy technologies using concentrated solar radiation.

There are several benefits to an approach of leasing and minimizing infrastructure. Investment costs and turnaround times required to get the facility up and operational are minimal in comparison to a permanent facility. Permitting for a long-lasting facility is likely a much more strenuous process. Furthermore, such a design strategy allows for flexibility in terms of long term management of the facility. If the facility is being effectively utilized then the temporary assets could be converted to permanent ones. Conversely, if it is found that the facility is not required, or the relocation of the facility is desired, then orderly removal of the assets and recovery of the site is achievable. Another advantage to a temporary facility is that it can be decommissioned for long periods of time, such as off-seasons, and then started back up again with relative ease. Figure 2.1 is a general layout of what is envisioned for the facility.

Figure 2.1 NCSETF site layout utilizing temporary infrastructure

The NCSETF accommodates users as they arrive with pre-configured test experiments. Experimenters subject their tests to the conditions of the facility, by pulling up and mounting their previously constructed test environment as displayed in Figure 2.1. It is envisioned that experiments are brought in via institutionally developed test trailers.

Upon completion, users are then able to conveniently pack up their experiment, leaving space for a new experiment to be brought in. The goal of such a configuration is to provide ease of access and accommodation of different experimental programs. By allowing experimenters to come to the facility with their own experimental hardware, the bugs and testing configuration issues can be worked out before arriving on site. For users who can't support an extensive testing trailer, it is envisioned that a general user trailer will be permanently available on site for preliminary studies. Academic, governmental, and commercial agencies ranging from domestic to international customers can all benefit from the facility. Again, one of the most significant advantages to the facility's design is that commercial users will be able to develop proprietary applications with full control over intellectual property.

2.2 Targeted Output

It is targeted that the NCSETF will be able to provide 1 MW_{th} of solar thermal energy at 1,000 suns concentration at ground level for utilization in the development of advanced solar energy technologies. The optical geometry of the system is designed around achieving such an output during peak performance of the facility. Table 1.1 demonstrates that 1,000 suns concentration is enough to provide practical operating concentrations for common CSP technologies as discussed in Chapter 1. 1 MW_{th} of solar thermal energy is similar in power output to that provided by the down beam system implemented at the Weizmann Institute of Science. Furthermore, 1 MW_{th} of thermal energy allows for absorbers, receivers, and other advanced concentrated solar energy technologies, as well as thermochemical experiments, to be evaluated under relatively high power conditions. It is intended that the experiments can either take the light directly, which is a good model of tower-top optical behavior, or the light can be extracted for further processing.

If the facility were to prove successful, and utilized by experimenters on a consistent basis, a larger system may become feasible for solar thermal testing under conditions of higher power output and concentration. Since the optical geometry is intended to produce the targeted output during peak performance, testing conditions requiring lower power outputs or concentration levels can be achieved by implementing tests during morning or afternoon hours when DNI values are less. Another option for lower output testing would be to utilize only a portion of the heliostat field, reducing both testing power output and concentration conditions.

It is significant to distinguish how the profile of the output for a testing facility will vary in comparison to a facility designed for the production of electrical power. With the production of power, a consistent output is of the utmost concern. Thermal storage has long been the focus of extensive research for plants utilizing solar energy to produce electrical power. The goal of utilizing thermal storage is to allow for a constant output during cloudy periods and hours of night. A test facility, however, does not have the same stringent requirements. A facility optimized for research has a different output profile than that for producing power. In point of fact, a constant output for a testing facility limits the scope of testing conditions and capabilities. For a solar testing facility it is crucial that the output can be estimated for a given time frame. Experimenters need to have known and established testing conditions for which they are subjecting their experiments to before implementing onsite testing at the facility. A method for modeling the facility on an hourly basis is the focus for establishing the performance of the NCSETF.

2.3 Site Details

2.3.1 Reflector Design

The primary reflector makes the design of the NCSETF unique from other down beam optical systems. The concept is adopted from the optics of a Newtonian telescope. Instead of utilizing a hyperbolic mirror like that at the Weizmann Institute of Science, or Cassegrain optics like the multi-ring reflector in Masdar, the NCSETF is designed using a flat planar down beam mirror. A planar down beam mirror offers several benefits in terms of developing a testing facility.

A primary advantage to using a planar down beam mirror is its intrinsic capability to host multiple experiments. A hyperbolic or elliptical reflector is constructed for a single focal point. A flat planar mirror can allow for the focal point to be adjusted by simply varying the AP. It is intended that the AP for the heliostat field be one that yields concentrated solar radiation at ground level directly below the center of the down beam mirror. While this is the approach used to develop the model for the targeted output of the facility, a separate AP could yield an additional output of concentrated rays at ground level. Therefore, a separate heliostat field, or a portion of the original field could be used to accommodate multiple experiments simultaneously. A planar down beam mirror easily supports smaller scale testing for experiments not requiring the full capability of the facility by allowing for varying focal points of lesser power and concentration.

A planar down beam mirror is relatively simple to design and fabricate in comparison to a large hyperbolic mirror. Hyperbolic reflectors utilized in down beam systems require extensive designing of both the down beam reflector as well as the secondary RC. A planar mirror sets a standard of more predictable behavior. A planar mirror, based on its dimensions and orientation, will have an easily foreseeable convergence angle of rays towards ground level. A planar TR bends the optical image to ground level, which allows for a good model of on-tower optical behavior to be explored at ground level. More significantly, deformation of a planar mirror is much easier to address from an optical perspective.

Thermal expansion can render detrimental effects to a TR depending on the operating conditions for which the reflector is being subjected to. Deformation of a hyperbolic mirror due to thermal expansion results in distortion of the optical system. Enough deformation could render the facility useless or even hazardous. A planar mirror can be developed to expand uniformly without distorting the optics of the facility. Such an advantage is very significant in terms of reliability of the system. Furthermore, concerns of active cooling become less relevant for a planar mirror if optical deformation of the system can be avoided.

2.3.2 Tower Design

When designing a tower for supporting a down beam system, high optical access from the heliostat field to the beam down reflector is essential. For a south facing heliostat field, the north side of the tower must be highly visible so that rays reflecting from the heliostat field to the down beam mirror are not obstructed by the tower. Consequently, the north side of the tower must be minimalistic in terms of structure.

Conceptually, the tower was originally envisioned as a steel lattice truss assembly as presented below in Figure 2.2.

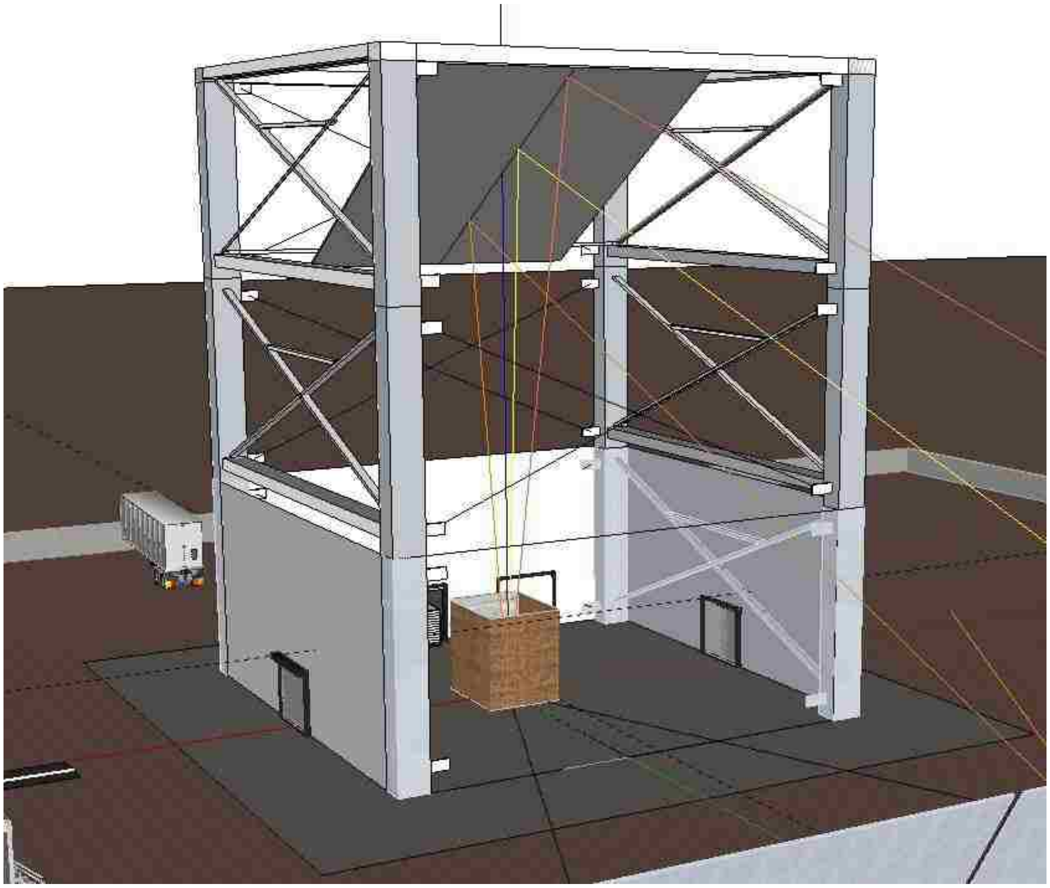

Figure 2.2 Steel lattice truss tower design for NCSETF

While investigating potential sites for the facility in southern Nevada it was found that building height restrictions in areas of Nye County are limited to approximately 100 ft (30.48 m). For this reason, the tower was designed to be roughly 60 ft^2 (5.57 m^2) by 100 ft (30.48 m) tall. The tower needs to be capable of supporting the approximated 10-20 ton weight of the down beam mirror. The tower will also need to be inherently stiff to avoid optical distortion. Furthermore, the tower must be constructed in a manner such that it is intrinsically fire proof. Under operating conditions it is intended that the tower be unoccupied to avoid risks to user safety.

Another considered design for the construction of the tower utilizes three steel beam columns instead of a lattice truss structure. Similar to the tower implemented in Masdar, a beam and column tower configuration offers possible optical benefits. With a three beam column tower, there is less to interfere with rays traveling from the heliostat field to the down beam reflector. For the primary heliostat field, located directly north of the tower, the optical benefits are likely minimal. If an additional heliostat field were to be introduced for smaller scale testing, as previously suggested, then the optical advantages of a three column tower may become much more realizable. A secondary experiment with a different AP may result in rays entering from the east or west side of the tower. A steel lattice tower would obstruct the line of site from the new heliostat field to the top of the tower. A three column tower, however, makes the additional heliostat field achievable from an optical perspective since it does not fully obstruct the visibility of the down beam mirror when viewing the tower from the side. Figure 2.3 demonstrates what is envisioned for the NCSETF implemented using a three column design.

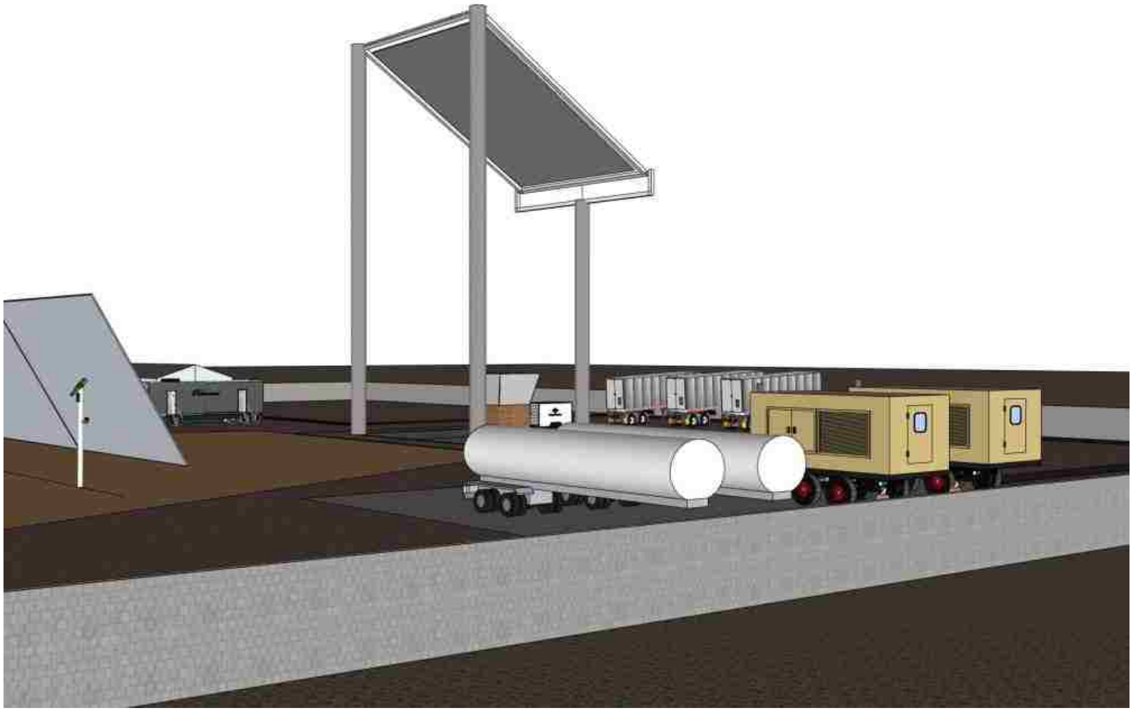

Figure 2.3 NCSETF schematic with 3 column tower

Ultimately, final tower construction will need to be extensively investigated from a barrage of perspectives. The focus of the research presented is on evaluating the optics of the NCSETF. More qualified personnel, such as an engineering firm with expertise in tower construction, will need to determine the most appropriate assembly of the tower for the given weight and line of sight requirements specified. Estimates for the tower are currently being solicited.

2.3.3 Heliostat Field

The solar field efficiency can be described as the reflected power arriving at ground level divided by the product of the incident solar power on the total area of the heliostat field [24]. Many contributing factors determine the optical efficiency of a heliostat field. The four primary contributors to optical efficiency losses include blocking, shading, cosine losses, and reflective losses. Blocking occurs when the rays reflected from a heliostat are obstructed by a neighboring heliostat. Shadowing, on the other hand, occurs when a heliostat's shadow is cast on another heliostat surrounding it. To minimize shadowing and blocking effects of the heliostat field the sun angle, tower height, and heliostat spacing all must be considered in the design layout of the field.

A cosine loss is an expression derived from the solar radiation lost by heliostats not being normal to the sun's rays. In a down beam system, the heliostats are orientated such that the rays from the sun reflect to the top of a tower. The difference between the vector required to be normal to the sun's rays and the vector required to reflect to the top of a tower initiates the cosine effect. The energy lost on the heliostat due to the incident angle of the sun is a function of the cosine of the angle away from being perpendicular to the sun's rays [25]. Figure 2.4 depicts the effects of cosine losses.

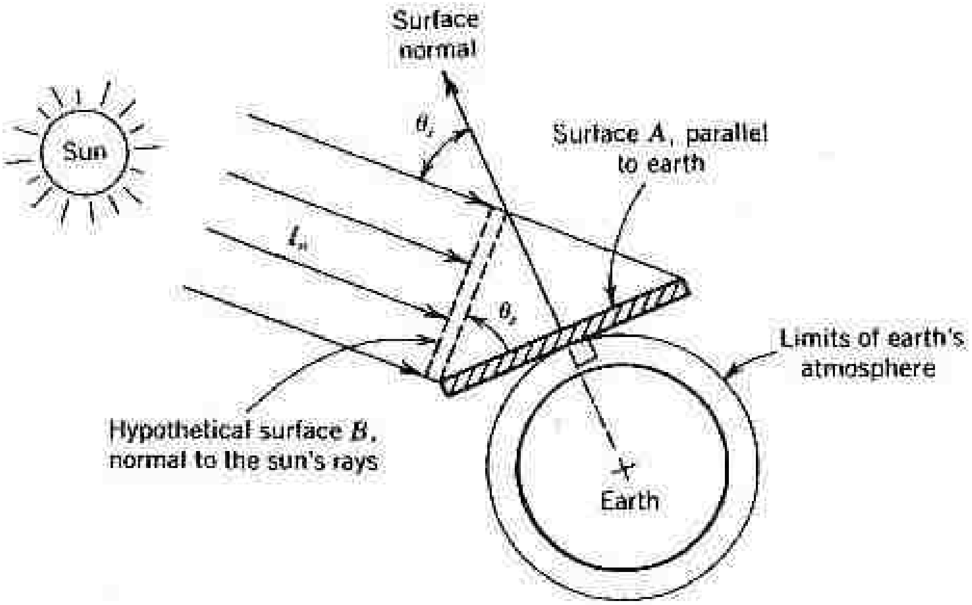

Figure 2.4 Cosine losses as applied to extraterrestrial horizontal irradiance [26]

In Figure 2.4 solar energy is falling on surface A at the same rate as the hypothetical surface B. The figure demonstrates that the projected surface area of the hypothetical surface B is less than the actual surface area of surface A. Therefore, the solar irradiance, or rate at which energy per unit area, falls on surface A is less than that falling on surface B [26]. Ideally, heliostats are arranged to yield maximum cosine efficiency. Such efficiency is dependent on the sun's position and the heliostat's position relative to the tower's receiver. The tracker positions the heliostat so that its normal angle of incidence bisects the beam component of irradiation from the sun and the line of reflectance from the heliostat to the tower's receiver. In an effort to reduce cosine losses, heliostat fields constructed in the Northern Hemisphere are typically orientated to face south, and tall towers are generally constructed.

Blocking, shading, and cosine losses all result in a reduction of the effective heliostat field area. Reflectivity losses, however, are an intrinsic property of the heliostat mirrors. The reflectivity of the heliostat mirrors plays a large role in the heliostat field efficiency. Low absorption mirrors are capable of reflecting the suns beam irradiation at a high efficiency. Of course, over a period of time, this efficiency is reduced by factors such as dust accumulation and age. Therefore, heliostat maintenance becomes pertinent in regards to keeping the mirrors clean and sustainable, allowing them to operate at maximum reflective capability. A further investigation into the reflectivity parameters utilized for modeling the NCSETF is described within the modeling of the facility, section 3.4.2. Blocking, shading, cosine losses, and reflective losses all need to be addressed to effectively simulate the optical performance of a TR system.

Initial design estimates targeted a heliostat field totaling 2,000 m^2 of reflective surface area. This estimation is based on an attainable DNI gauging parameter of 1,000 W/m^2, which is achievable many hours of the year in southern Nevada. At 50% total optical efficiency, accounting for the optical losses discussed, a 2,000 m^2 heliostat field would yield 1 MW of concentrated power at ground level. If focused down to a 1 m^2 spot size, 1,000 suns concentration would be achieved. Further details are presented for the heliostat field when analysis of modeling the facility is presented in Chapter 3, including heliostat relevant dimensions as well as heliostat field layouts.

2.3.4 Ground Collector Element

A ground collection element is a unit to be located at the focal point of the concentrated solar energy. For the primary heliostat field, this collection element will be located directly below the center of the planar down beam reflector at ground level. The targeted collector is envisioned as a large kiln type structure with fixtures for mounting pre-configured solar energy acceptors and experiments. The collection element is intended to be an actively water cooled firebrick assembly.

Coinciding with the ground collection element may be the need for a secondary RC. A secondary RC allows for further processing and focusing of the solar energy before being subjected to the experiment. The secondary RC primarily offers the benefit of further concentration. A secondary RC would need to be developed explicitly to match the operating conditions of the facility. More specifically, it would have to consider the rate of convergence from the down beam mirror to ground level in its design. A secondary RC would require further investigation should it be deemed a necessary asset of the facility. In this thesis, however, the design and analysis of a secondary RC is not considered.

2.3.5 Utilities

Onsite water is necessary for the purpose of cooling experiments. It is envisioned that leased portable water tankers along with pumps and chillers will be utilized. An estimated 30,000 gallons of water is targeted to be available on location. With the facility operating at the targeted 1 MW, 4 hours of operation results in a temperature rise of approximately 40°C in the tank. The water temperature in the tanks can then be brought back down during the night. Longer operating conditions or higher power outputs from the facility may result in the need for additional cooling system components to be brought in.

Onsite electrical power is a necessity for a down beam research facility. Power is proposed to be provided via portable leased generators. If leased, it is not required to bring the facility up to the same electrical code that purchased generators would require. Estimated is the necessity for two 100 kW generators to be available on location. Similar to water tankers, should specific experiments require additional power, supplementary portable generators could easily be provided.

Leased office space and user facilities are also anticipated to be supplied on site. The office space is envisioned as a modular facility with a control room on one end and a small conference room on the other. A modular office of approximate dimensions 60 ft (18.288 m) by 28 ft (8.534 m) is intended for the first phase of implementation of the facility. Temporary user facilities are readily available, and can be added or removed depending on the traffic of the site.

A research facility of such scale as the proposed NCSETF would require both access parking as well as fencing. The fencing serves to provide both security and safety. Access to the site will need to be controlled and restricted. Furthermore, the fence can serve as a barrier from concentrated stray light unintentionally leaving the facility.

As discussed, a modular experimental facility operated by the sponsoring institution is to be supplied onsite. The general user experimental trailer will supply a means for the testing of smaller scale projects, allowing for minimal investment in research assets. Additionally, the onsite modular trailer will monitor operating conditions as well as facility performance. Operating conditions are primarily in the form of weather data, i.e. levels of DNI, temperatures, wind speeds, etc. Facility performance data is anticipated to be in the form of flux maps, power outputs, and concentration ratios received at ground level.

2.3.6 Land Specifications

The compact optics of a planar down beam mirror configuration allows for the facility to be located on relatively minimal land space. Initial investigations led to an approximated 5 acres required to contain the primary heliostat field and experimental facilities. Figure 2.5 portrays the intended site plan and facility dimensions. A site twice the size at 10 acres would be much more optimal, and allow for the expansion of the heliostat field or for a separate field to be constructed.

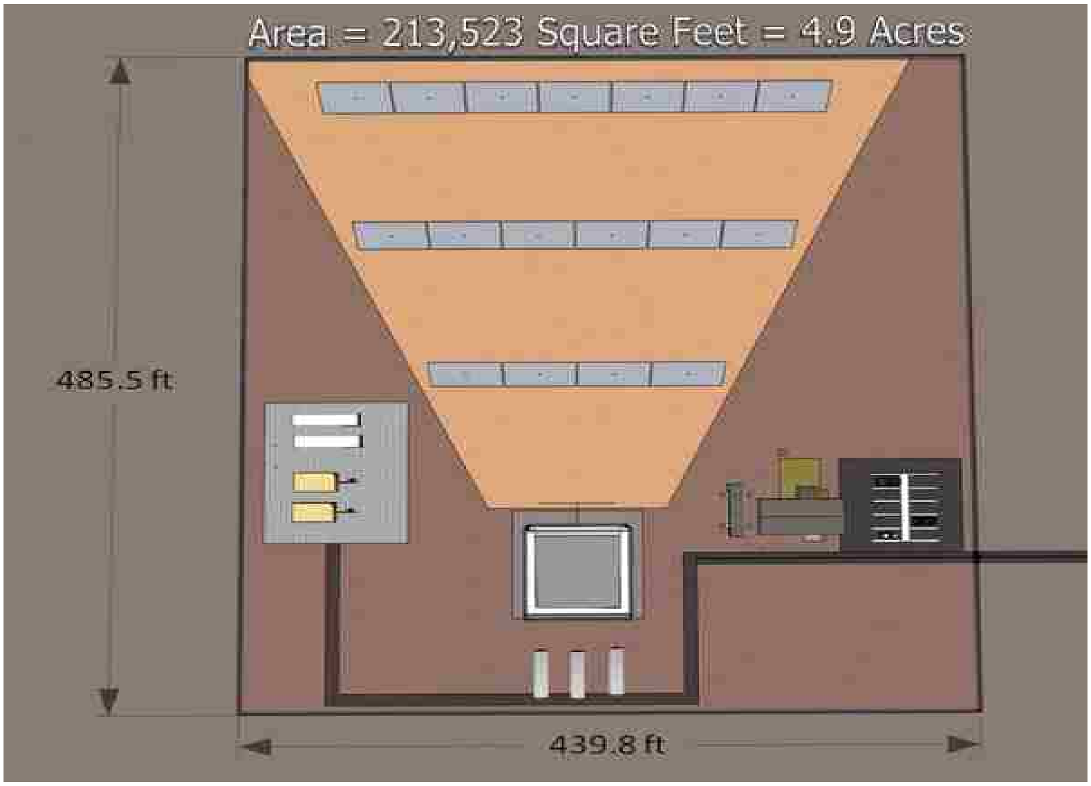

Figure 2.5 Site plan for proposed NCSETF

Various site locations have been investigated for implementation of the NCSETF in southern Nevada. Amongst them include UNLV distinguished professor Dr. Boehm's allocated solar research parcel near Boulder City, adjacent to Nevada Solar One, as well as the recently declared solar testing zone at the Nevada Test Site (NTS). The selection of site location is primarily dependent on the search for funding. Ideal locations will be within close proximity of the sponsoring institution and be both easily accessible as well as highly visible. As described, the height restrictions of Nye County have been taken into consideration in the design of the facility.

CHAPTER 3

MODELING THE NCSETF

3.1 Modeling Approach

The objective in developing a model for the NCSETF was to establish the optical performance of the facility. More specifically, the model was implemented to determine the power output and concentration received at ground level. Consequently, only the optical geometry was simulated within the model, i.e. the heliostat field, down beam mirror, and ground level receiver. The model was approached with the goal of being able to simulate the output of the facility on an hourly basis. In order to do so ray tracing techniques were utilized.

The model was constructed in a format such that it is versatile, easy to use, and allows for the varying of input parameters so their effects can be realized. The user of the model is prompted with changeable simulation conditions, including the simulation hour as well as inputs to construct the optical geometry for the facility. The simulation presented is specific to the design conditions of the NCSETF; however, the model developed is capable of easily modifying the optical geometry. For example, heliostat dimensions, heliostat field layout, and down beam reflector orientation as well as dimensions can all be easily altered. This is a very significant attribute of the model, especially for continuing investigations of the optical geometry in an effort to improve the performance of the facility.

Modeling offers a feasible way to add validity to the design of the system without having to construct and test the facility. Furthermore, it verifies to stakeholders and possible investors that from an optical perspective the facility is capable of producing the targeted output. It is significant to recognize that modeling is only an estimation tool, and the model can only be as accurate as the resources utilized and assumptions made to develop it. Assumptions incorporated into the model are presented as they are applied. Various data sets, software tools, and programming environments were utilized to develop the comprehensive model. The role of each and how they were incorporated into developing the model is presented.

3.2 Software and Modeling Tools

3.2.1 MATLAB®

A MATLAB® programming environment was utilized to construct a large portion of the model. An algorithm was developed to determine the sun's relative position in a 3D spherical coordinate system for any given hour of the year in Las Vegas, Nevada. Heliostat field layout algorithms were implemented to examine the effects of various heliostat locating strategies. Furthermore, the relative orientation as well as the focal distance to achieve the correct optical geometry for each heliostat of NCESETF was all implemented in MATLAB®.

3.2.2 ASAP®

Advanced Systems Analysis Program (ASAP®) is an optical systems simulation and modeling tool developed by Breault Research Organization (BRO) and has been commercially available for over 20 years. ASAP® is able to simulate, by utilizing Monte Carlo ray tracing techniques, the interaction of light with optical and mechanical structures. Rays can automatically be split into reflected, refracted, diffracted, polarized, and scattered components as they propagate through the optical system. The rays proceed independently, following physically realizable paths, encountering objects in the appropriate order as they proceed through the system. This is referred to as "unconstrained" or "non-sequential" ray tracing [27].

In its native form ASAP® is a scripting environment, therefore, some fundamental programming competency is required to effectively utilize the software. Essentially, the syntax categorizes ASAP® as its own distinctive programming language. In an attempt to alleviate some of the frustrations of working with the native scripting syntax, BRO has incorporated a spreadsheet builder to assists users in accurately developing script .inr files. The limitation of the builder is that not all of the ASAP® functionality can be implemented through the builder, such as macros or other types of customizable functionalities, which were all utilized in developing the model for the NCSETF.

In terms of modeling the NCSETF, ASAP® offers a magnitude of functionality. It provides the ability to track and visualize the sun's rays as they travel along their optical path from the sun to the heliostat field, to the down beam mirror, and then to the collector. This allows for the optical geometry of the system to be verified, and the optical losses simulated. The effects of cosine, reflective, blocking, and shadowing losses are all intrinsically represented in the ray trace. Furthermore, ASAP® is capable of accounting for atmospheric attenuation and the scattering of rays by specifying the medium, in this case air, through which the rays are propagating. Additionally, ASAP® is capable of producing power distribution and intensity calculations, as well as 2D and 3D depictions of those calculations, at any location in the optical system. Such calculations prove most useful for measurements on the collector at ground level.

A significant factor in the approach to modeling was based on the fact that ASAP® simulations of the NCSETF are not transient. Therefore, the optical geometry of the system for any given hour of the year was passed into ASAP® as a collection of variables, and the optical results simulated. MATLAB® was utilized to calculate the parameters needed to establish the optical geometry of the facility in ASAP® for any hour of the year.

3.2.3 TMY Weather Data

Typical Meteorological Year (TMY) weather data is utilized to determine the weather conditions for a facility located in southern Nevada, more specifically, the amount of utilizable beam radiation available from the sun for any given hour of the year.

TMY data portrays a set of hourly values of solar radiation and meteorological elements for a one year period. TMY data allows for performance comparisons of system types and configurations for one or multiple locations. TMY data sets are intended for the use in computer simulations of solar energy conversion and building systems, allowing for performance comparisons of different system configurations to be evaluated at various locations in the United States and its territories [28].

The original TMY data represents data for the Typical Meteorological Year as derived from the 1952-1975 SOLMET/ERSATZ data base. The initial TMY data sets covered a total of 234 sites and were created by means of measured solar radiation and temperatures from 26 locations. The additional 208 locations where developed using a correlated model and provided by the United States National Oceanic and Atmospheric Administration (USNOAA). They are based on other meteorological phenomena [28].

The next generation of TMY data, TMY2, was generated from the 1961-1990 National Solar Radiation Data Base (NSRDB). The data covers a total of 239 sites. 56 of these sites where considered primary locations, as they measured solar radiation for at least a part of the 30 year period. The other 186 locations were considered secondary sites, as no solar radiation measurements were taken from those locations. The secondary sites were derived from meteorological data and portray modeled solar radiation data. TMY2 data was produced and is supplied by NREL [28].

The most recent TMY data sets, TMY3 data sets, represents 1,020 sites in the United States and its territories and were developed by NREL's 1991-2005 Electrical System Center under the Solar Resource Characterization Project [28]. The TMY3 data set for Las Vegas McCarren International Airport is utilized in modeling of the NCSETF. The McCarren location is a Class I dataset, implying that it has the lowest amount of uncertainty data and is therefore amongst the most accurate class of TMY3 data sets. In TMY3 data sets DNI is measured as the amount of solar radiation received in a collimated beam on a surface normal to the sun during a sixty minute period ending at the timestamp presented in the data [28].

It is crucial to recognize that TMY data represents typical weather conditions rather than extreme conditions, and therefore should not be used in the modeling of worst or best case circumstances. For the purpose of modeling the NCSETF, in which typical performance of the facility is desired, TMY3 is a very suitable dataset.

3.3 Simulating the Sun

3.3.1 Sun's Position

In order for the NCSETF to be modeled on an hourly basis, the sun's location relative to a facility implemented in southern Nevada needed to be determined for every hour of the year. First, the exact location of the facility was specified by utilizing the latitude, ϕ, and longitude, φ, of Las Vegas McCarren International Airport as reported in the TMY3 dataset. The latitude and longitude of the McCarren International Airport are 36.083° and -115.15°, respectively.

The relative direction from which the sun's rays are emitting can be established in a 3D spherical coordinate system with knowledge of the solar zenith angle, θ_z, and the solar azimuth angle, γ_s. The solar zenith angle is representative of the angle between a vertical line and a line directly to the sun. If beam radiation from the sun is projected on a horizontal surface, the solar azimuth angle is the angular displacement from south of that projection. West of south is considered positive and east of south is considered negative [29]. A graphical depiction of the solar zenith angle, θ_z, and the solar azimuth angle, γ_s, is presented in Figure 3.1. Figure 3.1 is followed by the formulation used to derive the solar zenith and solar azimuth angle of the sun on an hourly basis, allowing for the sun's relative position to be simulated within the model.

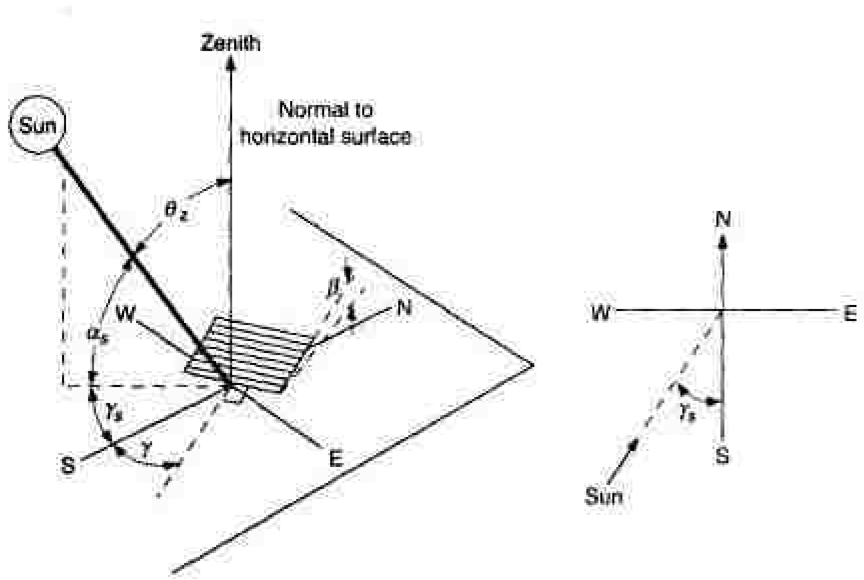

Figure 3.1 Solar zenith angle, θ_z, and solar azimuth angle, γ_s [29]

The declination of the sun, δ, was initially established on a daily basis. A declination angle arises from the tilt of the earth on its axis of rotation as it rotates around the sun. The declination angle ranges from 23.45° on the summer solstice, June 21, to -23.45° on the winter solstice, December 22. For the fall equinox, September 23, and the spring equinox, March 22, the declination angle is 0°. A precise approximation for the declination of the sun, accurate to 0.035°, is described by equation (3.1) [29]:

$$\begin{aligned}\delta = (180/\pi)(&0.006918 - 0.399912\cos(B) + 0.070257\sin(B)\\ &-0.006758\cos(2B) + 0.000907\sin(2B)\\ &-0.002697\cos(3B) + 0.00148\sin(3B))\end{aligned} \tag{3.1}$$

Where (3.2),

$$B = (n-1)\frac{360}{365} \tag{3.2}$$

In equation (3.2), *n*, is representative of the day of the year. Upon implementation of the MATLAB® code a prompt specifies for the input of a month, day, and hour for the simulation. Based on the user input month parameter an index is established for the day of the year. Therefore, the following formulation is used to establish *n*, an array containing the day of the year for every hour of the month selected for simulation (3.3):

$$n = index + ceil\left(\frac{hour}{24}\right) \tag{3.3}$$

In equation (3.3), *hour*, is a vector array containing the number of hours in the month selected for simulation. Additionally, *index*, is a base parameter establishing the number of days in the year up to the time of the specified month. Furthermore, *ceil*, is a rounding operator to round up to the nearest day integer. The angular displacement of the sun east or west of the local meridian due to the rotation of the earth on its axis is referred to as the hourly angle, ω [29]. The hourly angle varies 15° per hour, ranging from -180° at midnight to 180° at noon. A vector containing the hourly angle for every hour of the selected simulated month is represented by (3.4):

$$\omega = -180 + 15(hour - 24(n - (index + 1))) \tag{3.4}$$

With numerical representations for the latitude, declination, and hourly angle, the sun's zenith angle can be determined for any hour of the year according to the following equation (3.5) [29]:

$$\theta_z = \cos^{-1}\left(\cos(\phi)\cos(\delta)\cos(\omega) + \sin(\phi)\sin(\delta)\right) \tag{3.5}$$

Similarly, once the zenith angle has been calculated the azimuth angle can be determined for any hour of the year according to equation (3.6):

$$\gamma_s = \begin{cases} -\left|\cos^{-1}\left(\dfrac{\cos(\theta_z)\sin(\phi) - \sin(\delta)}{\sin(\theta_z)\cos(\phi)}\right)\right| & \mathit{for} \quad \omega < 0 \\ \\ \left|\cos^{-1}\left(\dfrac{\cos(\theta_z)\sin(\phi) - \sin(\delta)}{\sin(\theta_z)\cos(\phi)}\right)\right| & \mathit{for} \quad \omega \geq 0 \end{cases} \tag{3.6}$$

3.3.2 Modeling the Sun's Rays

With a method established for determining the solar azimuth and zenith angles, a Sun Position Orientation (SPO) algorithm was developed in MATLAB® that exports a data file to the root directory of ASAP® for utilization in modeling the optical geometry of the NCSETF. The data file produced by the SPO algorithm contains a vector of three hourly varying parameters needed to define the sun for a given modeled hour. They include the solar azimuth angle, solar zenith angle, and DNI for the specified simulation hour. TMY3 data for McCarren International Airport comes in a Microsoft Excel spreadsheet format, with hourly DNI data contained in one of the columns. The SPO algorithm reads in the appropriate DNI value based on an hourly index for the month selected, and then exports the three required parameters to be utilized in ASAP® for modeling the sun for the specified sample hour.

Initially, the sun's rays were simulated in the ASAP® model of the NCSETF as a grid of parallel rays emitting from the appropriate direction of the sun. Once the solar azimuth angle, solar zenith angle, and DNI values for the modeled hour have been allocated in ASAP®, an arbitrary distance to place the source of the sun's rays is specified. This arbitrary distance, *R*, was set to 400 m for modeling the NCSETF. Direction cosines for emitting rays back towards the heliostat field can then be specified in spherical coordinates according to the following equations (3.7):

$$\begin{aligned} A &= -R\cos(\gamma_s)\sin(\theta_z) \\ B &= -R\sin(\gamma_s)\sin(\theta_z) \\ C &= -R\cos(\theta_z) \end{aligned} \tag{3.7}$$

In ASAP®, objects are positioned by specifying their x, y, and z location, as well as the object's respective rotation around an arbitrarily defined axis in a 3D Cartesian coordinate system. The axes in the ASAP® model of the NCSETF are orientated such that the positive x-axis points north, the positive z-axis points east, and the positive y-axis is normal to the earth's surface. It is assumed that the facility is located on a flat horizontal surface. The sun object is initially defined as a grid of parallel rays on the plane of the x-axis at the origin. The sun grid is then shifted *A* in the x direction, –*C* in the y direction (i.e. gravitation direction), and *B* in the z direction to match the coordinates of the ASAP® model.

With the sun's location defined, the required rotation of the sun's object to emit rays back towards the origin is addressed. First, the sun source is rotated $-\left(90^\circ - \theta_z\right)$ about a z-axis, displaced *A* in the x direction and –*C* in the y direction. The source is then rotated $-\gamma_s$ about a y-axis, displaced A in the x direction and B in the z direction. Parallel rays are then emitted from the sun source towards the origin.

The sun source object in ASAP® is depicted as an elliptical grid of parallel rays sized large enough to cover the entire heliostat field. In ASAP®, flux is defined as energy per unit time (J/s = W). Therefore, a scaling parameter had to be introduced to maintain proper DNI (W/m^2) as the size of the elliptical sun source was modified to cover the entire heliostat field. The following expression is utilized to scale the flux in ASAP® and preserve proper DNI for the model (3.8):

$$Scaled\ Flux = (S_r)^2 (DNI)\pi \tag{3.8}$$

where,

S_r = Radius of the elliptical grid sun source (m)
DNI = Direct Normal Irradiance for simulation hour (W/m^2)

The total wattage of the elliptical sun source, as determined by equation (3.8), is then able to be emitted towards the heliostat field within the model. The wattage is evenly distributed amongst the rays implemented in the ray trace. At this stage, it is important to identify that up to this point the model has been assuming rays from the sun are parallel, as if emitting from a point source. In actuality, not all of the sun's rays are parallel, but instead demonstrate divergence behavior as they propagate through the system. The development of a realistic solar disk within the model is the focus of section 3.3.3.

3.3.3 Realistic Solar Disk

Considering the sun's rays as parallel implies they are emitting from a point source. Such an assumption is slightly inaccurate; however, often assumed appropriate since the sun is so far away. A true image of the sun produces a spot size that has an obvious width. This spot size is a product of not all of the sun's rays being parallel. The angular diameter of the sun in the sky, S_{AD}, can be approximated with knowledge of the sun's diameter, 1,392,000 km, and distance from the earth, 149,600,000 km, according to the following relation (3.9):

$$S_{AD} \approx \frac{360^{\circ}}{2\pi} \frac{1,392,000\ km}{149,600,000\ km} \approx 0.5^{\circ} \tag{3.9}$$

Therefore, the total angular aperture of the sun in the sky is approximately 0.5°. Figure 3.2 presents a graphical depiction of the divergence characteristics of the sun's rays.

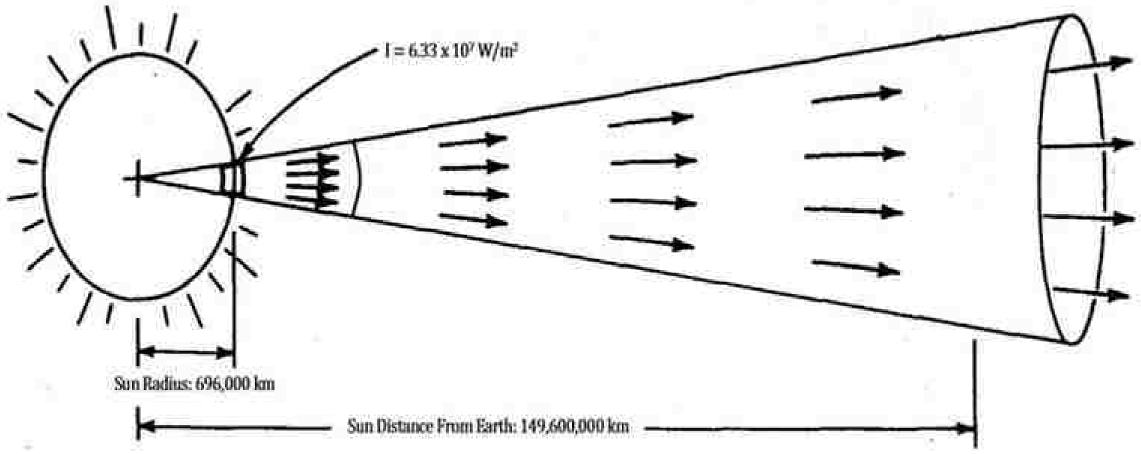

Figure 3.2 Divergence characteristics of solar rays

In order to simulate divergence behavior of the sun's rays, as they reflect off the heliostats within the ASAP® model of the NCSETF, a scattering surface was utilized. To develop the scattering surface a user defined bi-directional scattering distribution function (BSDF) was required. For the specific case of modeling the NCSETF, in which all the solar radiation is desired to be transmitted and not reflected through the scattering surface, such a function can be considered a bi-directional transmittance distribution function (BTDF). The user defined BSDF utilized in simulating the angular diameter of the sun in the sky is described by equation (3.10):

$$USERBSDF = \frac{1}{\pi * S_{HAR} * S_{HAR}} \tag{3.10}$$

where,

S_{HAR} portrays the half angle of the sun in radians and is represented by equation (3.11):

$$S_{HAR} = \frac{\pi}{360} * S_{AD} \tag{3.11}$$

Such a BSDF allows for an isotropic scattering surface to be created within ASAP®. The scattering surface is placed directly in the path of the previously developed grid of parallel rays, emitting from a coordinate in the celestial sphere as defined by the sun position vector for any given simulation hour. The scattering surface is equal in size to the grid of parallel rays. As solar rays transmit through the scattering surface they are given a finite scatter angle ranging from 0° to a maximum of 0.5°. This allows for the rays to be scattered into a circular cone centered in the specular direction and directed towards the heliostat field. The methodology behind constructing the scattering surface was based on a previously established script .inr file developed by the ASAP® development team for simulating the behavior of the sun's rays within a ray trace. Figure 3.3 is a graphical depiction of the scattering surface implemented within the ASAP® simulation of the NCSETF. Figure 3.3 is taken during the middle of a ray trace. The black speckles on the disk portray rays interacting with the scattering surface.

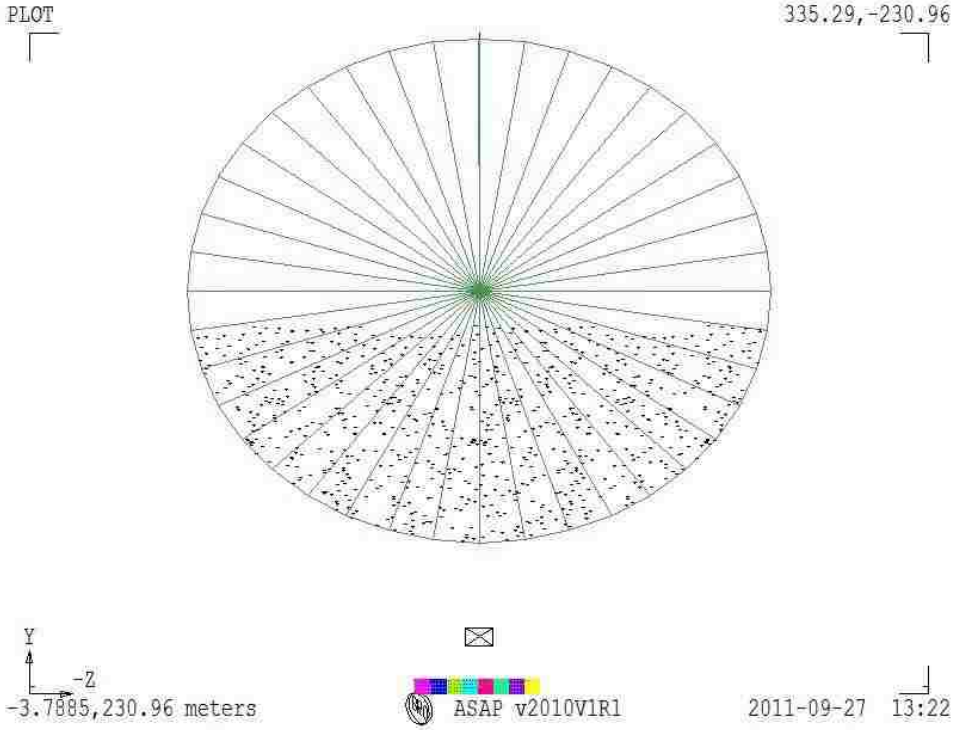

Figure 3.3 ASAP® scattering surface for diverging solar rays

The implementation of a realistic solar disk within the model is intended to simulate the achievability of practical concentration ratios for the NCSETF. Divergence characteristics are expected to have little to no effect on the power output, but a significant effect on attainable concentration ratios. Since the rays of the sun are not all parallel, an idealized point source overestimates practical concentration ratios by allowing for focusing conditions to a point instead of an area.

The NCSETF was designed with a heliostat field close to the tower. This was to limit the concentration losses that increase as the focal length for each heliostat grows due to the angular diameter of the sun. The use of parallel rays does not account for this effect within the simulated model. Implementation of a realistic sun source allows for real world limitations on the achievable concentration of the facility to be realized. Simulation results are presented in Chapter 4 for both parallel and diverging rays, allowing for the effects on power and obtainable concentration to be both recognized and compared.

3.4 Optical Geometry

3.4.1 Down Beam Reflector

The dimension of the planar down beam reflector utilized for initial modeling of the NCSETF was 18 m long by 14 m wide. The dimensions were based on a realistic combination of optical and physical considerations. On one hand, the mirror needed to be large enough to focus the rays of a heliostat field capable in size of reaching the targeted output of the facility. On the other hand, the down beam mirror couldn’t be so large that it became infeasible to construct. The dimensions specified were deemed appropriate for initial investigations of the facility.

The center of the mirror is located 25.6 m above the center height of the heliostat field and rotated 32.1° to favor a south facing heliostat field. The relatively short height of the down beam reflector is based on two factors. A shorter tower height minimizes construction costs of the tower. Additionally, it allows for consideration of the NCSETF to be implemented in Nye County by abiding to the height restrictions. Several considerations also went into the rotation of the down beam reflector. Partially, the rotation was based on optimal orientation at solar noon, with the TR, sun, and a line down the center of the heliostat field all being co-liner. Furthermore, since the physical footprint of the facility was targeted to be containable within 5 acres, a compact heliostat field close to the tower was a necessity. The 32.1° rotation allows for a heliostat field relatively close to the tower, but far enough away to accommodate a reasonably sized heliostat field capable of achieving the target output and the focal point centered below the down beam mirror. Figure 3.4 is a drawing depicting the optical characteristics for the geometry and orientation of the down beam reflector used in modeling the NCSETF.

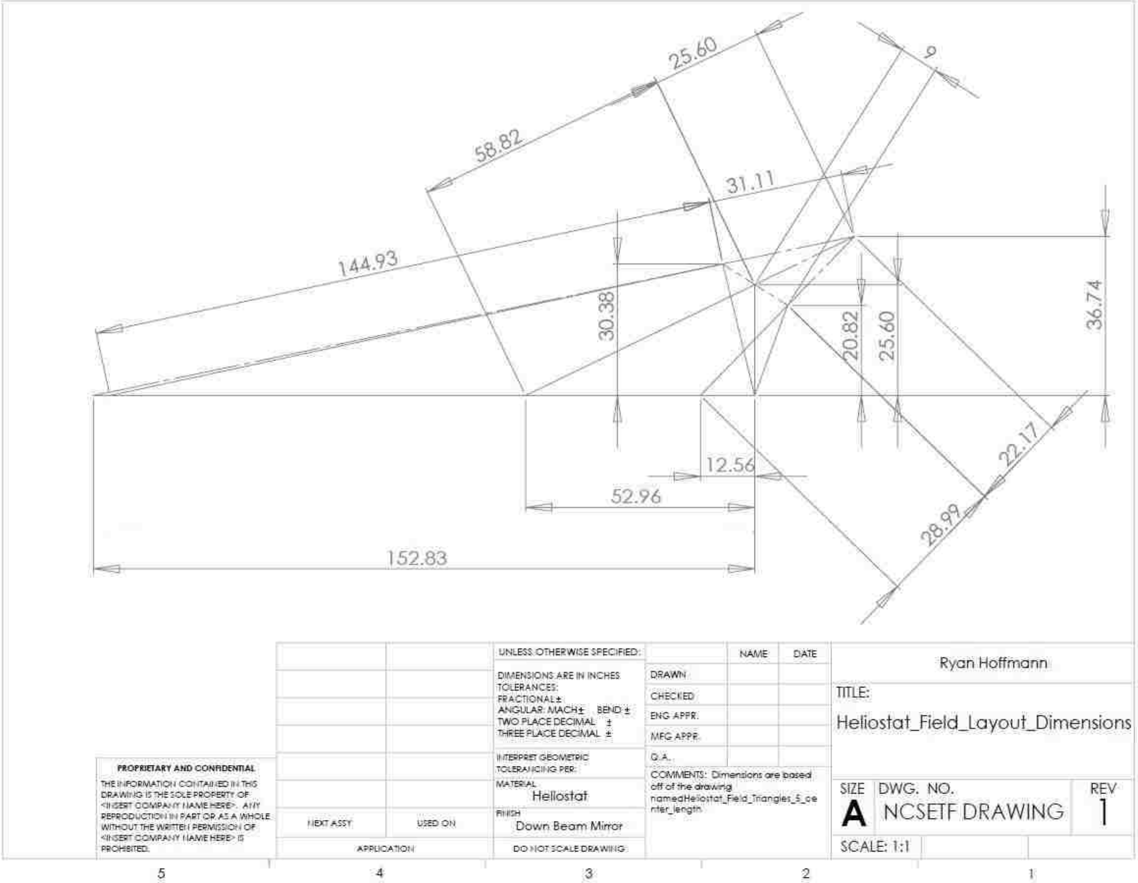

Figure 3.4 Optical geometry for NSCETF down beam reflector [unit: m]

The size and orientation of the down beam reflector yields an AP for the heliostat field located 23.05 m behind and 11.14 m above the center of the down beam mirror, as described in Figure 3.4. Furthermore, the drawing also demonstrates that the first row of heliostats capable of reflecting rays to the focal point is located 12.56 m in front of the center of the down beam mirror, while the last ray is located 152.83 m in front of the center of the down beam reflector.

Advancements in mirror glass and reflective films have allowed for the development of highly reflective mirrors. It is assumed that the down beam mirror is capable of achieving and maintaining 96% specular reflectivity. This assumption is based off of manufacturer 3M’s Solar Mirror Film 1100, capable of exceeding 94% total hemispherical reflectance, and specular reflectance above 95%. The reflective film, a silver metalized and weatherable acrylic, is designed specifically for the utilization in concentrating solar collectors [30].

3.4.2 Heliostats

Initial investigations of the heliostat field led to a determination of 8 x 8 m heliostats to be utilized in simulating the facility. The reflectivity established for the heliostat is the same as that specified for the down beam reflector, 96% specular. The heliostat dimensions were based on collaborations with Nabtesco Motion Control, a manufacturer of high precision gearboxes utilized in solar tracking devices. Drive units account for approximately 50% of the manufacturing costs of heliostats. Therefore, motion controls play a significant role in the selection process of heliostats. With a working relationship established with Nabtesco, it was concluded that initial modeling of the heliostats should incorporate a design that could be implemented with Nabtesco tracking units. It was specified by Nabtesco that their drive units could accurately accommodate 60-75 m^2 in heliostat reflective surface area. Subsequently, square heliostats of reflective surface area 64 m^2 were selected for modeling of the facility. However, the model developed was constructed in such a manner that allows for the dimensions of the heliostats to be modified according to user input parameters. The thought process was that future optimization of the facility would undoubtedly include the investigations of varying heliostat dimensions. Therefore, a model implementation capable of easily adjusting the size of heliostats and subsequently realizing the effects was deemed necessary.

Utilizing a Newtonian optical system, there is a limited land area for which heliostats can be placed and still effectively utilized. Separately stated, the rays reflected from any given heliostat towards the AP must be able to be intercepted by the down beam reflector in order to redirect the sun's rays to the focal point at ground level. This physical footprint was determined by drawing a line from the AP to the four corners of the down beam mirror, and then extending each of those lines to the height of the heliostat field at ground level. The result is a trapezoid at ground level for which heliostats can be placed and effectively utilized within the system. Figure 3.5 demonstrates the trapezoid generated from such a technique.

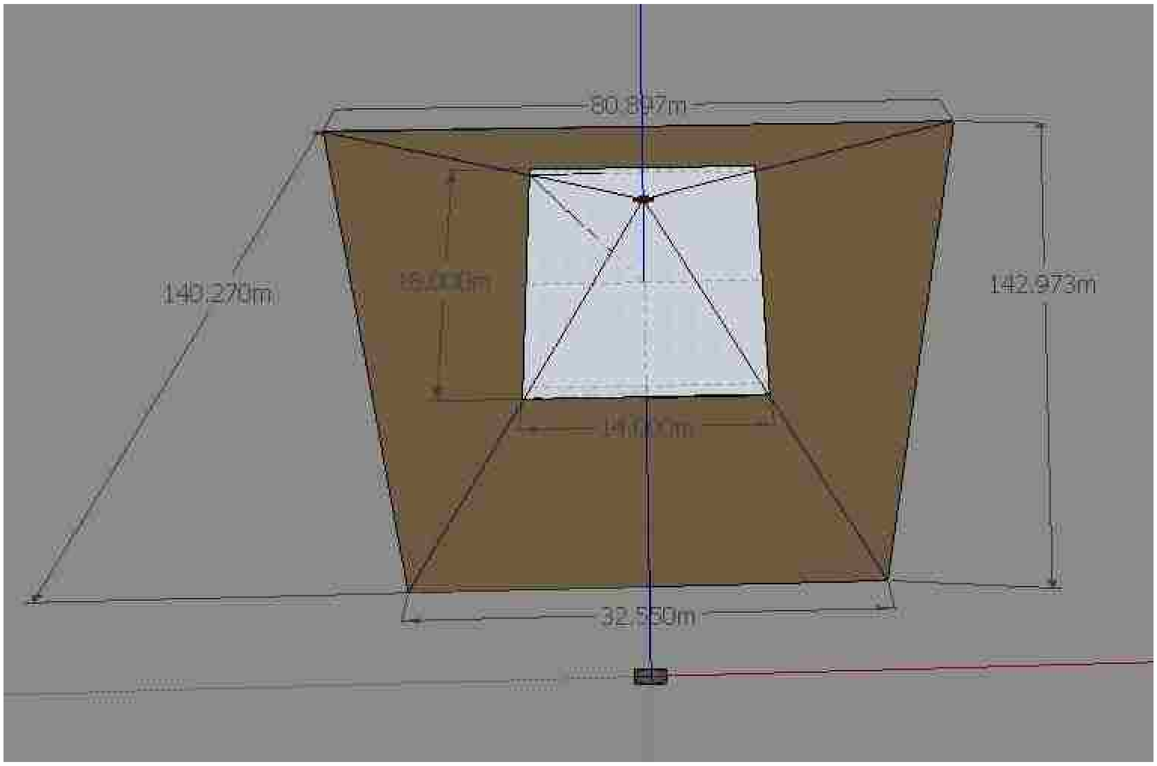

Figure 3.5 Trapezoid demonstrating utilizable placement of heliostats

The diagram in Figure 3.5 depicts approximately 7,960 m^2 of utilizable land area for placing heliostats capable of reflecting to the focal point for the given optical geometry of the NCSETF. Methodologies for how heliostats were positioned within that land area is presented under heliostat field layouts, section 3.7.

3.5 Heliostat Reflection Equations

A Heliostat Reflection Orientation Position Vector (HROPV) algorithm was developed to appropriately orientate each heliostat to reflect to the AP of the heliostat field for every hour of the year. Using the coordinates for the center of each heliostat in a 3D coordinate system, the algorithm orientates each heliostat to properly reflect to the AP. The orientation of the heliostat is time dependent based on the sun's position. The mathematical equations utilized to accurately orientate each heliostat are described.

A plane of reflection for each heliostat is defined by the center point of the heliostat, sun, and targeted AP, as depicted in Figure 3.6. The center of the heliostat and targeted AP are at fixed locations for any given simulation hour. The center of the sun, however, at the apex of the reflection plane, varies as the earth rotates. In order for the heliostat to properly reflect to the AP, the normal position vector to the heliostat must lie halfway between the sun and the AP in the plane of reflection [31].

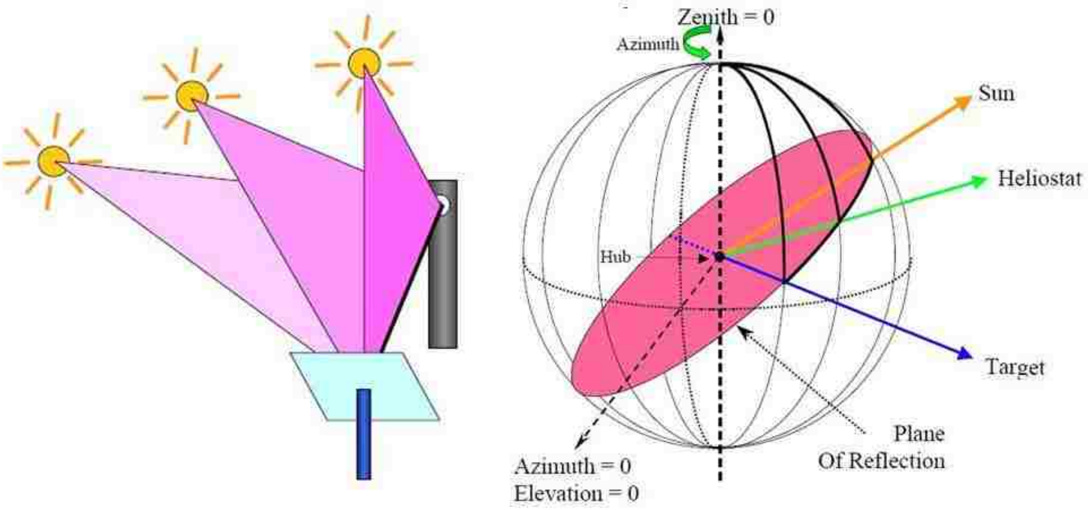

Figure 3.6 Plane of reflection for heliostats [31]

Figure 3.6 demonstrates that the plane of reflection rotates around the target vector, and is orientated based on the sun's position in the sky. The target vector is a function of each heliostat's location. As described by Leonard [31], the law of sines and the law of cosines are required to determine the heliostat positioning vector. This can be accomplished by a process known as triangulation, utilizing the known sun and target positioning vectors for any given time stamp. In a spherical coordinate system, the heliostat, sun, and target position vectors are defined by each of their zenith and azimuth angles respectively. Figure 3.7 represents the geometry in a spherical coordinate system.

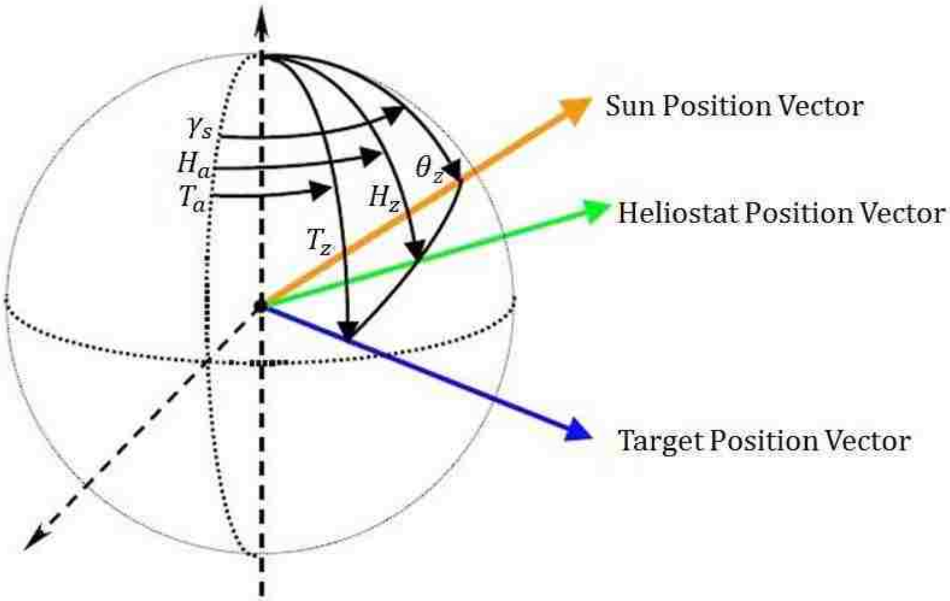

Figure 3.7 Vector position geometry for target, heliostat, and sun

The law of sines states that the sides of a triangle are in the same ratio to one another as the sines of their opposite angles. The law of cosines is a method for calculating a specific side of a triangle when the other two sides and opposite angle are known, or computing the angles of a triangle when all three sides are known. Figure 3.7 represents a non-Euclidean geometry, therefore, in a spherical coordinate system, the law of sines and the law of cosines theorems are adapted to relate the sides and angles of spherical triangles. Consider the following spherical triangle:

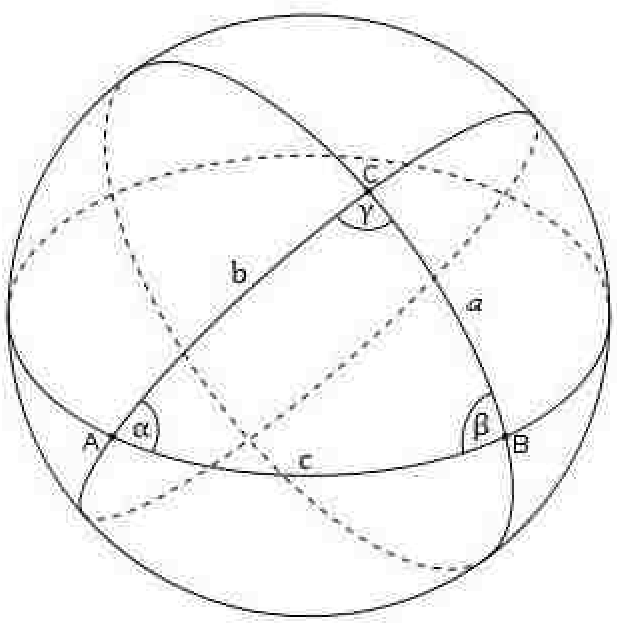

Figure 3.8 Triangle in spherical coordinates [31]

The law of sines in spherical coordinates states (3.12) [32]:

$$\frac{\sin\alpha}{\sin a}=\frac{\sin\beta}{\sin b}=\frac{\sin\gamma}{\sin c} \tag{3.12}$$

Similarly, the law of cosines in spherical coordinates states that the angles of a spherical triangle are represented by (3.13) [32]:

$$\begin{aligned}\cos\alpha&=-\cos\beta\cos\gamma+\sin\beta\sin\gamma\cos a\\ \cos\beta&=-\cos\gamma\cos\alpha+\sin\gamma\sin\alpha\cos b\\ \cos\gamma&=-\cos\alpha\cos\beta+\sin\alpha\sin\beta\cos c\end{aligned} \tag{3.13}$$

The law of cosines in spherical coordinates also states the angular length of the sides of the triangle (3.14) [32]:

$$\begin{aligned}\cos a &= \cos b \cos c + \sin b \sin c \cos \alpha \\ \cos b &= \cos c \cos a + \sin c \sin a \cos \beta \\ \cos c &= \cos a \cos b + \sin a \sin b \cos \gamma\end{aligned} \tag{3.14}$$

The geometry of the heliostat, sun, and target position vectors create two spherical triangles in 3D space. Figure 3.9 defines those spherical triangles:

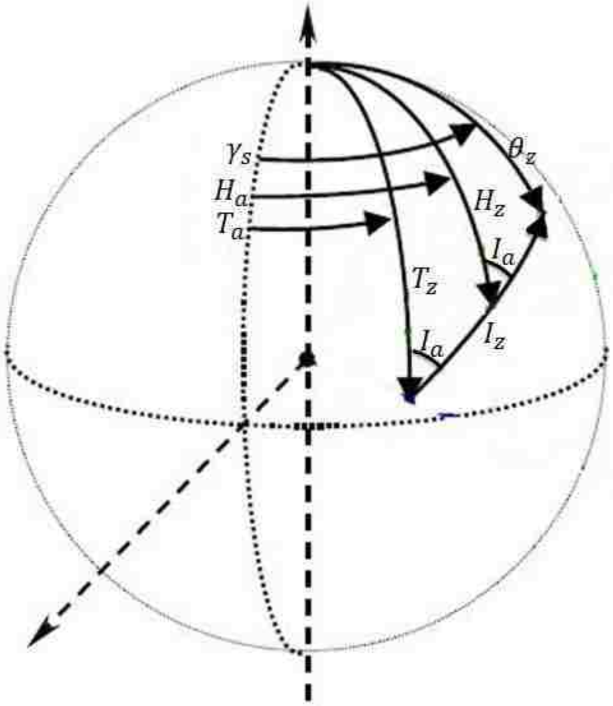

Figure 3.9 Spherical triangles created by heliostat, sun, and target position vectors

The solar azimuth angle, γ_s, and solar zenith angle, θ_z, are known on an hourly basis based on the calculated position of the sun as described by the SPO algorithm in section 3.3.1. The target azimuth angle, T_a, and the target zenith angle, T_z, are also known and calculated by the HROPV algorithm based on the x, y, and z location of each heliostat in a 3D Cartesian coordinate system. Therefore, the law of sines and law of cosines can be applied to the spherical triangles to solve for the heliostat azimuth angle,

H_a, and the heliostat zenith angle, H_z. As described by Leonard [31], the angles are calculated in a two-step process. The first step involves calculating the angle between the target and the sun, $I_{z.}$, so the halfway point for which the heliostat position vector must point can be determined. The law of cosines is applied to calculate I_z according to the following equation (3.15) [31]:

$$I_z = \cos^{-1}\left(\cos(\theta_z)\cos(T_z) + \sin(\theta_z)\sin(T_z)\cos(\gamma_s - T_a)\right) \tag{3.15}$$

The law of sines gives the relationship (3.16) [31]:

$$\frac{\sin(\gamma_s - T_a)}{\sin(I_z)} = \frac{\sin(I_a)}{\sin(\theta_z)} \tag{3.16}$$

Solving for the common intermediate angle, I_a, yields (3.17) [31]:

$$I_a = \sin^{-1}\left(\sin(\theta_z)\frac{\sin(\gamma_s - T_a)}{\sin(I_z)}\right) \tag{3.17}$$

With the intermediate values determined, the desired heliostat azimuth angle, H_a, and the heliostat zenith angle, H_z can be calculated. Again, using the law of cosines H_z can be solved for via (3.18) [31]:

$$H_z = \cos^{-1}\left(\cos(T_z)\cos\left(\frac{I_z}{2}\right) + \sin(T_z)\sin\left(\frac{I_z}{2}\right)\cos(I_a)\right) \tag{3.18}$$

The law of sines gives the relationship (3.19) [31]:

$$\frac{\sin(H_a - T_a)}{\sin\left(\frac{I_z}{2}\right)} = \frac{\sin(I_a)}{\sin(H_z)} \tag{3.19}$$

Finally, the heliostat azimuth angle, H_a, is represented by the equation (3.20) [31]:

$$H_a = \sin^{-1}\left(\sin\left(\frac{I_z}{2} \right) \frac{\sin(I_a)}{\sin(H_z)} \right) + T_a \qquad (3.20)$$

Based on the known coordinates for each heliostat, an arbitrary reference set of x, y, and z axes is defined, with the origin located at the center of each heliostat. Each heliostat is then respectively rotated about its arbitrarily defined reference axis the appropriate amount to achieve the correct positioning vector, defined by H_z and H_a. The MATLAB® code implements a data file in the root directory of ASAP® containing the x, y, and z location of each heliostat, as determined by one of the heliostat field layout algorithms to be discussed in section 3.7. This data file also contains the respective rotation of each heliostat required to achieve the appropriate heliostat position vector, as determined by the HROPV algorithm. The resulting data file contains six initial parameters for each heliostat: x, y, and z locations, as well as the rotation around each respective arbitrary axis.

A user defined macro in ASAP® then reads in the heliostats data file, and assigns each of the parameters to a unique variable, similar to how the sun source was implemented. The location and orientation of each heliostat is then realized in ASAP®, and the optical properties applied. This allows for the facility to be optically simulated for any given hour of the year.

3.6 Converging Heliostats

In order for the optical system, which utilizes a planar down beam reflector, to achieve the targeted concentration and power output within a reasonable spot size at ground level, converging heliostats were implemented. With an idealized point source emitting parallel rays the achievability of 1,000 suns concentration would require the overlapping of more than 1,000 planar heliostat images. With a desired spot size as close to 1 m^2 as possible, heliostats would have to be 1 m^2 or smaller in area. Instead, the model was developed using focusing heliostats, capable of covering the sun's rays to obtain additional concentration.

From a feasibility of manufacturing perspective, a non-imaging heliostat that focuses the sun's rays would likely be implemented using the method described by Chen [33]. Such a heliostat is composed of a flat master frame covered with faceted mirror tiles. The master frame is orientated such that it achieves the heliostat position vector, and the individual mirror facets are orientated to achieve focus. The advantage to such a design is that heliostats can be mass produced, since each heliostat is able to achieve varying focal points by adjusting the individually faceted mirror tiles. Figure 3.10 depicts the heliostat as described by Chen [33].

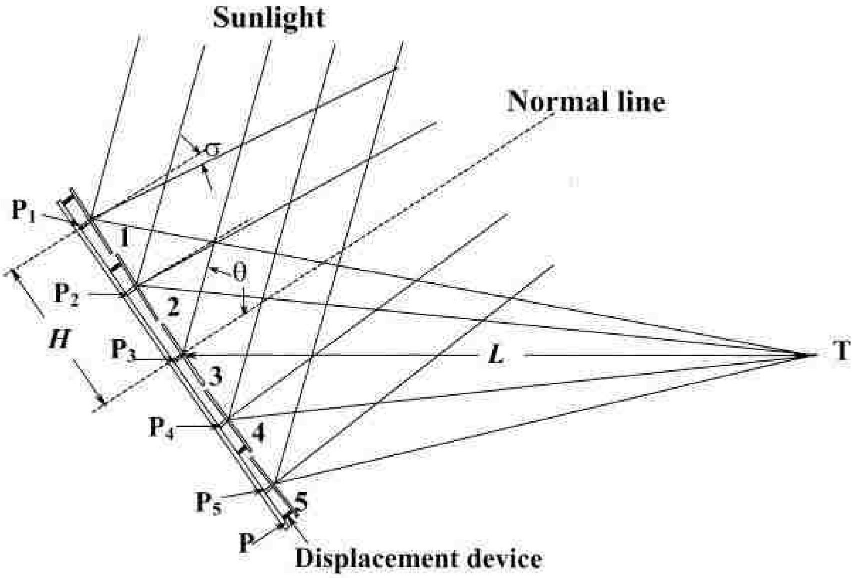

Figure 3.10 Non-imaging focusing heliostat schematic [33]

A limitation of ASAP® was encountered in the effort to implement focusing heliostats as described by Chen [33]. ASAP® contains 1,768 internal register values [27]. The implication is that only 1,768 variables can be assigned within ASAP® for any given optical simulation. In order to model a heliostat as defined by Chen [33], each mirror tile would essentially have to be simulated as an individual small planar heliostat. With 1 m^2 tiles, the minimal targeted size heliostat field of 2,000 m^2 would require the assignment of more than 12,000 variables, exceeding the upper limit of the internal register values available in ASAP®. Subsequently, alternate approaches had to be investigated for simulating focusing heliostats within the ASAP® model of the NCSETF.

A feasible approach, adhering to the restrictions of ASAP®, was developed for modeling converging heliostats. ASAP® is capable of taking a planar object and making it of parabolic shape by applying a vertex radius of curvature. The vertex radius of curvature is defined by the focal length of each heliostat. For any given heliostat, the focal length is equivalent to the length of the target positioning vector, a value previously calculated within the HROPV algorithm for defining the heliostat reflection equations. Utilizing the known focal length, along with the number of facets along the length and width of the object, a rectangular aperture can be used to simulate a converging heliostat in ASAP®. Figure 3.11 demonstrates a converging heliostat as defined in the ASAP® model of the NCSETF.

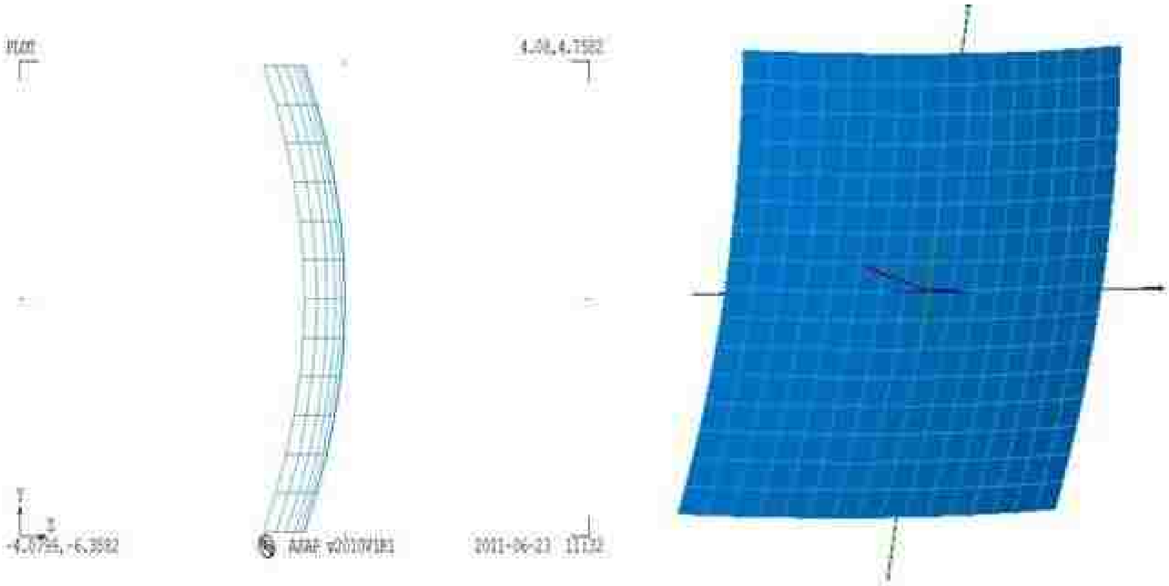

Figure 3.11 Faceted converging heliostat ASAP® schematic

In order to fabricate an object representative of a heliostat like that presented in Figure 3.11 ASAP® requires the input of a conic constant. Since the conic constant is the same for all heliostats, it can be specified in ASAP® and does not have to be imported. A conic constant of zero, representative of a sphere, was chosen in creating the heliostat objects for the model.

The method developed requires one additional variable per heliostat, the radius of curvature, to be imported from MATLAB® into ASAP® in order to simulate heliostat convergence characteristics. It also requires the number of facets along the length and width of the heliostats, which is imported as two parameters for the entire heliostat field. The model created prompts the user to input the number of facets for any given simulation. Again, this was done in an effort to make the model versatile, allowing for the effects of various facet sizes to be easily realized. It should be noted that the facets are only utilized for viewing purposes. Less facets make the rendering of 3D simulations easier to manipulate and quicker to construct. It was originally envisioned that the facet sizes could be adjusted to render different size mirror tiles of converging heliostats. In ASAP®, however, the number of facets used to render the object has no impact on the object's physical definition within the database. The numbers of facets affects only the graphics, and therefore have no influence on how rays interact with the object. In terms of modeling the NCSETF, facets were specified to produce 1 m^2 mirror tiles. Dimensions were based on attempting to match visible characteristics with feasibility of implementation.

The approach utilized for developing converging heliostats in ASAP® present two primary drawbacks. Predominantly, additional optical aberrations are introduced as a result of off-focus orientations required for tracking of the sun. Essentially, the converging heliostats are constructed as dishes with the correct focal distance, rather than true non-imaging heliostats as Chen [33] describes. Additionally, from a manufacturing perspective, each heliostat would have to be custom fabricated based on its exact radius of curvature. This would have to be done for the entire heliostat field, and once a heliostat is placed it can't be moved without distorting the optical geometry. Figure 3.12 is a ray trace implemented in ASAP® to demonstrate the convergence characteristics of a heliostat developed by the method described.

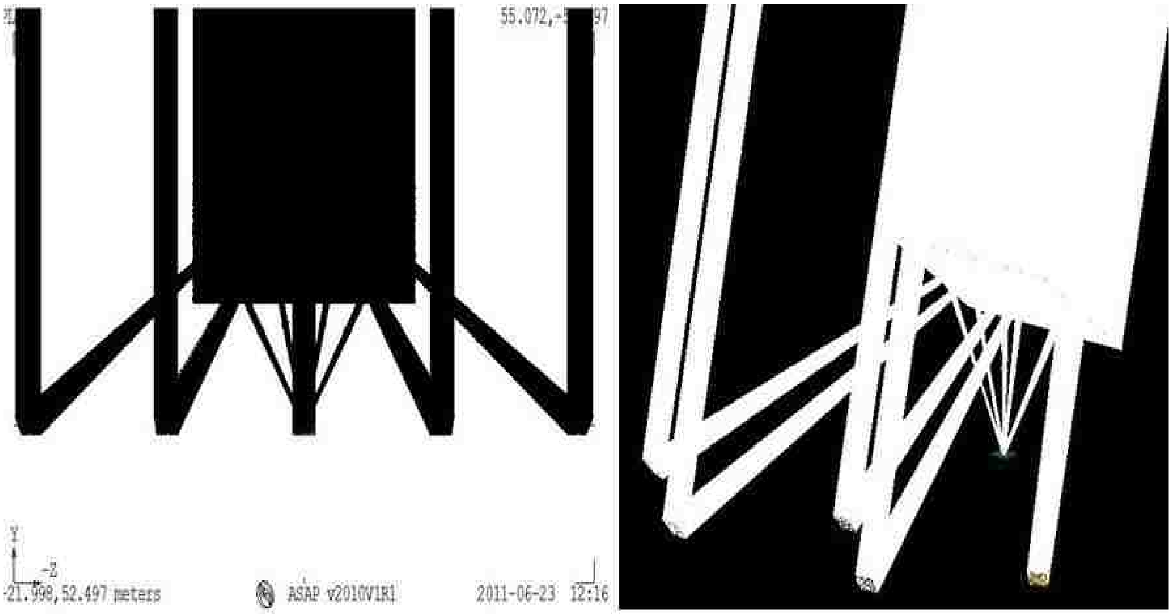

Figure 3.12 Ray trace demonstrating converging heliostats in ASAP®

3.7 Heliostat Field Layouts

3.7.1 Methodology

Two separate methodologies were utilized for heliostat placement. The first algorithm, deemed the Radially Staggered Heliostat Field Layout (RSHFL) algorithm, implements a radially staggered configuration in an effort to minimize optical losses of the NCSETF. Minimizing optical losses results in a more efficient system. From an economic perspective, fewer heliostats are required to produce the targeted output, implying less capital expenditure in construction of the heliostat field.

The second approach was to utilize a tightly packed North-South (N-S) cornfield configuration in an effort to pack as many heliostats as possible into the utilizable region of the TR for the primary AP of the heliostat filed. The utilizable region is depicted by the trapezoid presented in Figure 3.5. The N-S Cornfield Heliostat Field Layout (NSCHFL) algorithm ensures that a heliostat will not block a parallel vertical heliostat on a subsequent row if the heliostats, TR, and sun source are all co-linear. The NSCHFL algorithm was developed with the realization that the optical efficiency of the system would greatly decrease due to the effects of blocking and shading. Further details as to how each algorithm was developed are presented.

3.7.2 Radially Staggered Heliostat Field Layout (RSHFL) Algorithm

A radially staggered no blocking algorithm similar to that utilized in the MUEEN code presented by Siala [34] was implemented. The configuration can be described by rings of heliostats surrounding the tower, with no heliostat lying directly in front of another heliostat on an adjacent ring. Such a configuration allows for rays to pass in between heliostats located on neighboring rings. The RSHFL algorithm does not consider the effects of shading. However, as described by Siala [34], blocking has a more pronounced effect on the layout of heliostat fields than shading. Figure 3.13 demonstrates a radially staggered heliostat configuration where each heliostat can be defined in 2D space by radial and azimuth spacing.

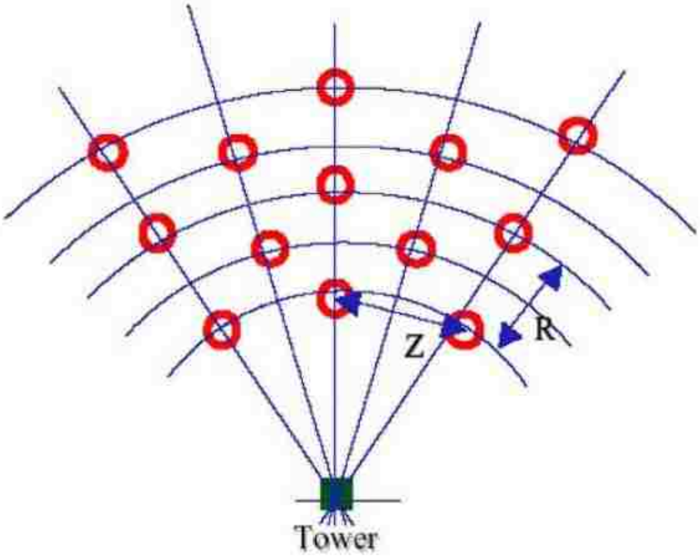

Figure 3.13 Radially staggered configuration [35]

A mathematical description of the algorithm implemented in the MUEEN code is presented by Siala et al. [34]. The RSHFL algorithm executed in modeling the radially staggered field of the NCSETF is very similar, but does contain some modifications. Primarily, the algorithm utilized to develop the MUEEN was designed to be implemented in a C++ programming environment [34]. Due to indexing discrepancies between C++ and MATLAB®, the MUEEN code algorithm had to be re-written for suitable implementation in MATLAB®. Furthermore, the MUEEN code algorithm is designed for a tower receiver system, not a TR system like that of the NCSETF. Different radii are suggested for the first ring of heliostats in a TR system. Falcone [36] suggests the first ring be located at a distance three quarters the height of the AP. The MUEEN code algorithm suggests the first ring of heliostats be located at a radius the height of the AP [34]. In order to accommodate the compact optical geometry desired for the NCSETF, the first ring of heliostats was allocated to be one third the height of the AP in the RSHFL algorithm.

The RSHFL algorithm implemented in MATLAB® requires user input parameters for the maximum angular direction of the heliostat field, the maximum ring radius, the length and width of each heliostat, and the number of facets along the length and width. As an output, the RSHFL algorithm produces the x, y, and z location for the center of each heliostat in a 3D Cartesian coordinate system. For purposes of modeling the NCSETF, the maximum angular direction was set to 30° and the maximum heliostat ring radius was specified at 150 m. The parameters were quantified in order to lay down a radially staggered no blocking heliostat field large enough to cover the entire utilizable area of the down beam reflector. As specified, the heliostat length and widths were set to 8 m, with 8 facets along each to achieve the 1 m^2 mirror tiles. Figure 3.14 displays the input prompt for the RSHFL algorithm, and the subsequent field layout as well as down beam reflector for modeling the NCSETF.

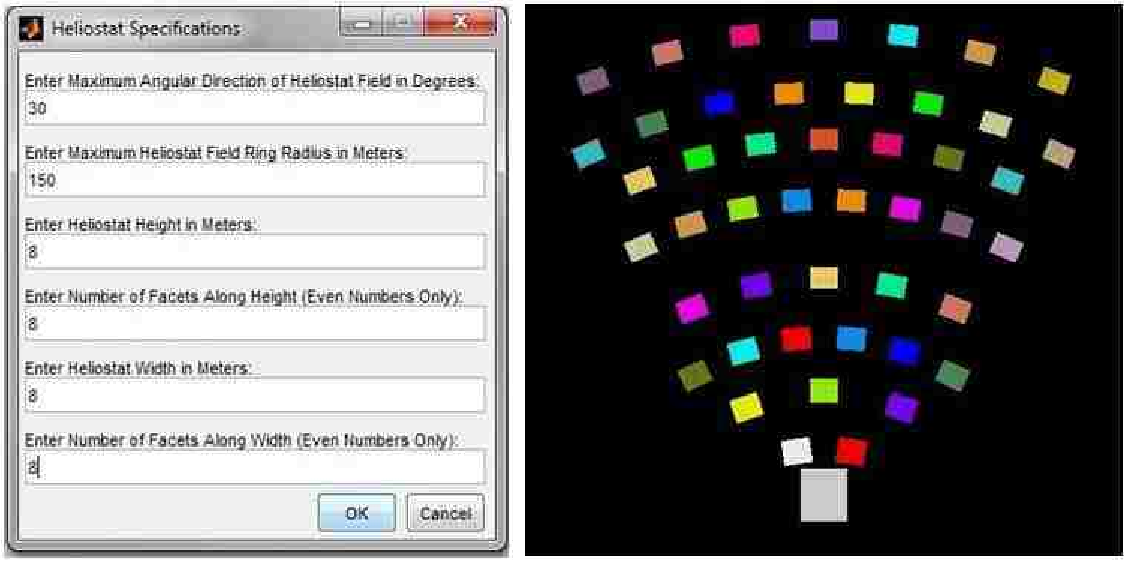

Enter Maximum Angular Direction of Heliostat Field in Degrees: 30

Enter Maximum Heliostat Field Ring Radius in Meters: 150

Enter Heliostat Height in Meters: 8

Enter Number of Facets Along Height (Even Numbers Only): 8

Enter Heliostat Width in Meters: 8

Enter Number of Facets Along Width (Even Numbers Only): 2

Figure 3.14 RSHFL algorithm prompt and heliostat field layout

3.7.3 N-S Cornfield Heliostat Field Layout (NSCHFL) Algorithm

The NSCHFL algorithm ensures that a heliostat will not block a parallel vertical heliostat on a subsequent row if the heliostats, TR, and sun source are all co-linear. For any given row, heliostats are compacted side by side, as close as physically possible without obstructing the range of motion of an adjacent heliostat. The NSCHFL algorithm takes in as user defined input parameters the minimum first row distance, the maximum last row distance, the length and width of each heliostat, and the number of facets along the length and width.

In order to allocate the row spacing for the field, the lowest position of the sun in the sky at solar noon for Las Vegas over the course of the year is required. The elevation, or solar altitude angle, α_s, is defined by the angle between the horizontal and a line to the sun. The elevation angle is a complement of the solar zenith angle, and therefore can be calculated according to the equation (3.21):

$$\alpha_s = 90 - \theta_z \tag{3.21}$$

At solar noon, in the Northern Hemisphere the elevation angle can be represented by the simplified equation (3.22):

$$\alpha_s = 90 - \phi + \delta \tag{3.22}$$

As previously described, the declination angle ranges from 23.45° on the summer solstice, June 21, to -23.45° on the winter solstice, December 22. Applying equation (3.22) for Las Vegas on the winter solstice when the sun is at its lowest elevation yields the following minimum elevation angle, α_{sm}, at solar noon (3.23):

$$\alpha_{sm} = 90 - 36.083 - 23.45 = 30.467^\circ \tag{3.23}$$

With the minimum elevation angle at solar noon specified, the row spacing, R_{space}, is defined based on the length of the heliostat mirror, L_m, according to the following equation (3.24):

$$R_{space} = \frac{L_m}{\tan(\alpha_{sm})} \tag{3.24}$$

Applying equation (3.24) for the conditions of modeling the NCSETF with 8 x 8 m heliostats and the minimum elevation angle as specified by equation (3.23) yields the following row spacing implemented for the N-S algorithm (3.25):

$$R_{space} = \frac{8}{\tan(30.467)} = 13.599\, m \tag{3.25}$$

With the row spacing allocated, the NSCHFL algorithm starts at the location of the first row and places subsequent rows, as defined by R_{space}, up to the distance of the maximum row. The width of each row is initially defined by laying down a square grid of heliostats, as determined by the minimum and maximum row. In investigations of the NCSETF the first row of heliostats was specified at 16 m from the focal point and the furthest possible row at 150 m. Again, this was to cover the entire utilizable range of the down beam reflector. The resulting field, for 8 x 8 m heliostats with 1 m^2 mirror tiles is depicted in Figure 3.15, along with the input prompt to the NSCHFL algorithm.

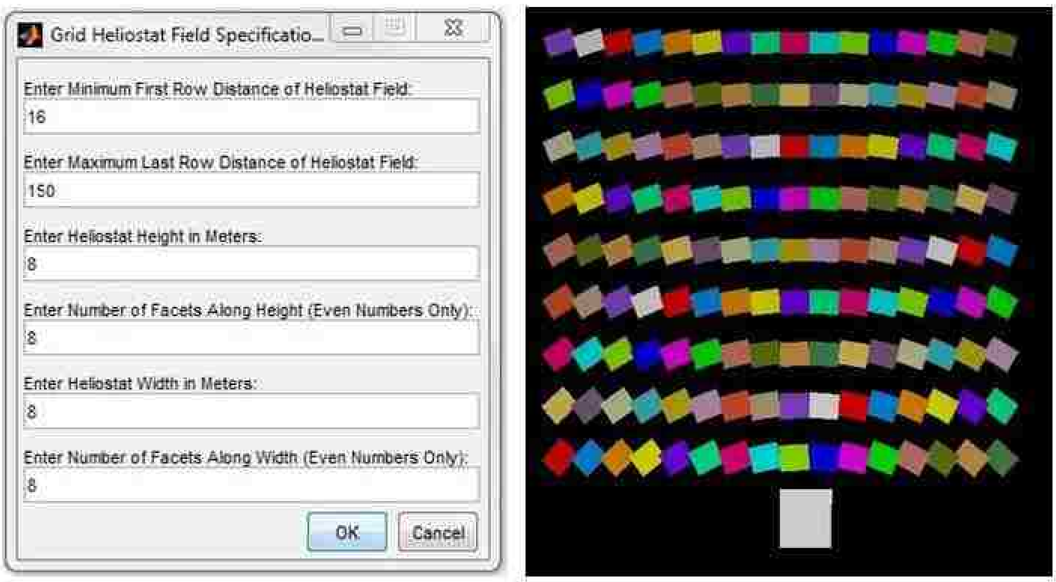

Enter Minimum First Row Distance of Heliostat Field:
16

Enter Maximum Last Row Distance of Heliostat Field:
150

Enter Heliostat Height in Meters:
8

Enter Number of Facets Along Height (Even Numbers Only):
8

Enter Heliostat Width in Meters:
8

Enter Number of Facets Along Width (Even Numbers Only):
8

Figure 3.15 NSCHFL algorithm prompt and heliostat field layout

A square grid of heliostats, as presented in Figure 3.15, contains several heliostats outside of the utilizable range of the down beam reflector. In order to further refine the N-S heliostat field, non-contributing heliostats are eliminated. ASAP® allows for any object within the optical geometry to be neglected from a ray trace. Three methods were implemented to determine contributing heliostats. First, heliostats visibly noticeable outside of the working trapezoid of the TR for the primary AP of the heliostat field were manually ignored. The field was further refined using the statistical data and the visualization of the ray trace. The ASAP® model of the NCSETF produces statistical data of how many rays hit any given heliostat and don't reflect to the down beam mirror. Utilizing this statistical data, along with visualization of the ray trace, non-contributing heliostats were further eliminated based on their contributing factor. For the conditions of modeling the NCSETF, the refined grid and subsequent ray trace of the NSCHFL algorithm are presented in Figure 3.16.

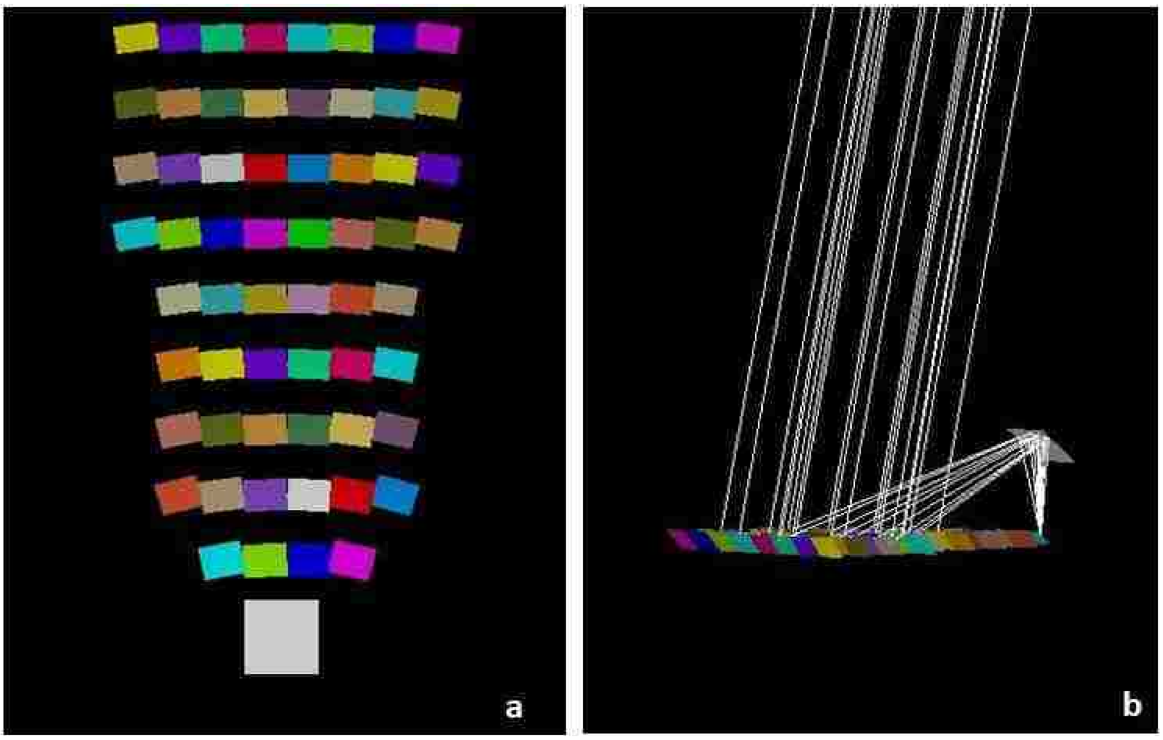

Figure 3.16 Refined N-S cornfield (a) heliostat field layout; (b) ray trace

3.8 Algorithm Integration

For any given simulation the user is prompted to specify three parameters to allocate the time of simulation within the model; the month, day, and simulation hour, S_h. Utilizing the NSCHFL algorithm the user is also prompted to specify the minimum row distance for placing heliostats from the TR center, R_{min}, the maximum row distance for placing heliostats from the TR center, R_{max}, the width of the heliostat mirror, W_m, the length of the heliostat mirror, L_m, along with the number of facets along the length and width of each heliostats. Based on the specified time parameters, the SPO algorithm selects the appropriate DNI from the TMY weather data file and exports a data file to the root directory of ASAP® containing the solar zenith angle, solar azimuth angle, and DNI required to simulate the sun source for the chosen hour within the ray trace. Furthermore, the SPO algorithm exports to the HROPV algorithm the hourly solar zenith and azimuth angles so that the orientation of each heliostat can be determined based on the relative position of the sun source within the model.

The user established heliostat field input parameters are utilized by the NSCHFL algorithm to determine the number of heliostats within the utilizable range of the TR for the primary AP of the field, N_{helios}, along with the global coordinates of each heliostats. Those parameters are then exported to both ASAP® so that each heliostat can be appropriately realized within the ray trace, as well as to the HROPV algorithm so that proper orientation of each heliostat can be determined. The HROPV algorithm exports to ASAP® the relative rotation about an arbitrarily defined set of axes located at the center of each heliostat the rotation for each heliostat to achieve the heliostat surface azimuth angle for the specified SH, R_{ha}, the heliostat surface zenith angle for the specified SH, R_{hz}, and the vertex radius of curvature, V_{radC}, required to achieve appropriate convergence behavior for each heliostat. ASAP® is then able to simulate the optical geometry of the system and produce an output at the detector both in terms of power and power distribution. Figure 3.17 is a flow chart depiction of how the algorithms are coupled together along with ASAP® to simulate the optical performance of the facility for any given SH.

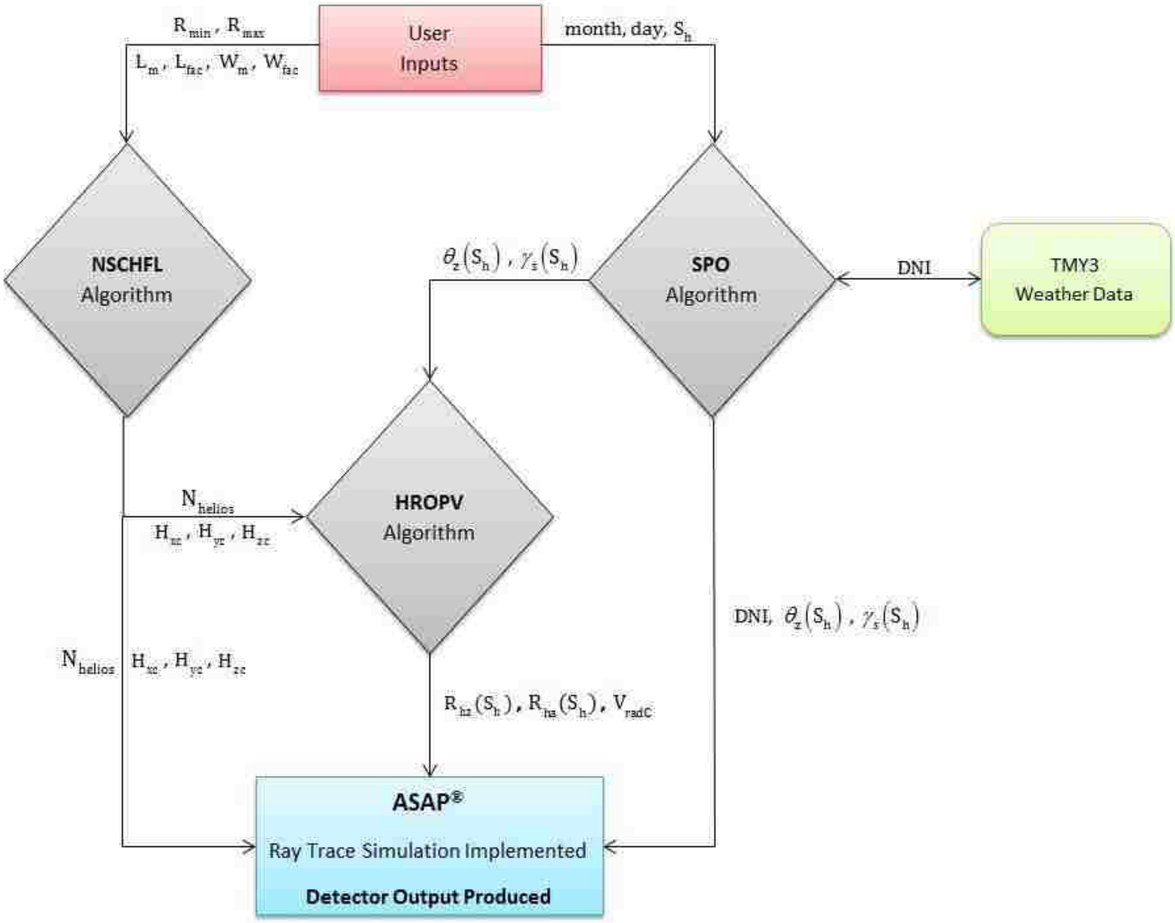

Figure 3.17 Algorithm flow chart for simulating NCSETF

CHAPTER 4

SIMULATION RESULTS & DISCUSSION

4.1 DNI Model Validation

In order to confirm proper DNI is received at ground level within the ASAP® simulation of the NCSETF, a simulation utilizing gauging surfaces was first implemented. Five flat surfaces were placed at ground level and orientated normal to the sun's rays within the model. The objective was to establish relatively equal and accurate distribution of flux amongst the heliostat field within the ray trace. Each of the five gauging surfaces measures 16 m^2, one quarter the total surface area of an actual heliostat implemented within the NCSETF model. The motivation behind utilizing smaller gauging surfaces was to ensure an appropriate amount of rays were simulated within the model.

For each gauging object, statistical data containing the number of rays landing on each surface, as well as the total flux (J/s) was produced. Additionally, irradiance (W/m^2) maps for each gauging surface were developed. Initial gauging was implemented using TMY3 data for January 21, 2001 at 12:00 p.m., in which DNI equates to 839 W/m^2. Table 4.1 demonstrates the statistical data produced by the gauging simulation for the five surfaces:

Table 4.1 Statistical data of DNI gauging simulation

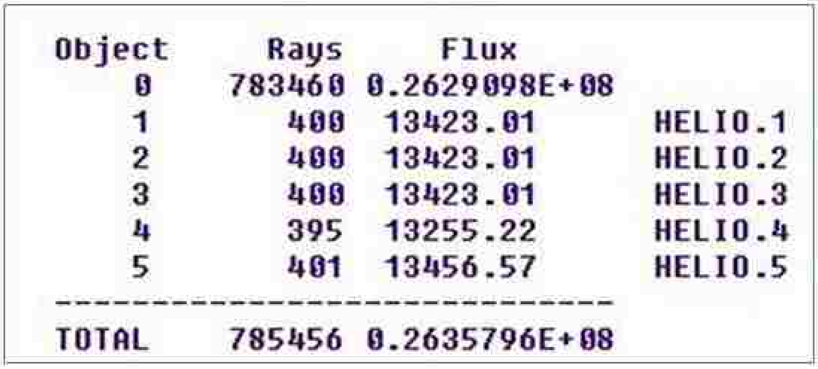

```
Object     Rays     Flux
     0   783460 0.2629098E+08
     1      400  13423.01       HELIO.1
     2      400  13423.01       HELIO.2
     3      400  13423.01       HELIO.3
     4      395  13255.22       HELIO.4
     5      401  13456.57       HELIO.5
----------------------------
TOTAL    785456 0.2635796E+08
```

The statistical data demonstrates that approximately 400 rays are equally incident on each gauging surface. Furthermore, taking the flux received on each gauging surface, roughly 13,420 J/s, and dividing by the surface area of each object, 16 m^2, yields DNI at approximately 839 W/m^2. With appropriate DNI established, 2D and 3D flux maps were also implemented to demonstrate distribution. Figure 4.1 depicts a 2D contour and 3D irradiance plot for the gauging surfaces of the model:

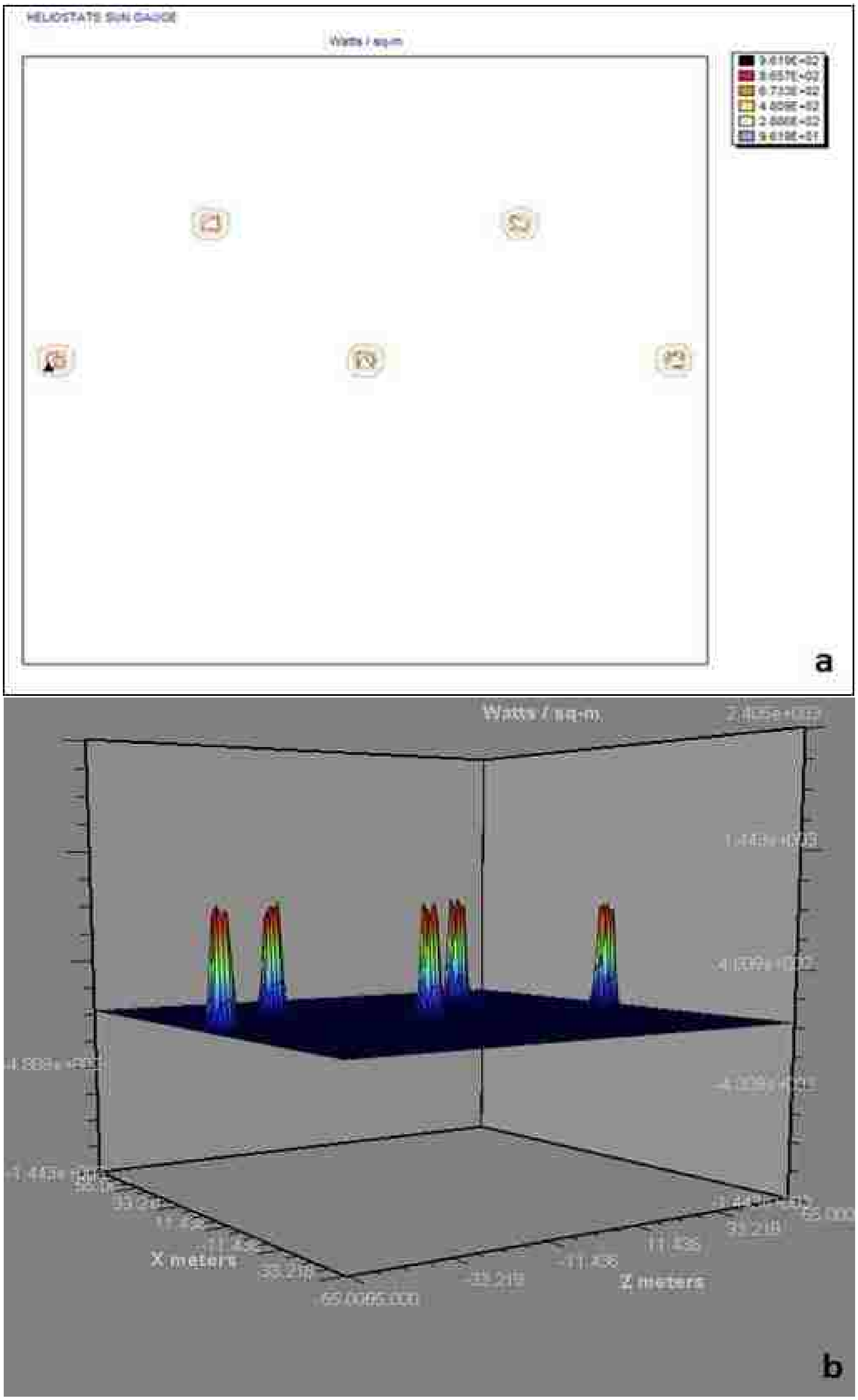

Figure 4.1 (a) 2D DNI gauging contour plot; (b) 3D DNI gauging irradiance plot

The DNI gauging simulation exhibits appropriate allocation of DNI emitting from the sun source within the ASAP® model of the NCSETF. With the sun source validated, attention was turned towards simulation of the NCSETF and the previously described heliostat field layout methodologies.

4.2 Simulation DNI Data

It was originally intended that simulations would be performed for the two solstices of the year, as well as the two equinoxes of the year, in order to produce a simulated performance of the facility for each of the four seasons. TMY3 data, however, for the summer solstice June 21, 1988 is abnormally low for summer conditions in Las Vegas. For example, at solar noon TMY3 DNI yields 316 W/m^2. Typical summer DNI values commonly exceed 900 W/m^2 in Las Vegas. The low TMY3 DNI for the summer solstice is likely due to overcast conditions for that specific day. As a result, an alternate date more representative of summer conditions in which high DNI values are attained was chosen. The replacement date was selected to be July 12, TMY 1991 in which DNI reaches 930 W/m^2 at solar noon. The winter solstice, as well as the spring and fall equinoxes, were still chosen for initial investigations of the NCSETF. Hours of simulation were from 5:00 a.m. through 7:00 p.m., ensuring modeled results for every hour of sunlight for each of the evaluated days. Table 4.2 demonstrates DNI vs. hour for each day simulated.

Table 4.2 TMY3 hourly DNI (W/m^2) for simulation days of NCSETF

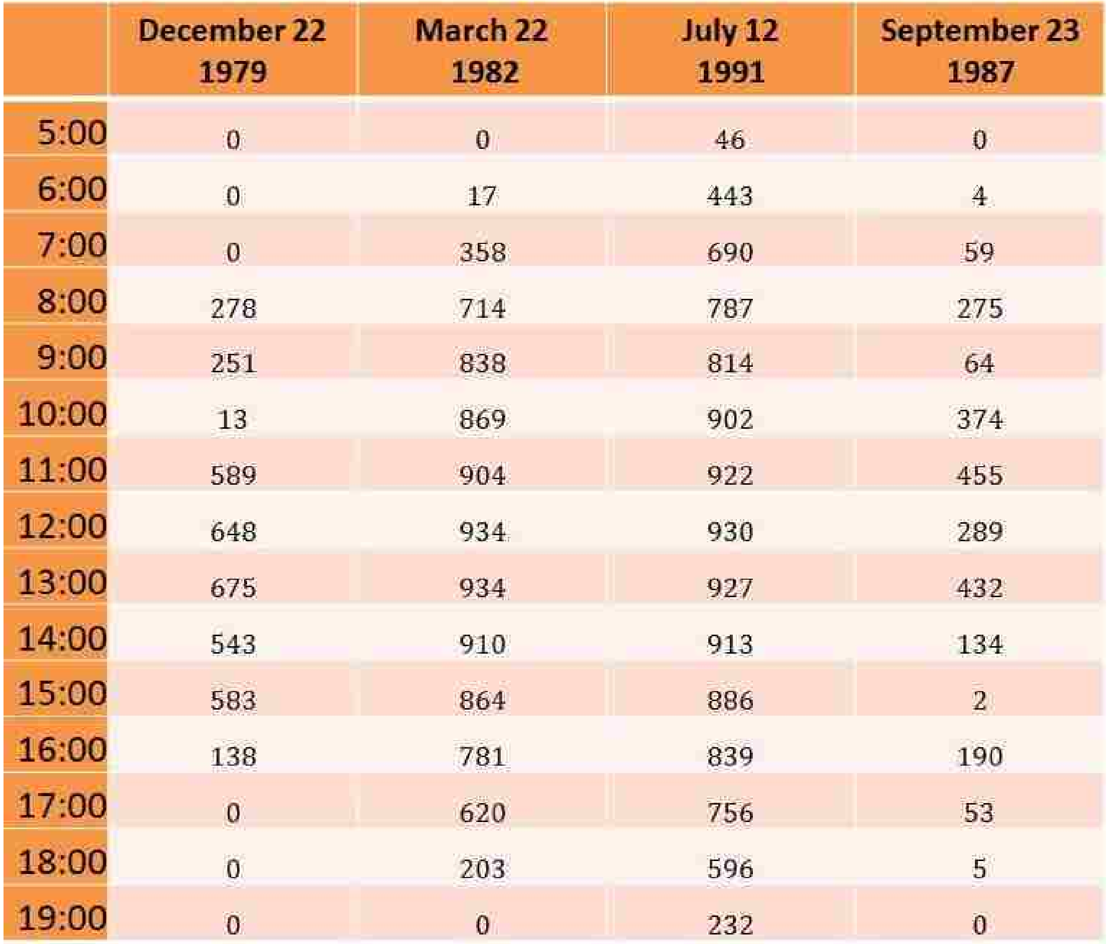

	December 22 1979	March 22 1982	July 12 1991	September 23 1987
5:00	0	0	46	0
6:00	0	17	443	4
7:00	0	358	690	59
8:00	278	714	787	275
9:00	251	838	814	64
10:00	13	869	902	374
11:00	589	904	922	455
12:00	648	934	930	289
13:00	675	934	927	432
14:00	543	910	913	134
15:00	583	864	886	2
16:00	138	781	839	190
17:00	0	620	756	53
18:00	0	203	596	5
19:00	0	0	232	0

The DNI data was also plotted as a function of time for each simulation day in order to provide a visual representation of the trends in the data. The resulting plot is presented in Figure 4.2:

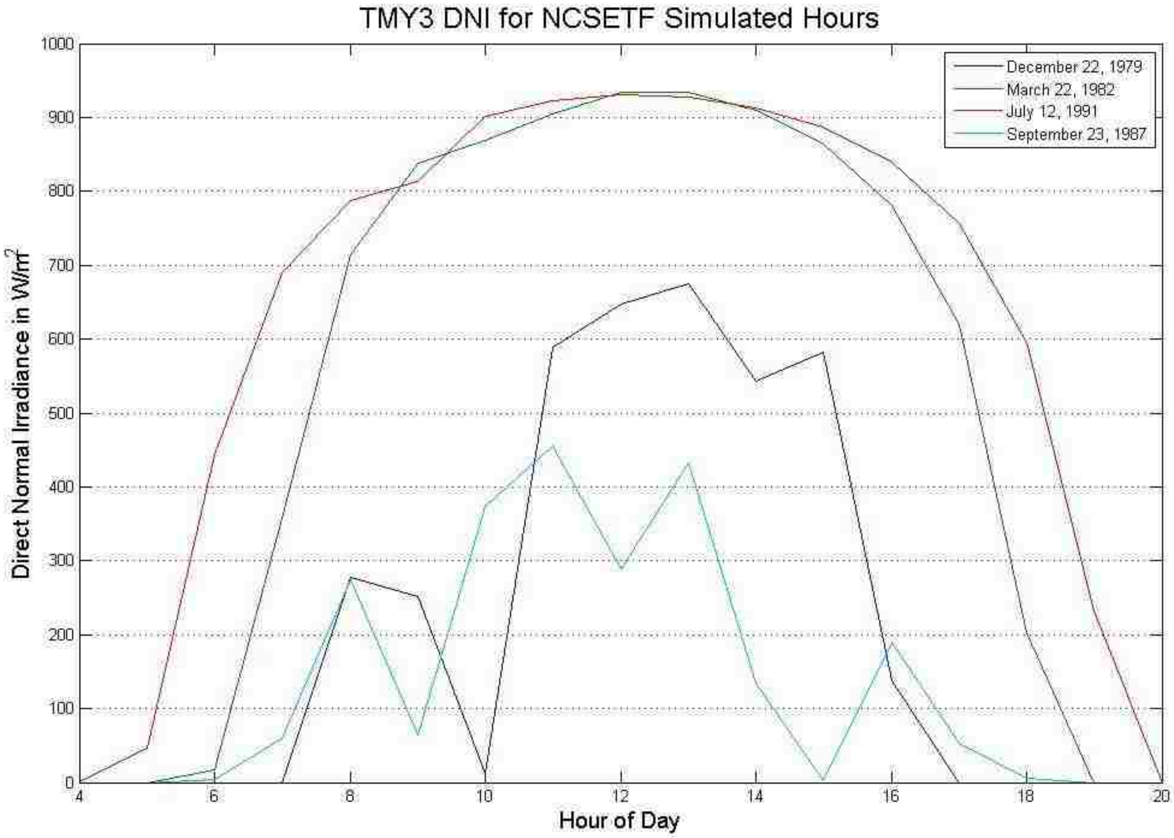

Figure 4.2 TMY3 DNI for NCSETF simulation hours

Comparing the output of the NCSETF against the DNI values depicted in Figure 4.2 allows for trends in the performance of the facility to be realized. Both the effects of optical losses as well as varying DNI intensities can be observed in the output of the facility. The performance of the facility is presented for the same hours as depicted in Table 4.2 and Figure 4.2.

4.3 Radially Staggered Simulations with Parallel Rays

The radially staggered algorithm was first implemented for solar noon on July 12, 1991. The results of that simulation are presented. Figure 4.3 is representative of the ray trace for the radially staggered heliostat configuration of the NCSETF.

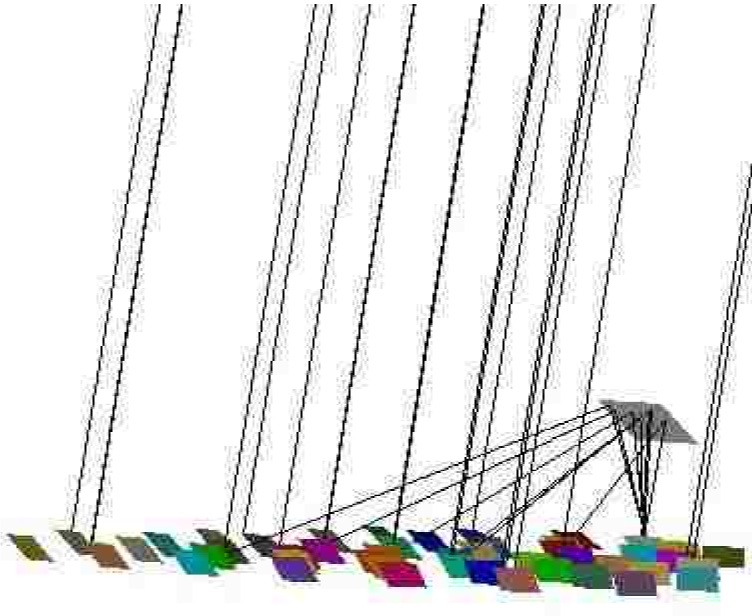

Figure 4.3 NCSETF ray trace utilizing radially staggered heliostat field layout

The ray trace demonstrates utilizable heliostats. Heliostats that are not within the acceptance realm of the down beam reflector display a ray incident on the heliostat, but that ray does not continue along its reflected path towards the AP. Figure 4.4 depicts 2D and 3D irradiance plots for the detector at ground level. An averaging of pixels is utilized within the model in order to smooth the image of the data.

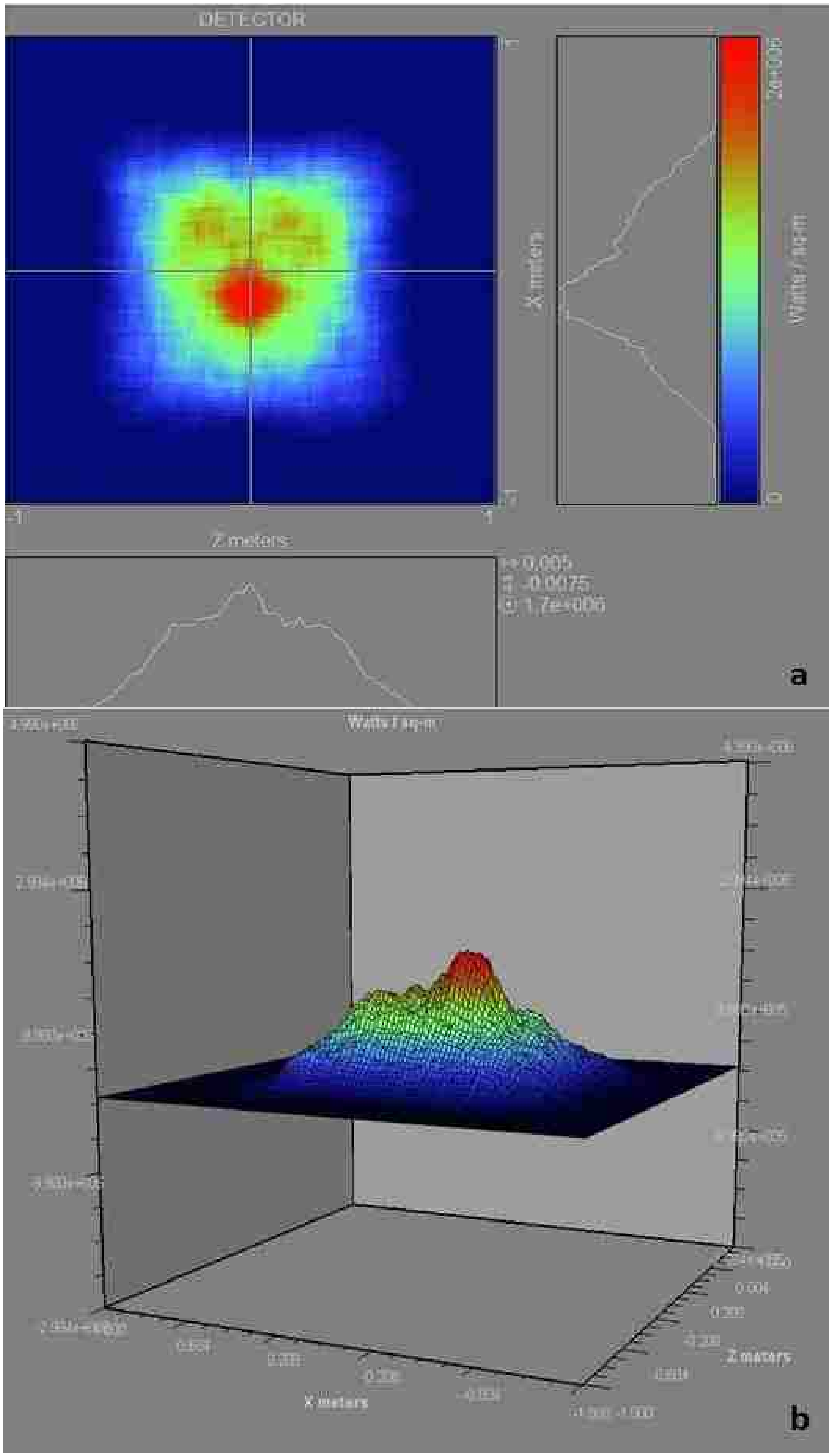

Figure 4.4 (a) 2D collector irradiance plot; (b) 3D collector irradiance plot

Figure 4.4 depicts a concentrated spot size totaling an approximated area of 2 m^2. At the origin of the detector, located at the center of the crosshairs in Figure 4.4 (a), the irradiance totals 1.7 x 10^6 W/m^2. Dividing by DNI for the hour, 930 W/m^2, yields a total concentration of approximately 1,828 suns. As can be observed, local hotspots exist within the concentrated image, and may not always be centered directly below the down beam reflector. A contour plot and 3D isometric distribution of flux plot were also produced for the detector at ground level. Figure 4.5 presents those plots:

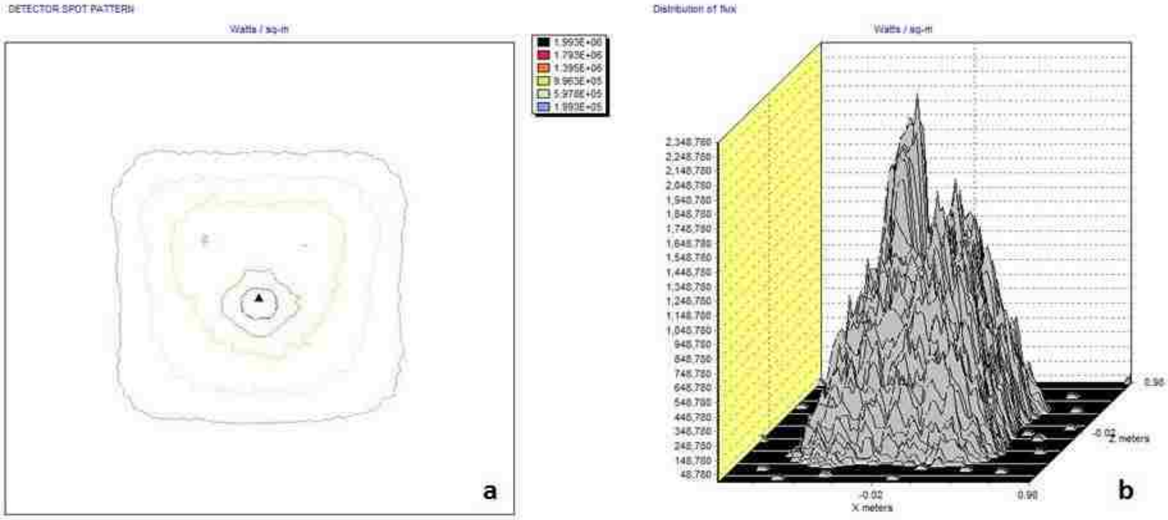

Figure 4.5 (a) Detector contour plot; (b) Isometric distribution of flux plot

The contour plot displays concentric rings ranging from 1.993 x 10^5 W/m^2 to a peak of 1.993 x 10^6 W/m^2. This produces a variance in concentration amongst the image from 214 suns to 2,143 suns. Along with the plots, the statistical data of the ray trace produces a simulated 1,000,014 W received on a 4 m^2 detector at ground level.

The resulting conclusions that can be drawn from the model are significant. Primarily, the RSHFL algorithm is not ideal for heliostat placement of the NCSETF. The reason being, the targeted 2,000 m^2 of reflective heliostat surface area does not fit within the utilizable range of the down beam reflector. As a result, the targeted output of 1 MW is barely achieved for even an hour of high DNI during the summer. Under such a configuration the simulation demonstrates that the NCSETF would only meet the desired output for a few select hours of the year. As a result, the idea of using the radially staggered field layout was abandoned, and instead focus was turned to the much more compact N-S cornfield configuration.

4.4 N-S Cornfield Simulations with Parallel Rays

4.4.1 Presentation Overview

For each day simulated the outputs of the model for the NCSETF are presented in detail for the hours of 9:00 a.m., 12:00 p.m., and 4:00 p.m. with a solar disk emitting parallel rays. General trends are then demonstrated for the output of the facility over the course of the four days modeled. Power output and concentration trends are established along with the optical efficiency of the facility for the days simulated.

4.4.2 TMY3 July 12, 1991 Simulation

The N-S cornfield heliostat field layout was first simulated for the same hour as the radially staggered configuration, July 12, 1991 at solar noon. The 3D visualization of that ray trace is realized in Figure 4.6.

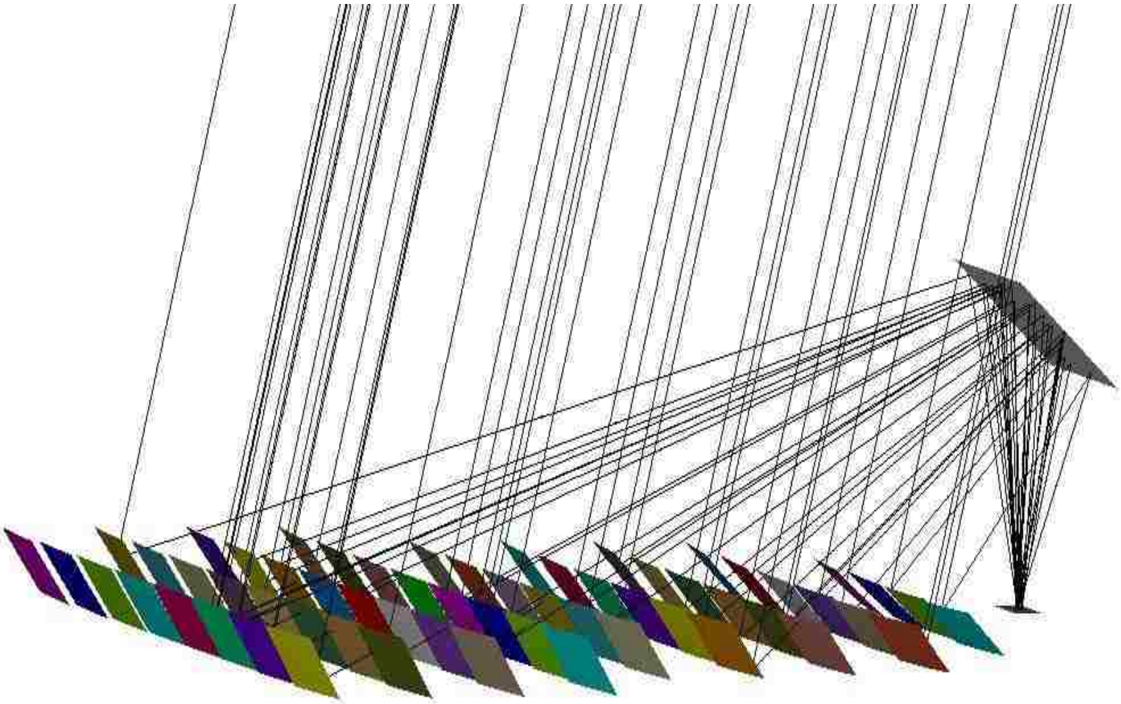

Figure 4.6 NCSETF ray trace utilizing N-S cornfield with parallel rays

The detector spot pattern and contour plot at solar noon for the N-S cornfield configuration are presented in Figure 4.7. Figure 4.7 is followed by similar plots for the hours of 9:00 a.m. and 4:00 p.m. in Figures 4.8 and 4.9, respectively. Figure 4.7 demonstrates a spot size centered just south of the origin, ranging in concentration from 521 suns to a maximum of 5,210 suns. Furthermore, a total of 1,890,651 W are accumulated on the detector at ground level. Figure 4.8 presents a concentration ranging from 159 suns to 1,588 suns for the hour ending at the timestamp of 9:00 a.m. The rays are congregated to the west side of the detector. A total of 1,356,987 W are collected on the receiver. For the hour of 4:00 p.m. concentration ranges from 90 suns to 904 suns as presented in Figure 4.9. A total of 1,064,075 W are simulated to be received on the detector.

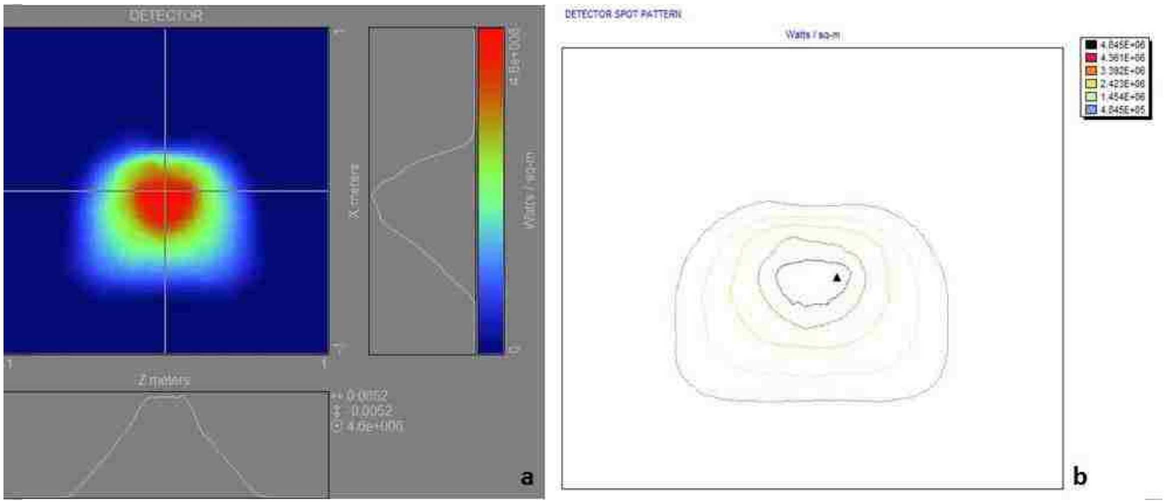

Figure 4.7 NCSETF July 12, 12:00 p.m. (a) Detector insolation plot; (b) Detector contour plot

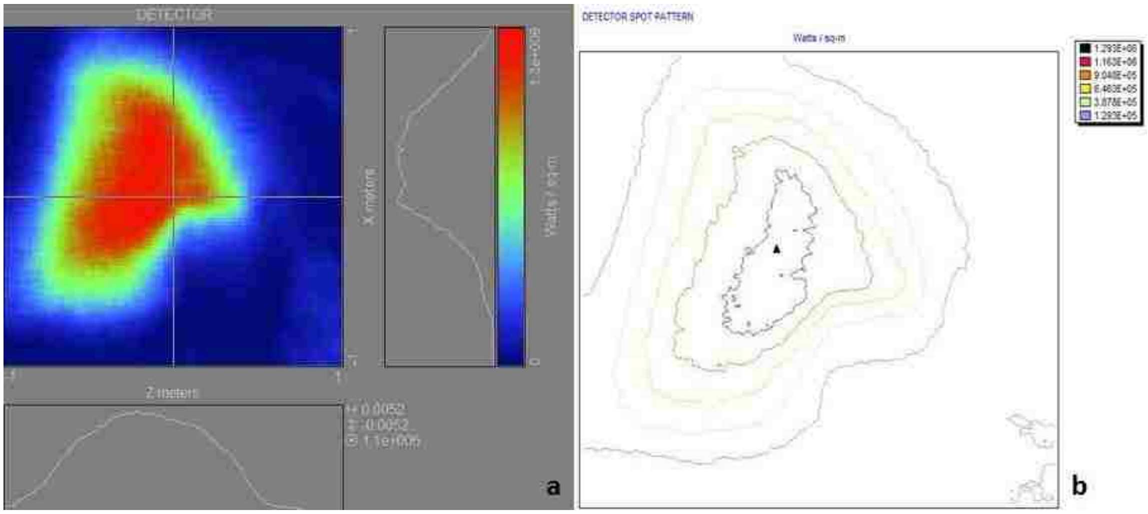

Figure 4.8 NCSETF July 12, 9:00 a.m. (a) Detector insolation plot; (b) Detector contour plot

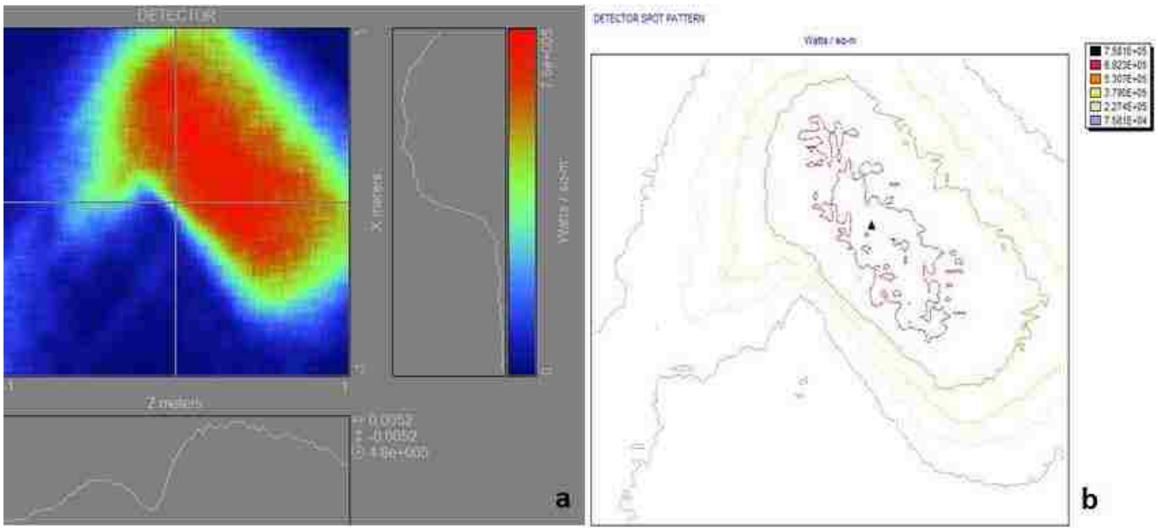

Figure 4.9 NCSETF July 12, 4:00 p.m. (a) Detector insolation plot; (b) Detector contour plot

The behavior of the spot patterns depicted in Figures 4.7, 4.8, and 4.9 lead to several observations. The local hot spots and shape of the concentrated rays vary over the course of the day. At 9:00 a.m., the majority of the rays tend to be concentrated toward the west side of the detector. Conversely, at 4:00 p.m. rays tend to be bundled on the east side of the detector. At local noon, the rays are relatively focused from east to west, but weighed slightly heavier towards the south side of the collector.

The effects of the behavior are similar to as expected. Because the heliostats are essentially defined as a smooth parabolic dish, the more off-focus they are from the AP the larger the optical aberrations become. Since heliostats are orientated to split the angular difference between the sun position vector and the target position vector in the plane of reflection, optical aberrations and cosine losses grow as the angular direction from the sun to the target increases.

4.4.3 TMY3 September 23, 1987 Simulation

The simulated outputs for the fall equinox, September 23, 1987 are presented for the hours 9:00 a.m., 12:00 p.m., and 4:00 p.m. Figure 4.10 demonstrates a spot size centered north of the origin at 9:00 a.m., ranging in concentration from 469 suns to a maximum of 4,693 suns. Additionally, a total of 110,428 W are accumulated on the detector at ground level for the hour of 9:00 a.m. Figure 4.11 presents a concentration ranging from 1,069 suns to 10,685 suns for the hour ending at the timestamp of 12:00 p.m. The rays are centered just south of the origin on the detector. A total of 561,490 W are collected on the receiver. For the hour of 4:00 p.m. concentration ranges from 200 suns to 2,000 suns as presented in Figure 4.12. A total of 271,973 W are simulated to be received on the detector.

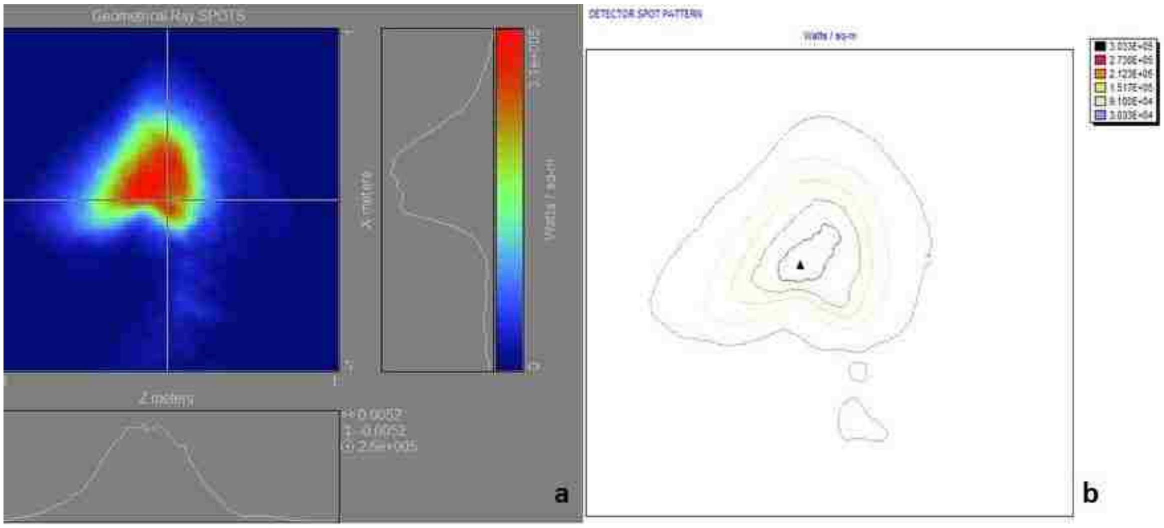

Figure 4.10 NCSETF Sept 23, 9:00 a.m. (a) Detector insolation plot; (b) Detector contour plot

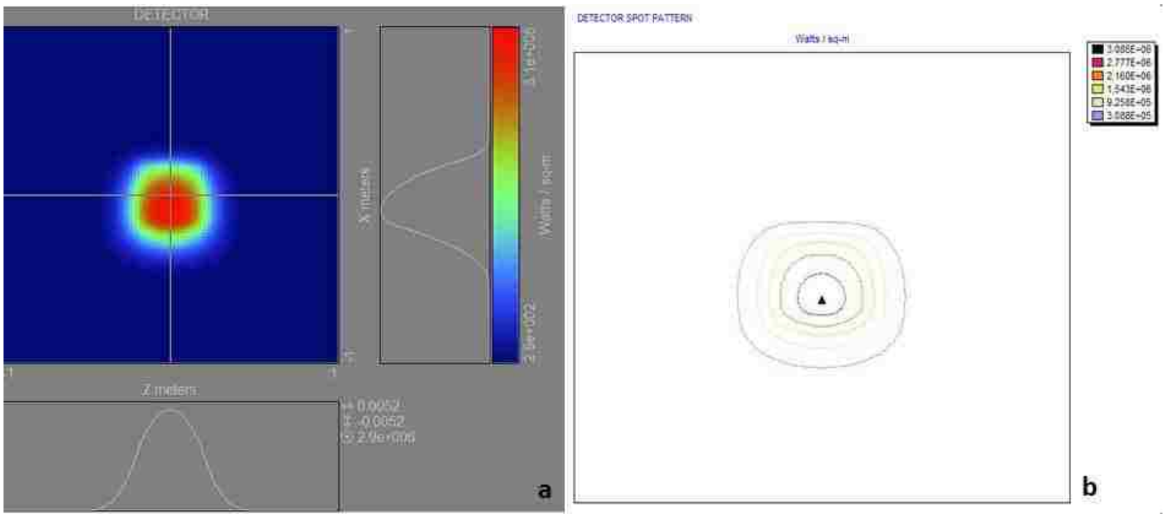

Figure 4.11 NCSETF Sept 23, 12:00 p.m. (a) Detector insolation plot; (b) Detector contour plot

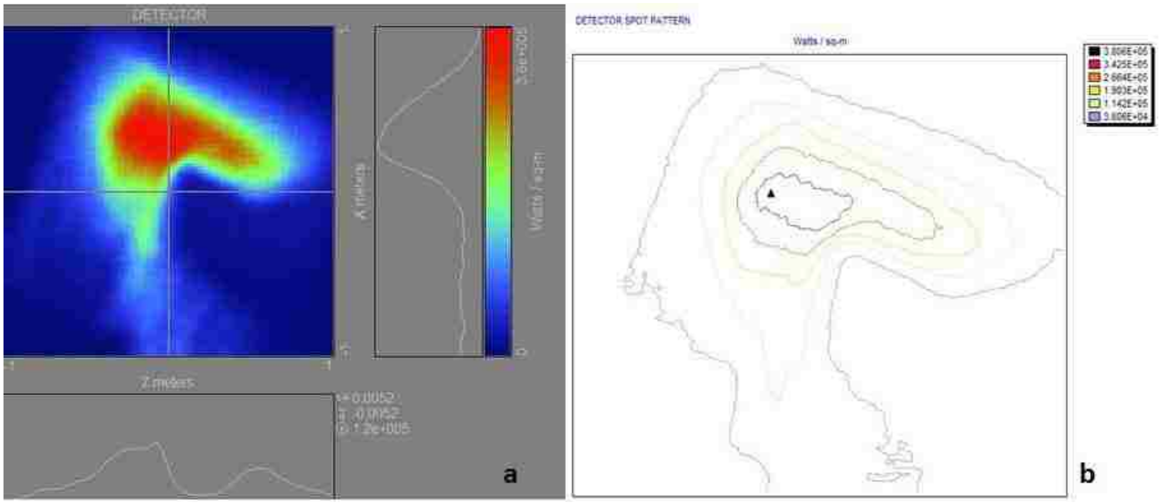

Figure 4.12 NCSETF Sept 23, 4:00 p.m. (a) Detector insolation plot; (b) Detector contour plot

When comparing the simulations for September 23, 1987 to those of July 12, 1991 the results appear plausible. Tighter concentration ratios and spot sizes are achieved. Again, because the sun is lower in the sky for the September simulation, the angular difference in the plane of reflection is less. The result is less optical aberrations due to off-focus conditions of the dish shaped heliostats. The same trend is observed for off-noon hours, the farther from solar noon the larger the spot size and less concentration levels are achieved.

4.4.4 TMY3 December 22, 1979

The simulation results for December 22, 1979 during the hours of 9:00 a.m., 12:00 p.m., and 4:00 p.m. are presented respectively. Figure 4.13 demonstrates a tight spot size centered north of the origin at 9:00 a.m., ranging in concentration from 971 suns to a maximum of 9,713 suns. A total of 257,375 W are gathered on the detector at ground level within the simulation. Figure 4.14 presents a concentration ranging from 14,086 suns to 140,864 suns for the hour ending at the timestamp of 12:00 p.m. The rays are highly concentrated to a tight spot centered directly at the origin of the detector. A total of 954,297 W are collected on the receiver. For the hour of 4:00 p.m. concentration ranges from 34 suns to 337 suns as presented in Figure 4.15. A total of 27,262 W are simulated to be received on the detector.

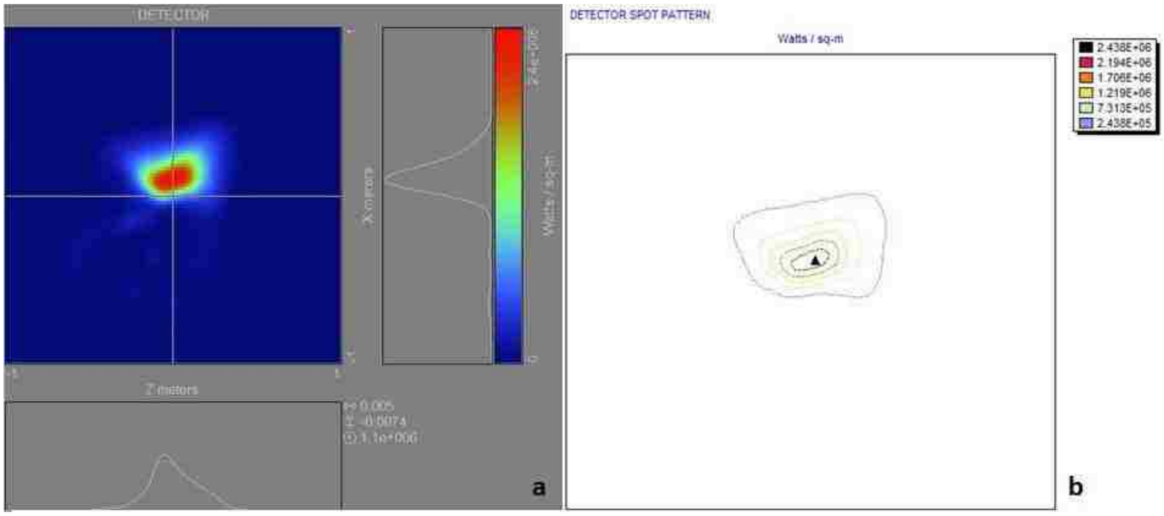

Figure 4.13 NCSETF Dec 22, 9:00 a.m. (a) Detector insolation plot; (b) Detector contour plot

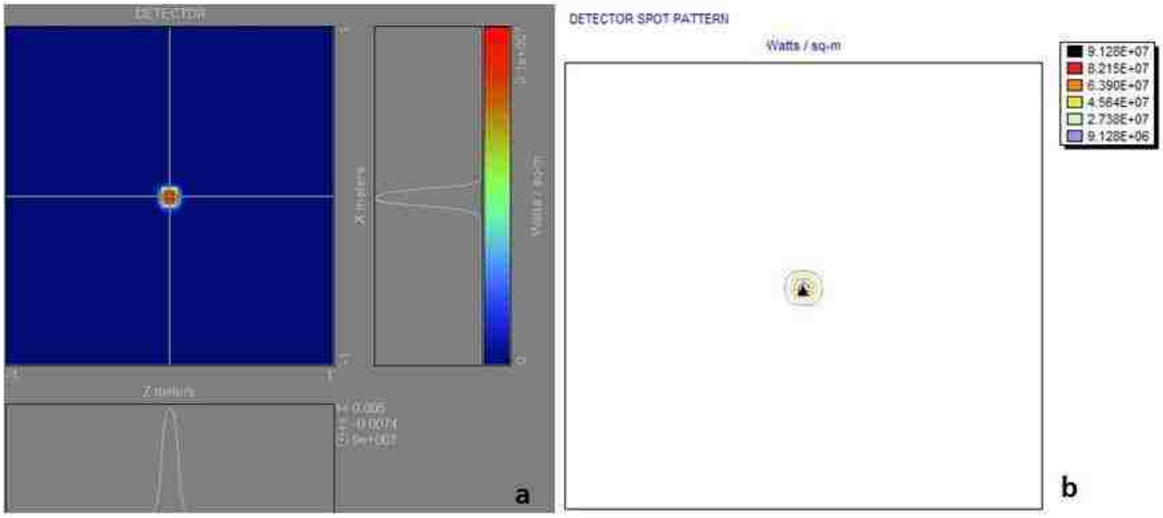

Figure 4.14 NCSETF Dec 22, 12:00 p.m. (a) Detector insolation plot; (b) Detector contour plot

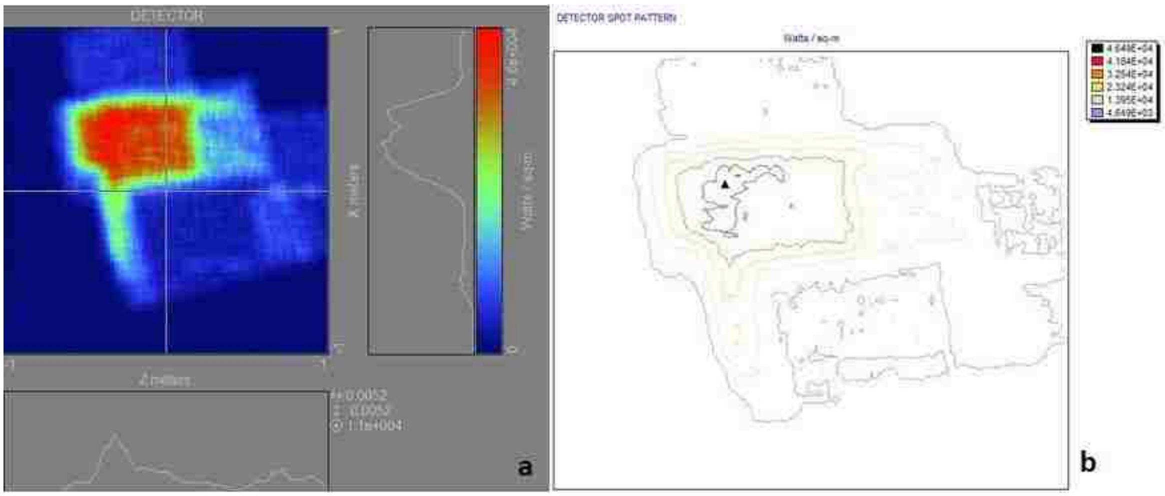

Figure 4.15 NCSETF Dec 22, 4:00 p.m. (a) Detector insolation plot; (b) Detector contour plot

The results for the December 22, 1979 simulation are insightful. In December the sun is relatively low in the sky. On solar noon, the elevation of the sun for the winter solstice in Las Vegas is just 30.467°. Resultantly, the angular difference between the sun position vector and the target position vector in the plane of reflection is small for each heliostat. Therefore, the object utilized to simulate a converging heliostat is nearly entirely in focus. The result is a very compact bundle of rays at the origin attaining extremely high concentration. In actuality, the achievable concentration is limited by the angular size of the sun in the sky, which is realized in section 4.5. The high concentration simulated is a product of utilizing parallel rays within the model to represent the sun. A higher level of concentration is simulated by the model due to the parallel ray representation of the sun.

4.4.5 TMY3 March 22, 1982

The simulation results for March 22, 1982 during the hours of 9:00 a.m., 12:00 p.m., and 4:00 p.m. are displayed. Figure 4.16 demonstrates a spot size centered north of the origin at 9:00 a.m., ranging in concentration from 470 suns to a maximum of 4,696 suns. Furthermore, a total of 1,445,371 W are accumulated on the detector at ground level. Figure 4.17 presents a concentration ranging from 1,067 suns to 10,665 suns for the hour ending at the timestamp of 12:00 p.m. The rays are centered just south of the origin on the detector. A total of 1,815,480 W are collected on the receiver. For the hour of 4:00 p.m. concentration ranges from 198 suns to 1,979 suns as presented in Figure 4.18. A total of 1,116,780 W are simulated to be received on the detector.

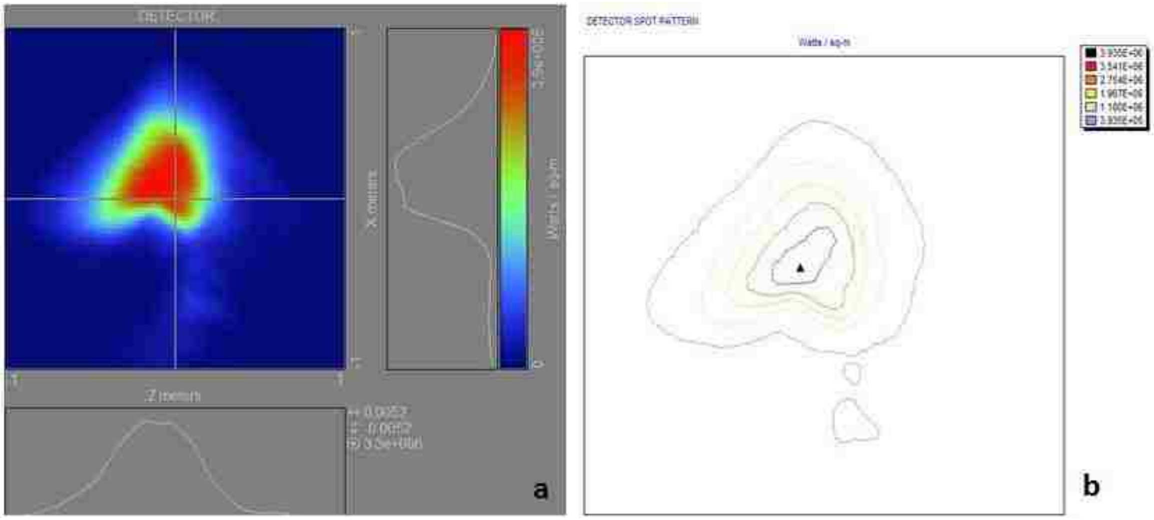

Figure 4.16 NCSETF March 22, 9:00 a.m. (a) Detector insolation plot; (b) Detector contour plot

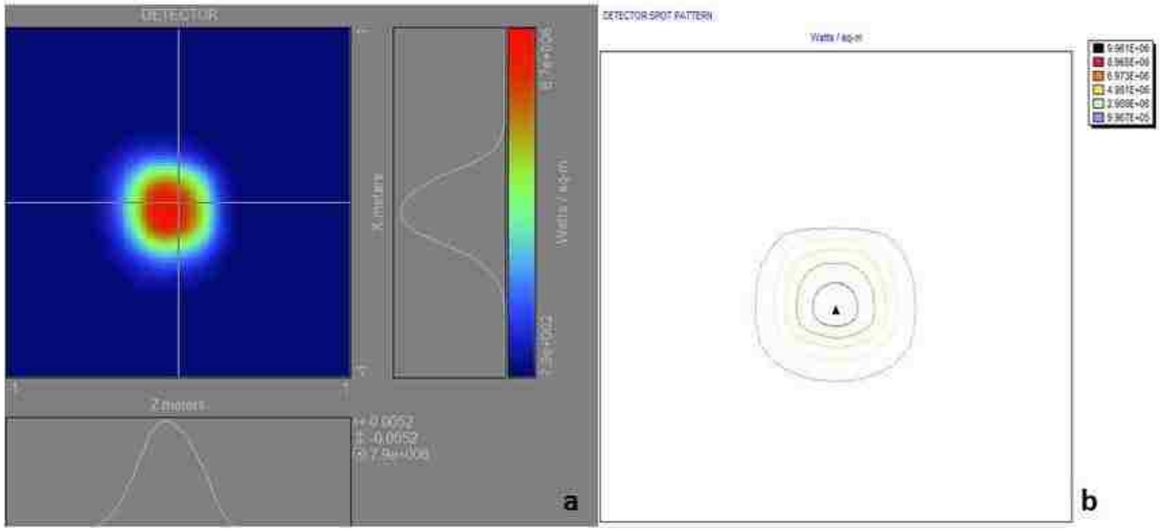

Figure 4.17 NCSETF March 22, 12:00 p.m. (a) Detector insolation plot; (b) Detector contour plot

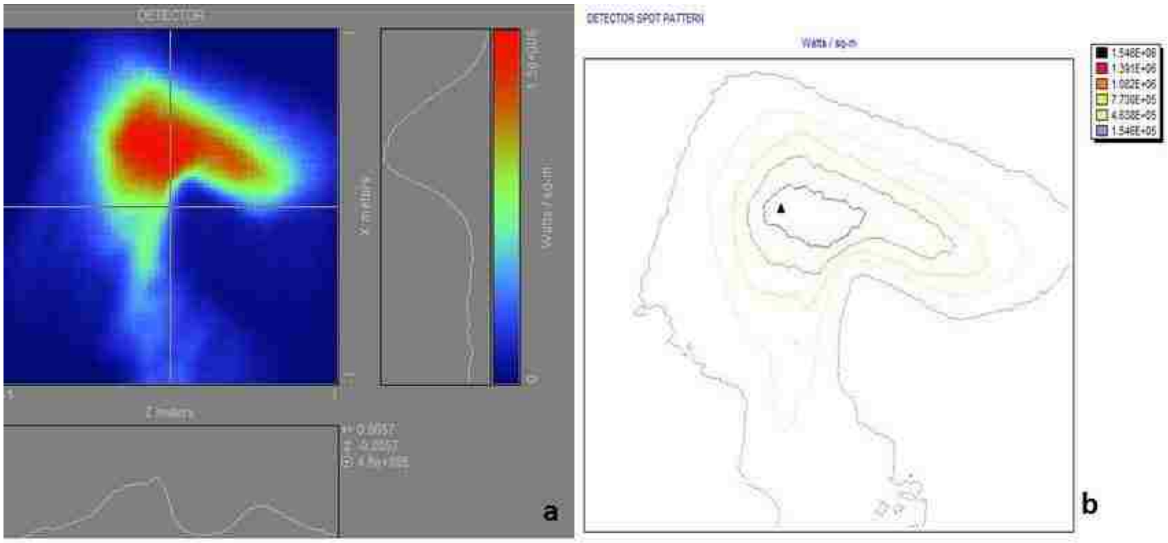

Figure 4.18 NCSETF March 22, 4:00 p.m. (a) Detector insolation plot; (b) Detector contour plot

The simulation results for the spring equinox are very similar to the results of the fall equinox. This is appropriate, since the angular direction in the plane of reflection is similar for those days. The result is nearly analogous concentration ratios over the course of the day for the fall and spring equinoxes. The power outputs vary due to different levels of DNI records for March 22, 1982 and September 23, 1987 within the TMY3 dataset.

The off-axis focusing conditions resulting from the angular difference between the sun position vector and the target position vector in the plane of reflection produces optical coma. Optical coma is defined as a defect of an objective mirror or lens in which rays of light, striking the objective away from the optical axis are not brought to focus in the same image plane [37]. Figure 4.19 demonstrates the effect of optical coma.

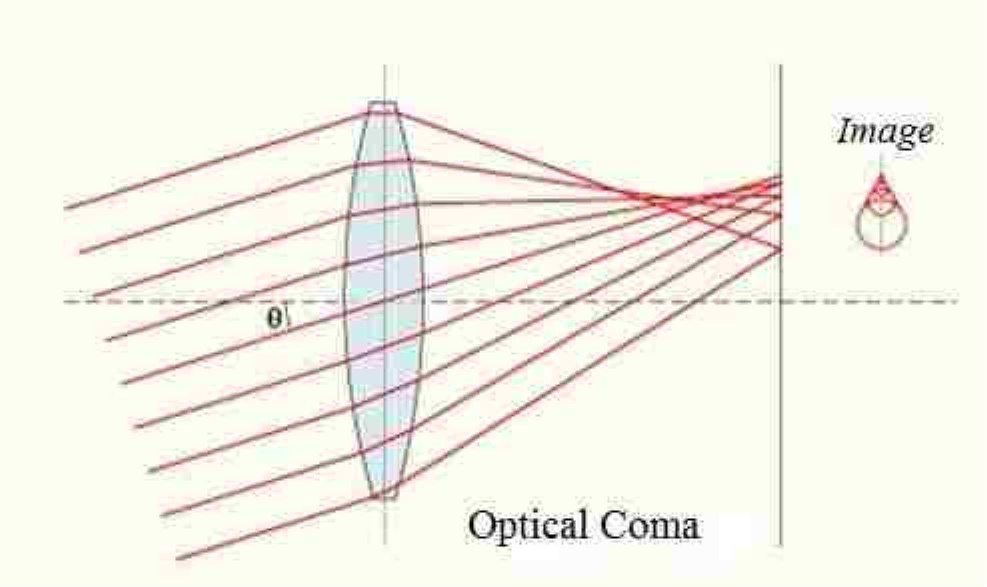

Figure 4.19 Optical coma due to off-axis light source [37]

As presented in Figure 4.19, optical coma arises from the angular difference between the light source and the optical axis. In the case of the NCSETF, the optical axis is the target position vector and the light source is defined by the sun's rays. Coma tends to create comet-like tails on the image, spreading radially out from the optical axis. This comet-like tail effect is demonstrated in several simulations of the NCSETF, including Figure 4.18. The effects of optical coma are directly proportional to the angular difference between the light source and the optical axis. As the angular difference in the plane of reflection increases, the effects of optical coma become more pronounced. Such an effect is also demonstrated in the simulations of the NCSETF, and is the explanation behind the excellent focusing conditions when the sun is directly behind the AP of the heliostat field. It also explains the poor focusing conditions in the morning and afternoon simulations when the angular difference is large.

4.4.6 Time Dependent Results

Time dependent tables and plots were constructed in order to evaluate the performance of the facility over the course of the days simulated. The model of the NCSETF considers all optical losses including cosine, blocking, shading, attenuation, and reflective losses. Table 4.3 portrays the total power collected on the receiver at ground level for each hour simulated with the parallel ray sun source.

Table 4.3 Simulated power output (W) for N-S cornfield algorithm

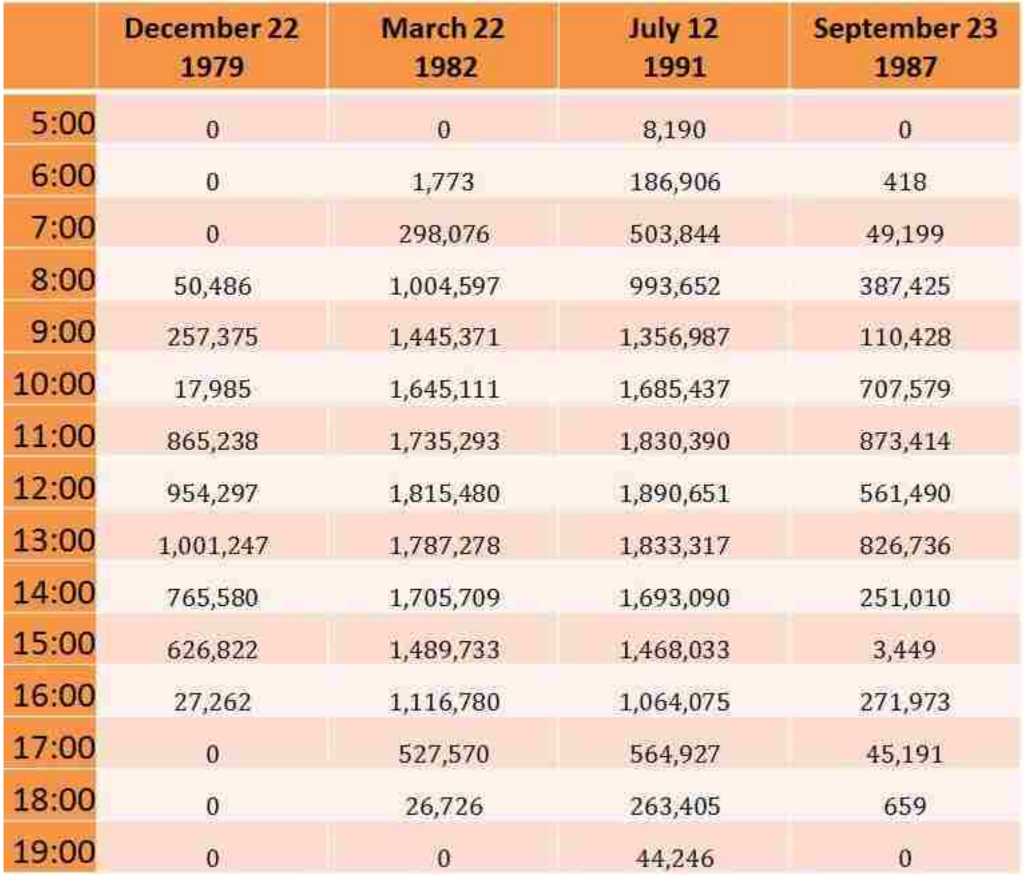

	December 22 1979	March 22 1982	July 12 1991	September 23 1987
5:00	0	0	8,190	0
6:00	0	1,773	186,906	418
7:00	0	298,076	503,844	49,199
8:00	50,486	1,004,597	993,652	387,425
9:00	257,375	1,445,371	1,356,987	110,428
10:00	17,985	1,645,111	1,685,437	707,579
11:00	865,238	1,735,293	1,830,390	873,414
12:00	954,297	1,815,480	1,890,651	561,490
13:00	1,001,247	1,787,278	1,833,317	826,736
14:00	765,580	1,705,709	1,693,090	251,010
15:00	626,822	1,489,733	1,468,033	3,449
16:00	27,262	1,116,780	1,064,075	271,973
17:00	0	527,570	564,927	45,191
18:00	0	26,726	263,405	659
19:00	0	0	44,246	0

The table demonstrates several hours of the four simulated days in which the targeted power output of 1 MW is achieved. Furthermore, the data portrays that as early as 8:00 a.m. and as late as 4:00 p.m. the facility is capable of producing the target 1 MW at the detector. A graphical representation of the data presented in Table 4.3 is depicted by Figure 4.20. The power output plot is followed by a plot simulating the optical efficiency of the NCSETF for each of the hours modeled, Figure 4.21. The optical efficiency plot is based strictly on the power received on the detector at ground level. Concentration is not considered in the optical efficiency.

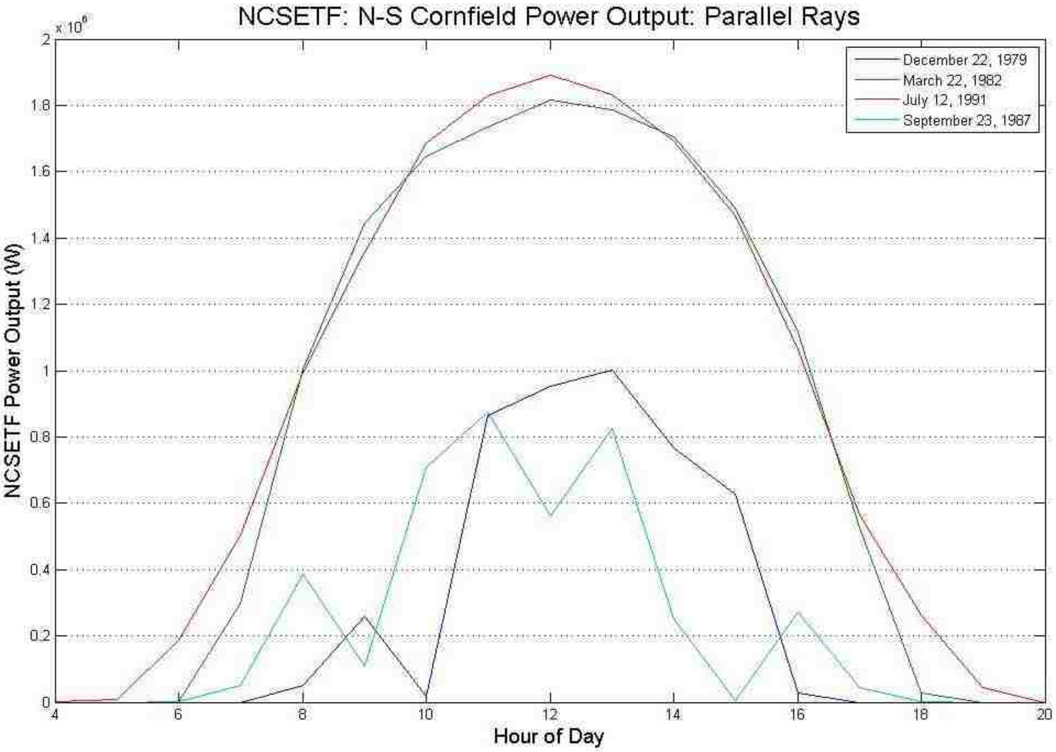

Figure 4.20 Simulated power output: N-S cornfield with parallel rays

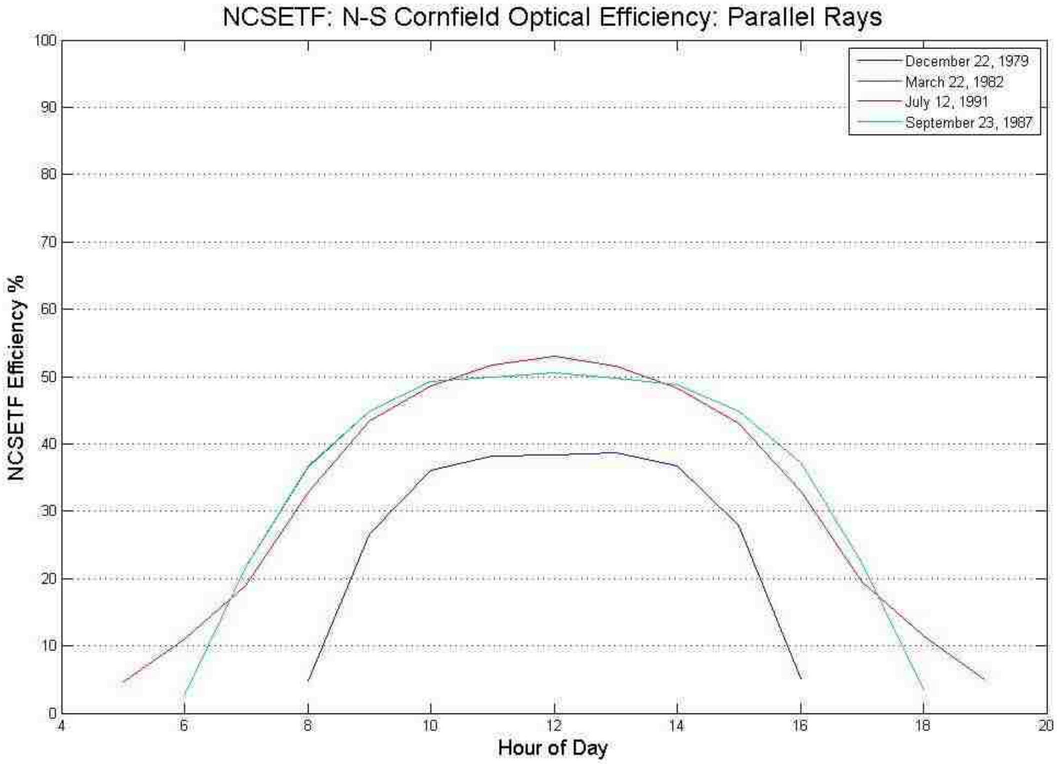

Figure 4.21 Simulated optical efficiency: N-S cornfield with parallel rays

The power output and optical efficiency plots provide useful insight as to the simulated performance of the NCSETF over time. The power curves demonstrate utilizable hours for operation testing of the facility, ranging from 7:00 a.m. until 5:00 p.m. Furthermore, days with relatively high levels of DNI are capable of achieving almost twice the targeted output, while days with significantly lower levels of utilizable DNI are still capable of producing at or near the target output of 1 MW.

The efficiency curves establish significant effects in terms of the optical behavior of the facility. First, they demonstrate that the facility is optically more efficient during days of higher sun elevation. This makes sense, since the effects of blocking and shading are less the higher the sun is in the sky. The efficiency curves also allow for the significant effects of cosine losses in the afternoon and morning hours to be visualized. It is also observed that the optical efficiency is nearly identical for the facility on the spring and fall equinoxes.

4.5 N-S Cornfield Simulations with Realistic Solar Disk

4.5.1 Sun Source Verification

In order to verify proper behavior of the sun's rays within the ray trace, a simulation was first executed utilizing a single heliostat with a known focal length. The heliostat chosen was centered 100 m directly north of the tower, producing a focal length of 125.6 m. The simulation was implemented for December 22, 1979 at solar noon when the sun source is aligned directly south of the tower. Therefore, the sun, tower and heliostat are all co-linear. The simulation hour was chosen because optical aberrations due to the dish shaped heliostat are minimal, allowing for nearly point focusing with parallel rays as presented in Figure 4.14. By minimizing optical aberrations due to the shape of the heliostat, a single heliostat produces an image of the sun on the detector. The diameter of that image can be calculated with the known distance of the heliostat from the down beam reflector. The calculated diameter is presented in equation (4.1), and the NCSETF simulated sun spot produced by the single heliostat is presented in Figure 4.22.

$$SUN_{Diameter} = \tan(0.5^{\circ})*125.6\ m \approx 1.1\ m \tag{4.1}$$

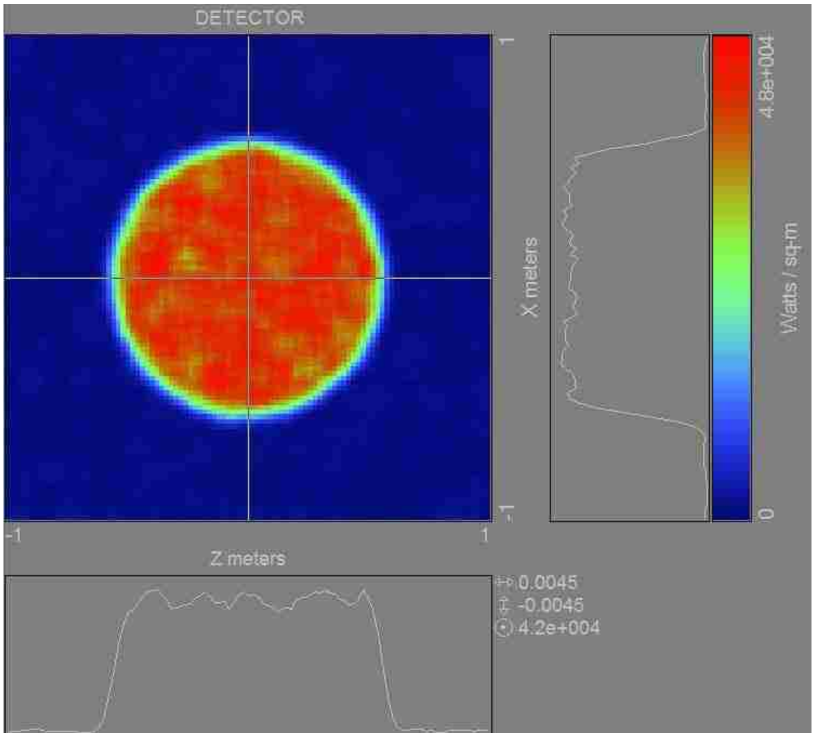

Figure 4.22 Single heliostat sun spot: Focal length = 125.6 m

Comparing the calculated diameter, equation (4.1), with the simulated diameter, Figure 4.22, it can be observed that the diameters are nearly equivalent. Conclusively, the simulated scatter surface is producing proper divergence characteristics of the sun's rays within the ASAP® model of the NCSETF.

4.5.2 Presentation Overview

For each day simulated the outputs of the NCSETF model are presented in detail for the hours of 9:00 a.m., 12:00 p.m., and 4:00 p.m. with a realistic solar disk. General trends are then established for the output of the facility over the course of the four days modeled utilizing a realistic sun source that demonstrates appropriate divergence characteristics as described in section 3.3.3. Similar to the simulations implemented with parallel rays, power output and concentration trends are also established along with the optical efficiency of the facility for the days modeled. All concentration comparisons made between the realistic sun source and an idealized point source are based on the highest concentric ring concentration of the contour plots.

4.5.3 TMY3 July 12, 1991 Simulation

The N-S cornfield layout was simulated with diverging rays for the same hours as the parallel ray simulations, starting with July 12, 1991 at solar noon. The 3D visualization of that ray trace is realized in Figure 4.23.

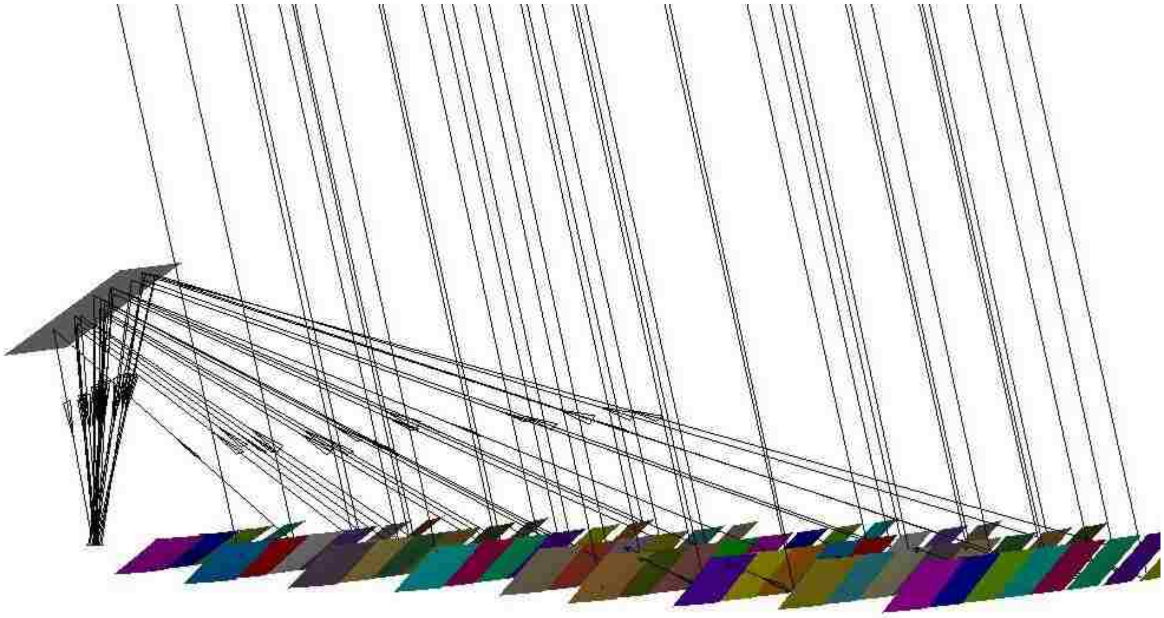

Figure 4.23 NCSETF ray trace utilizing NSCHFL algorithm with diverging rays

The detector spot pattern and contour plot at solar noon for the N-S cornfield configuration are presented in Figure 4.24. Figure 4.24 is followed by similar plots for the hours of 9:00 a.m. and 4:00 p.m. in Figures 4.25 and 4.26, respectively. Figure 4.24 demonstrates a spot size centered just south of the origin, ranging in concentration from 383 suns to a maximum of 3,826 suns. At the middle of the detector, centered directly below the down beam mirror, a concentration of 3,656 is achieved. Furthermore, a total of 1,871,802 W are accumulated on the detector at ground level. Figure 4.25 presents a concentration ranging from 137 suns to 1,332 suns for the hour ending at the timestamp of 9:00 a.m. The rays are congregated to the west side of the detector. At the center of the detector is a concentration of 1,118 suns. A total of 1,268,711 W are collected on the receiver. For the hour of 4:00 p.m. concentration ranges from 84 suns to 779 suns, as presented in Figure 4.26, with a 501 suns concentration at the detector center. A total of 994,113 W are simulated to be received on the detector.

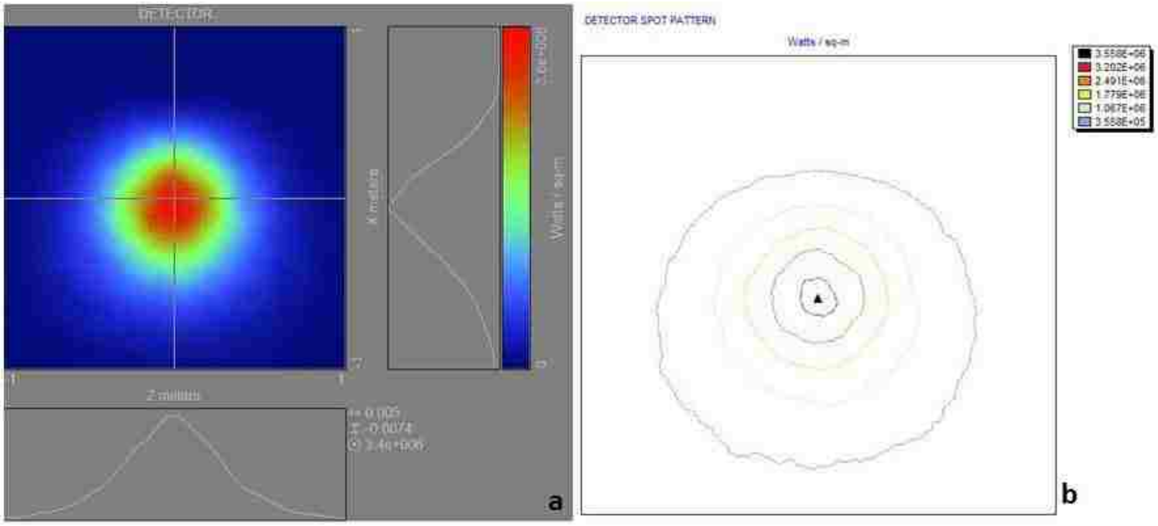

Figure 4.24 NCSETF July 12, 12:00 p.m. (a) Detector insolation plot; (b) Detector contour plot

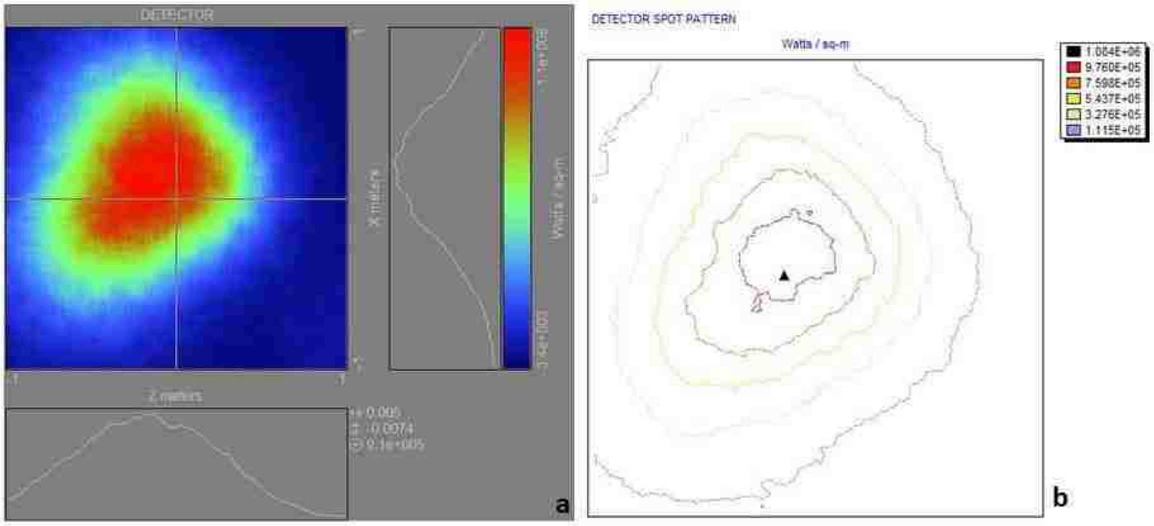

Figure 4.25 NCSETF July 12, 9:00 a.m. (a) Detector insolation plot; (b) Detector contour plot

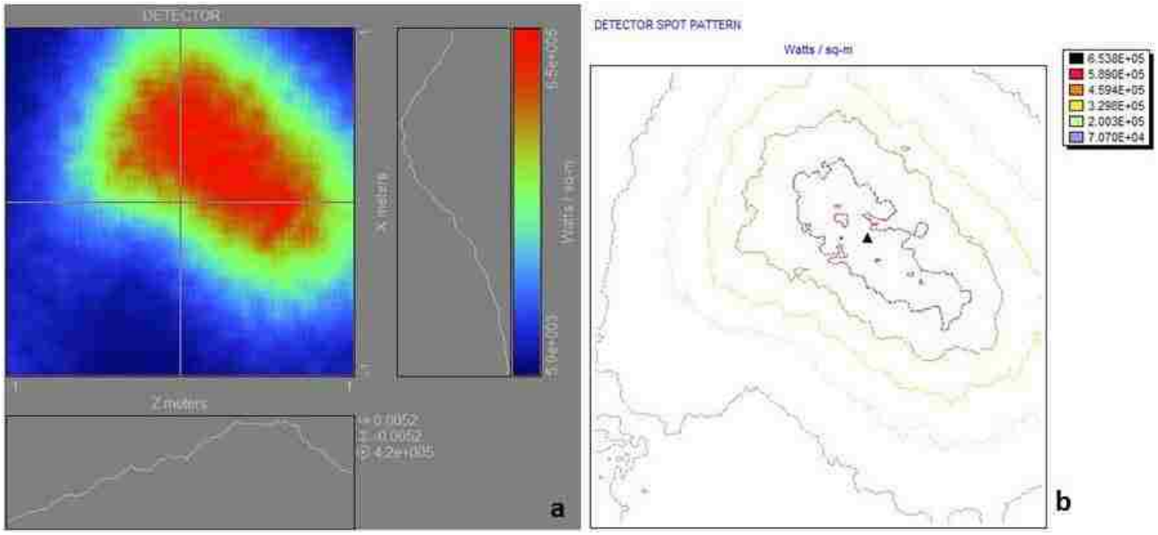

Figure 4.26 NCSETF July 12, 4:00 p.m. (a) Detector insolation plot; (b) Detector contour plot

The behavior of the spot patterns depicted in Figures 4.24, 4.25, and 4.26 lead to several observations. The local hot spots and shape of the concentrated rays vary over the course of the day. At 9:00 a.m., the bulk of rays tend to be concentrated toward the west side of the detector. Conversely, at 4:00 p.m., rays tend to be bundled on the east side of the detector. At local noon, the rays are relatively focused from east to west, but weighed slightly heavier towards the south side of the collector. The observations are similar to the outputs provided by the parallel ray simulations as presented in Figures 4.7, 4.8, and 4.9.

The differences between the parallel rays and diverging rays simulations for July 12, 1991 pertain to the concentration and shape of the spot received on the detector. For the simulation hour of 12:00 p.m. the realistic solar disk simulation produces a slightly larger and more circular shaped spot on the detector. Furthermore, the maximum concentric ring concentration drops approximately 27% with the realistic sun source. For the 9:00 a.m. diverging rays simulation the maximum concentric concentration is reduced by approximately 16% on the detector. Similarly, for the 4:00 p.m. simulation the concentration decreases by about 14% for the realistic sun source implementation.

4.5.4 TMY3 September 23, 1987 Simulation

The simulated outputs for the fall equinox, September 23, 1987 are presented for the hours 9:00 a.m., 12:00 p.m., and 4:00 p.m. utilizing the realistic sun source. Figure 4.27 demonstrates a spot size centered north of the origin at 9:00 a.m., ranging in concentration from 251 suns to a maximum of 2,514 suns. The obtained concentration at the detector center is 2,344 suns. Additionally, a total of 107,821 W are accumulated on the detector at ground level for the hour of 9:00 a.m. Figure 4.28 presents a concentration ranging from 396 suns to 3,936 suns for the hour ending at the timestamp of 12:00 p.m. The rays are centered just south of the origin of the detector. The concentration at the middle of the detector is 3,806 suns. A total of 561,328 W are collected on the receiver. For the hour of 4:00 p.m. concentration ranges from 123 suns to 1,207 suns as presented in Figure 4.29. The center of the receiver yields 895 suns concentration. A total of 256,004 W are simulated to be received on the detector.

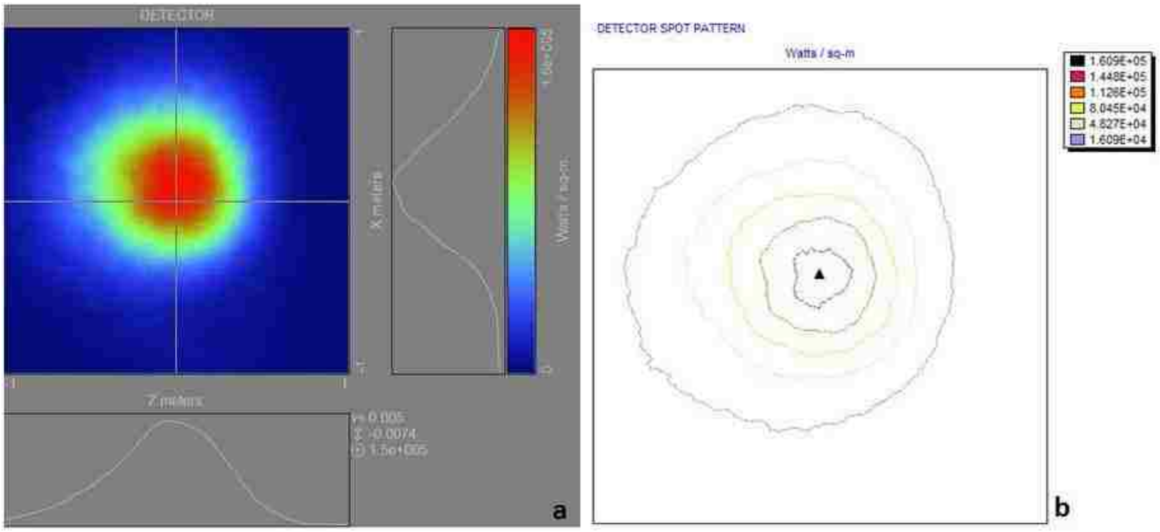

Figure 4.27 NCSETF Sept 23, 9:00 a.m. (a) Detector insolation plot; (b) Detector contour plot

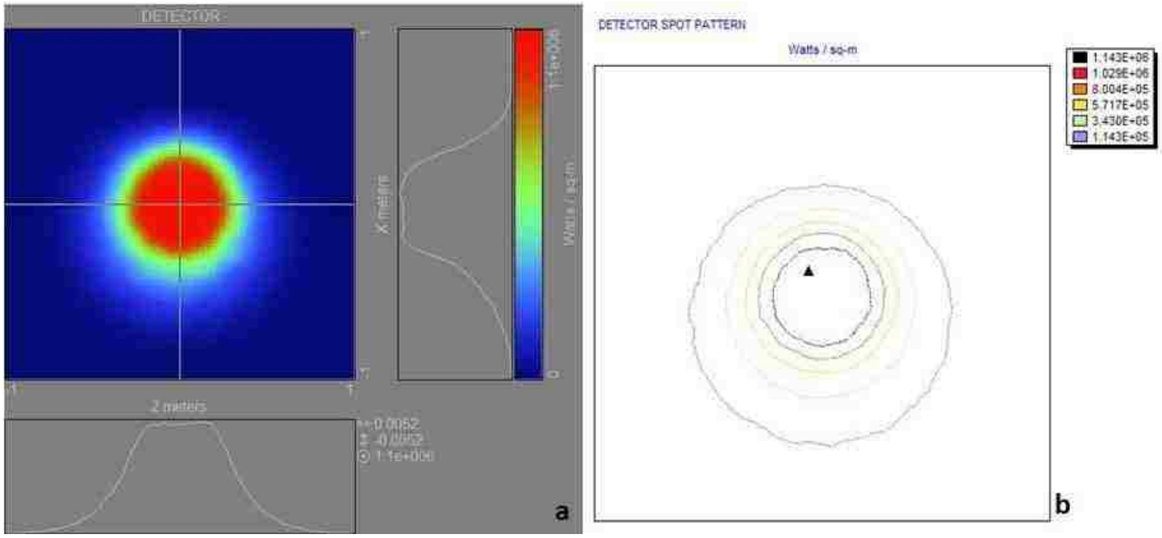

Figure 4.28 NCSETF Sept 23, 12:00 p.m. (a) Detector insolation plot; (b) Detector contour plot

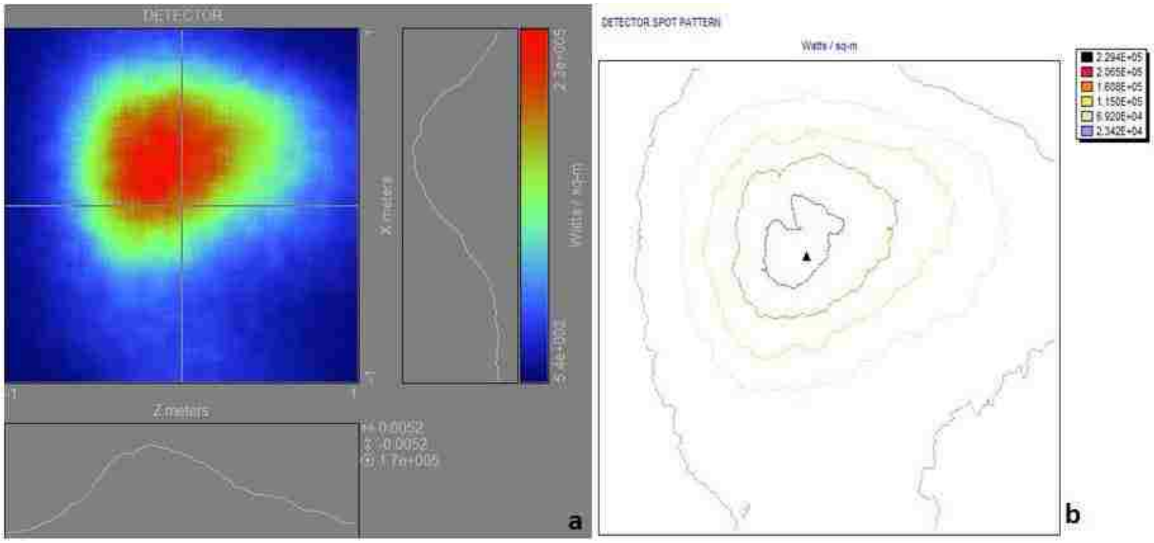

Figure 4.29 NCSETF Sept 23, 4:00 p.m. (a) Detector insolation plot; (b) Detector contour plot

Analyzing the results of the realistic sun source simulations leads to several observations for the September 23, 1987 modeled hours. Like the July 12, 1991 simulations, the diverging rays produce a larger spot size and less concentration on the detector at ground level. For the simulation hours of 9:00 a.m., 12:00 p.m., and 4:00 p.m., there is a decrease in maximum concentric ring concentration of 47%, 63%, and 40% respectively on the detector. In comparison to the July 12, 1991 simulations, the realistic sun source has a greater effect on the achievable concentration ratios for the September 23, 1987 simulations. Again, because the sun is lower in the sky for the month of September than the month of July, the angular difference in the plane of reflection is less. The result is less optical aberrations due to off-focus conditions of the dish shaped heliostats. Consequently, the focusing conditions with parallel rays are better for September than July as previously established in section 4.4.3. With a realistic sun source, however, the focusing conditions are limited by the divergence of the sun's rays, justifying the larger decrease in maximum concentric concentration.

4.5.5 TMY3 December 22, 1979

The simulation results for December 22, 1979 during the hours of 9:00 a.m., 12:00 p.m., and 4:00 p.m. are presented respectively for the realistic sun source. Figure 4.30 demonstrates a sun spot centered north of the origin at 9:00 a.m., ranging in concentration from 110 suns to a maximum of 1,101 suns. At the midpoint of the detector is a concentration of 1,036 suns. A total of 249,976 W are gathered on the detector at ground level within the simulation. Figure 4.31 presents a concentration ranging from 223 suns to 2,233 suns for the hour ending at the timestamp of 12:00 p.m. The rays are concentrated to a sun spot centered directly at the origin of the detector reaching 2,160 suns. A total of 954,155 W are collected on the receiver. For the hour of 4:00 p.m. concentration ranges from 15 suns to 146 suns, with a centered concentration of 109 suns as presented in Figure 4.32. A total of 24,830 W are simulated to be received on the detector.

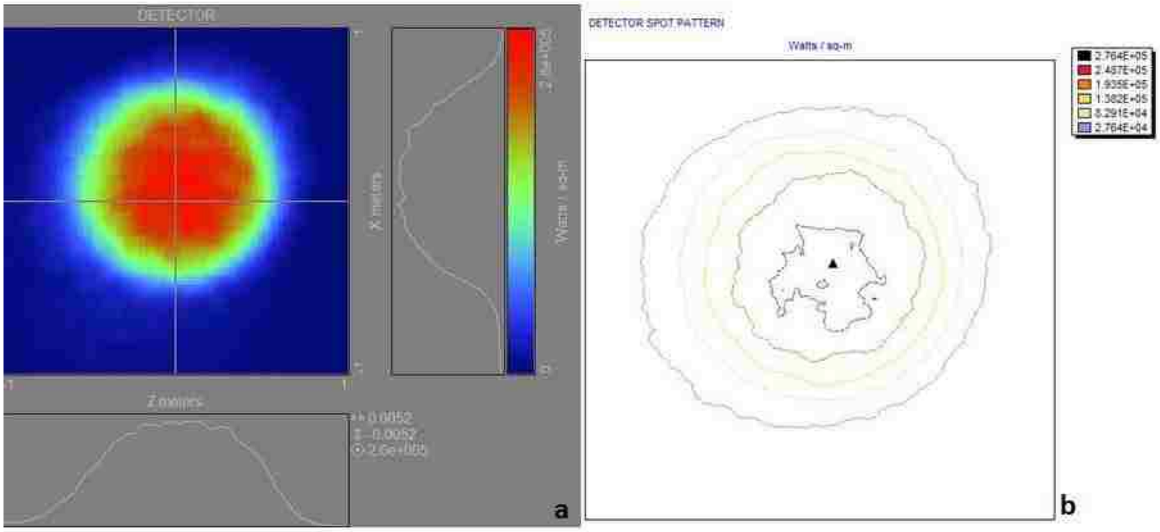

Figure 4.30 NCSETF Dec 22, 9:00 a.m. (a) Detector insolation plot; (b) Detector contour plot

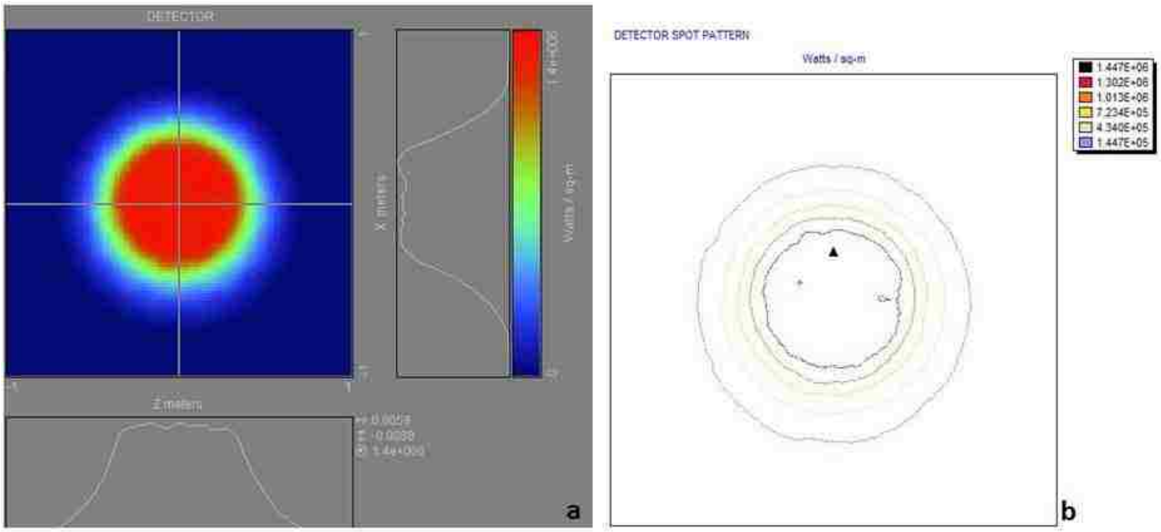

Figure 4.31 NCSETF Dec 22, 12:00 p.m. (a) Detector insolation plot; (b) Detector contour plot

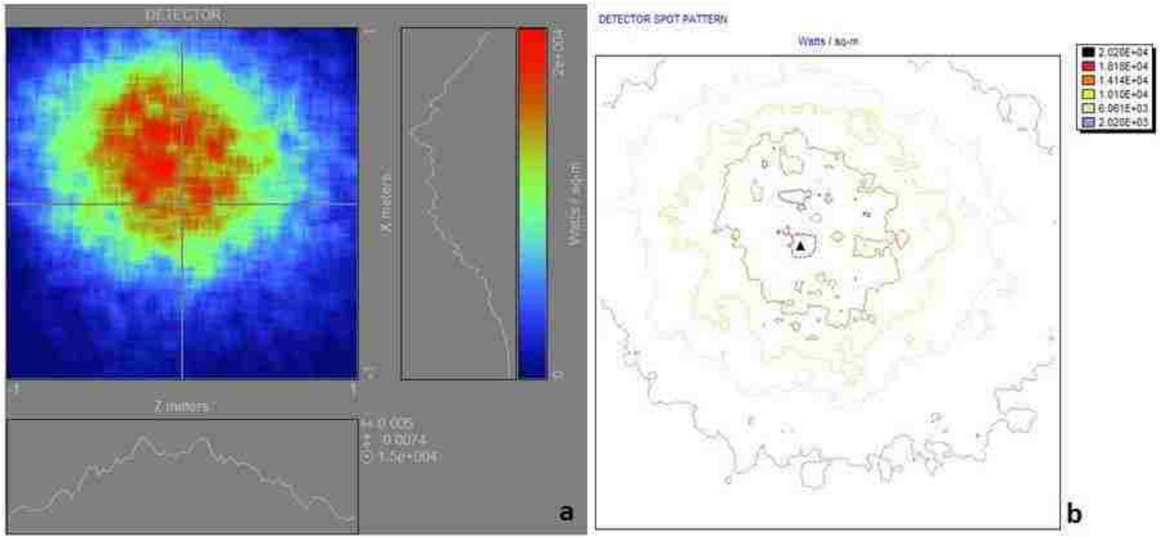

Figure 4.32 NCSETF Dec 22, 4:00 p.m. (a) Detector insolation plot; (b) Detector contour plot

The results for the December 22, 1979 simulation with a realistic sun source are very insightful. As previously established, the elevation of the sun for the winter solstice at solar noon in Las Vegas is only 30.467°. Resultantly, the angular difference between the sun position vector and the target position vector in the plane of reflection is small for each heliostat. Therefore, the objects utilized to simulate converging heliostats are nearly entirely in focus. For the parallel rays simulations, the result is a very compact bundle of rays at the origin, attaining extremely high levels of concentration as presented in section 4.4.4. In actuality, the achievable concentration is limited by the angular size of the sun in the sky, as demonstrated in Figures 4.30, 4.31, and 4.32. For the simulation hours of 9:00 a.m., 12:00 p.m., and 4:00 p.m., there is a respective 89%, 98%, and 57% decrease in maximum concentric ring concentration.

4.5.6 TMY3 March 22, 1982

The simulation results for March 22, 1982 during the hours of 9:00 a.m., 12:00 p.m., and 4:00 p.m. are respectively displayed for the implementation utilizing diverging solar rays. Figure 4.33 demonstrates a spot size centered north of the origin at 9:00 a.m., ranging in concentration from 253 suns to a maximum of 2,526 suns. At the center of the receiver a concentration of 2,387 suns is attained. Furthermore, a total of 1,410,887 W are accumulated on the detector at ground level. Figure 4.34 presents a concentration ranging from 395 suns to 3,952 suns for the hour ending at the timestamp of 12:00 p.m. The rays are centered just south of the origin on the detector. At the detector center is a concentration of 3,858 suns. A total of 1,815,041 W are collected on the receiver. For the hour of 4:00 p.m. concentration ranges from 122 suns to 1,222 suns as presented in Figure 4.35. The center of the detector reaches a concentration of 883 suns. A total of 1,051,409 W are simulated to be received on the detector.

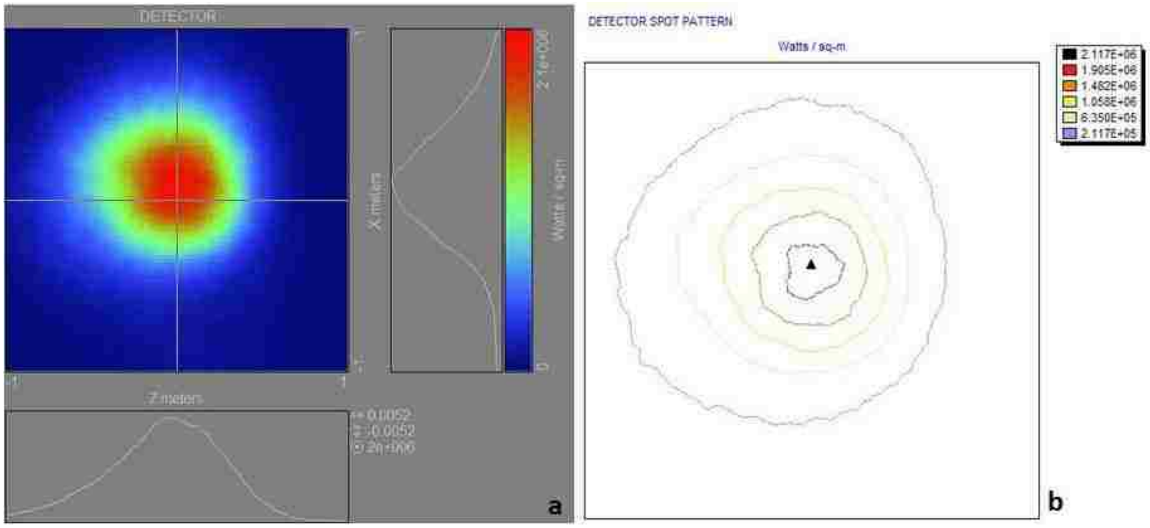

Figure 4.33 NCSETF March 22, 9:00 a.m. (a) Detector insolation plot; (b) Detector contour plot

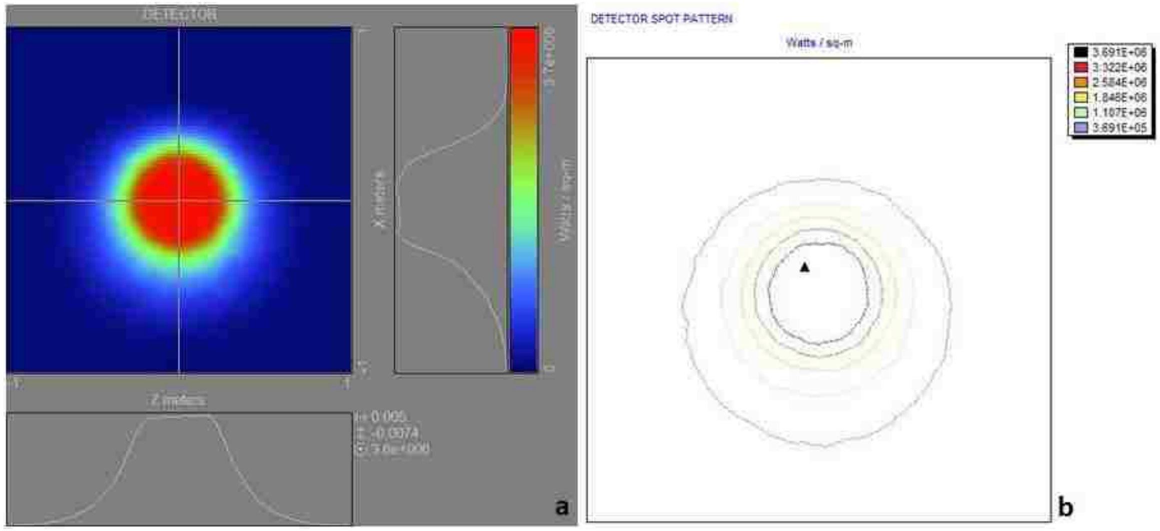

Figure 4.34 NCSETF March 22, 12:00 p.m. (a) Detector insolation plot; (b) Detector contour plot

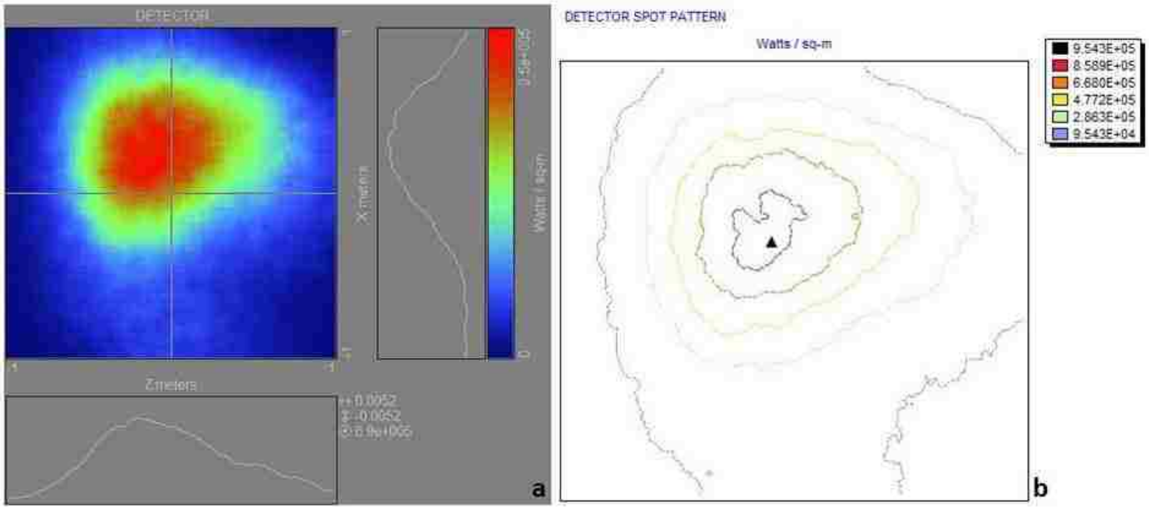

Figure 4.35 NCSETF March 22, 4:00 p.m. (a) Detector insolation plot; (b) Detector contour plot

Similar to the parallel ray simulations, the simulation results for the spring equinox are nearly analogous to the results for the fall equinox when a realistic solar disk is implemented within the model. Like the idealized point source simulations this is again suitable, since the angular direction in the plane of reflection is comparable for those days. For the simulation hours of 9:00 a.m., 12:00 p.m., and 4:00 p.m., there is a decrease in maximum concentric ring concentration of 46%, 63%, and 38% respectively on the detector. As expected, the decrease in maximum concentric ring concentration due to a realistic solar disk is nearly identical for equivalent hours on the spring and fall equinoxes.

4.5.7 Time Dependent Results

Time dependent tables and plots were constructed in order to evaluate the performance of the facility over the course of the days simulated with a realistic sun source. Again, the model of the NCSETF considers all optical losses including cosine, blocking, shading, attenuation, and reflective losses. Table 4.4 portrays the total power collected on the receiver at ground level for each hour simulated with a realistic sun source that incorporates diverging rays.

Table 4.4 Simulated power output (W): N-S cornfield with diverging rays

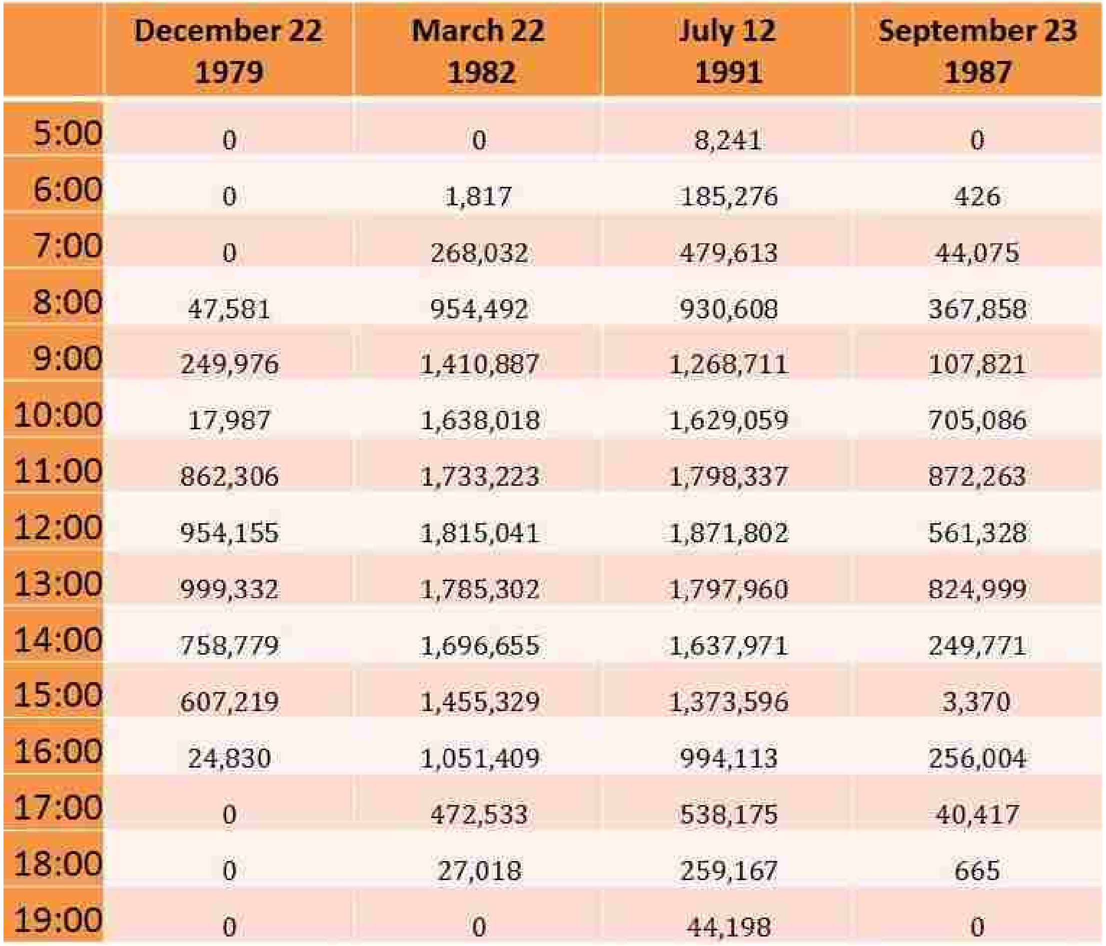

	December 22 1979	March 22 1982	July 12 1991	September 23 1987
5:00	0	0	8,241	0
6:00	0	1,817	185,276	426
7:00	0	268,032	479,613	44,075
8:00	47,581	954,492	930,608	367,858
9:00	249,976	1,410,887	1,268,711	107,821
10:00	17,987	1,638,018	1,629,059	705,086
11:00	862,306	1,733,223	1,798,337	872,263
12:00	954,155	1,815,041	1,871,802	561,328
13:00	999,332	1,785,302	1,797,960	824,999
14:00	758,779	1,696,655	1,637,971	249,771
15:00	607,219	1,455,329	1,373,596	3,370
16:00	24,830	1,051,409	994,113	256,004
17:00	0	472,533	538,175	40,417
18:00	0	27,018	259,167	665
19:00	0	0	44,198	0

Similar to the idealized point source simulations, the table demonstrates several hours of the simulated days in which the targeted power output of 1 MW is attainable. Furthermore, the data again portrays that as early as 9:00 a.m. and as late as 4:00 p.m. the facility is capable of achieving the targeted 1 MW at the detector. A graphical representation of the data presented in Table 4.4 is illustrated in Figure 4.36. Figure 4.36 is followed by optical efficiency curves for the simulated days with a realistic solar disk in Figure 4.37. Again, the optical efficiency plot is based strictly on the power received on the detector at ground level, neglecting concentration.

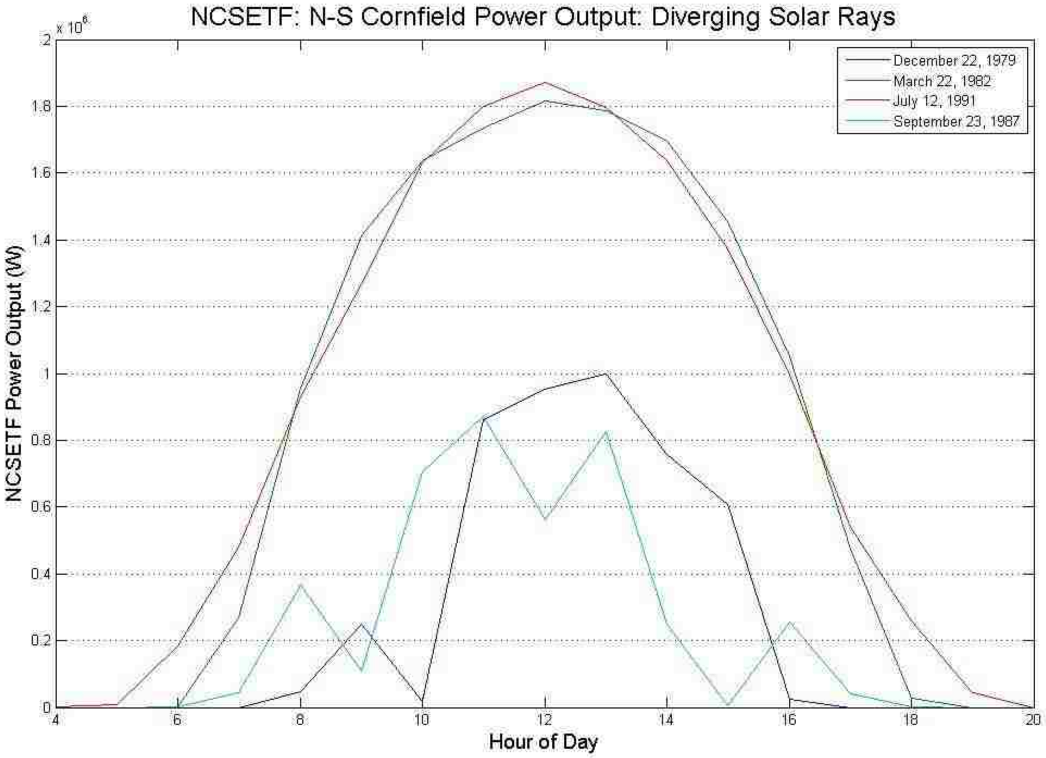

Figure 4.36 Simulated power output: N-S cornfield configuration with diverging rays

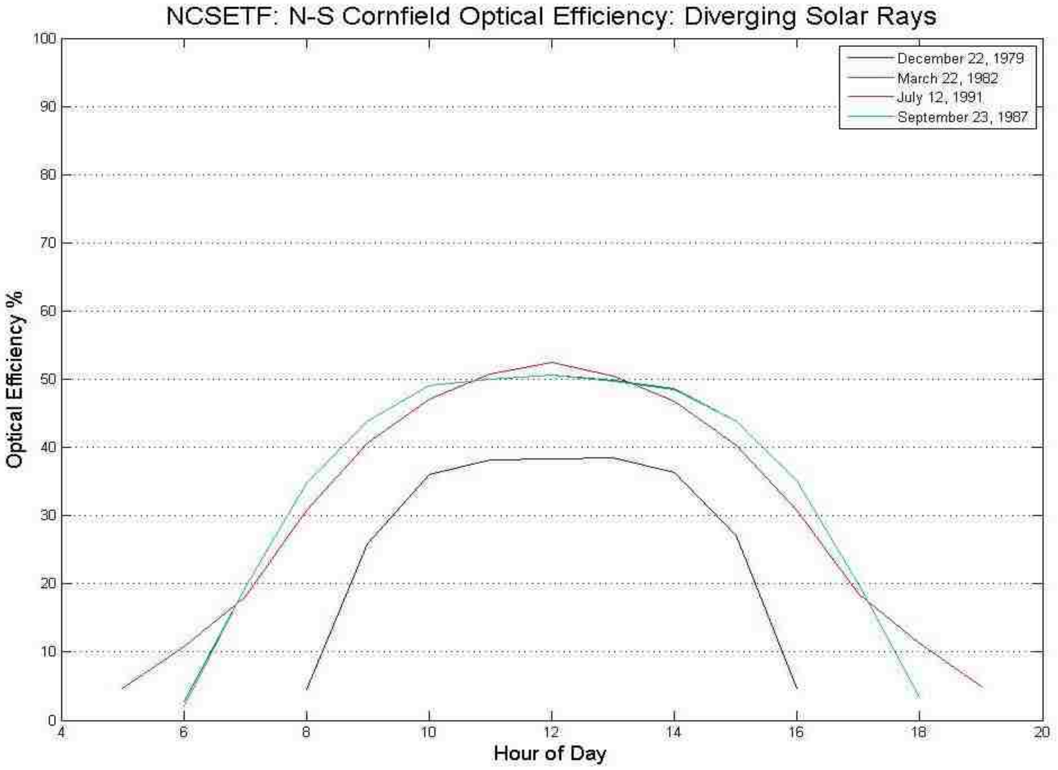

Figure 4.37 Simulated optical efficiency: N-S cornfield configuration with diverging rays

The power output and optical efficiency plots provide an understanding of the simulated performance of the NCSETF in terms of available power. The plots also allow for the trends demonstrated with a realistic solar disk to be compared to those of an ideal point source. Most significantly, the power output and optical efficiency are nearly identical for the diverging ray simulations as the parallel ray simulations. The power curves again demonstrate a broad window of hours in which significant levels of power are received at the detector, ranging from 7:00 a.m. until 5:00 p.m. Furthermore, days with relatively high levels of DNI are capable of achieving almost twice the targeted output, while days with significantly lower levels of utilizable DNI are still capable of producing at or near the target output of 1 MW.

Time dependent concentration tables and curves were also produced for the simulations incorporating the divergence characteristics of the sun's rays. Table 4.5 demonstrates the concentration range amongst the spot received at the detector based on the concentric rings of the contour plots. Table 4.6 depicts the concentration received at the center of the detector for each of the simulated hours of the NCSETF.

Table 4.5 Simulated concentration range (W/m^2): Diverging rays

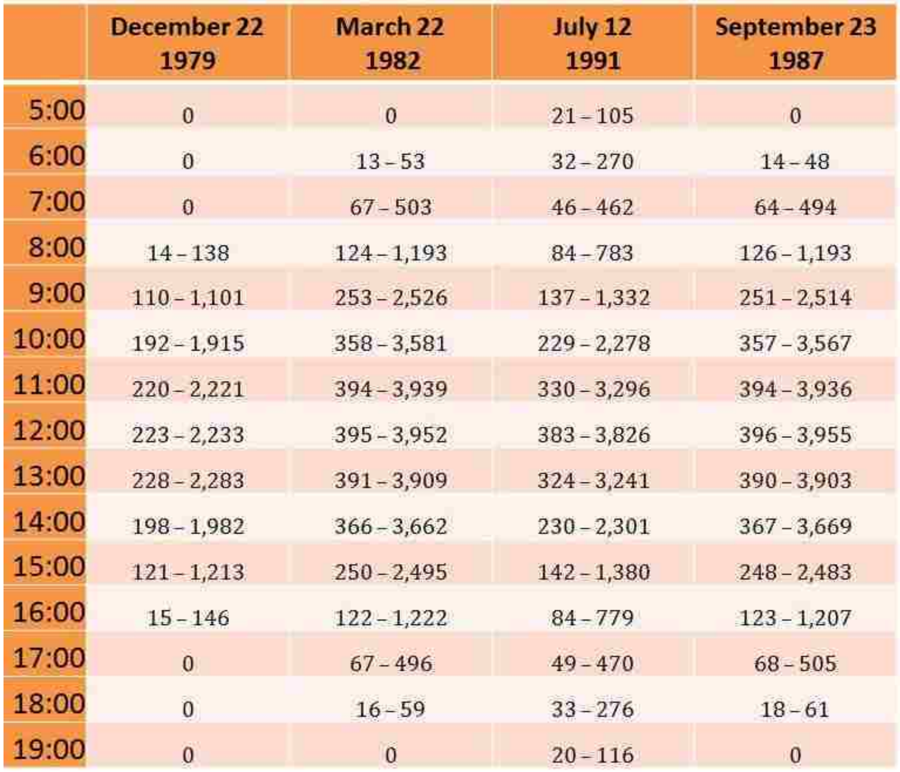

	December 22 1979	March 22 1982	July 12 1991	September 23 1987
5:00	0	0	21 – 105	0
6:00	0	13 – 53	32 – 270	14 – 48
7:00	0	67 – 503	46 – 462	64 – 494
8:00	14 – 138	124 – 1,193	84 – 783	126 – 1,193
9:00	110 – 1,101	253 – 2,526	137 – 1,332	251 – 2,514
10:00	192 – 1,915	358 – 3,581	229 – 2,278	357 – 3,567
11:00	220 – 2,221	394 – 3,939	330 – 3,296	394 – 3,936
12:00	223 – 2,233	395 – 3,952	383 – 3,826	396 – 3,955
13:00	228 – 2,283	391 – 3,909	324 – 3,241	390 – 3,903
14:00	198 – 1,982	366 – 3,662	230 – 2,301	367 – 3,669
15:00	121 – 1,213	250 – 2,495	142 – 1,380	248 – 2,483
16:00	15 – 146	122 – 1,222	84 – 779	123 – 1,207
17:00	0	67 – 496	49 – 470	68 – 505
18:00	0	16 – 59	33 – 276	18 – 61
19:00	0	0	20 – 116	0

Table 4.6 Simulated detector center concentration (W/m^2): Diverging rays

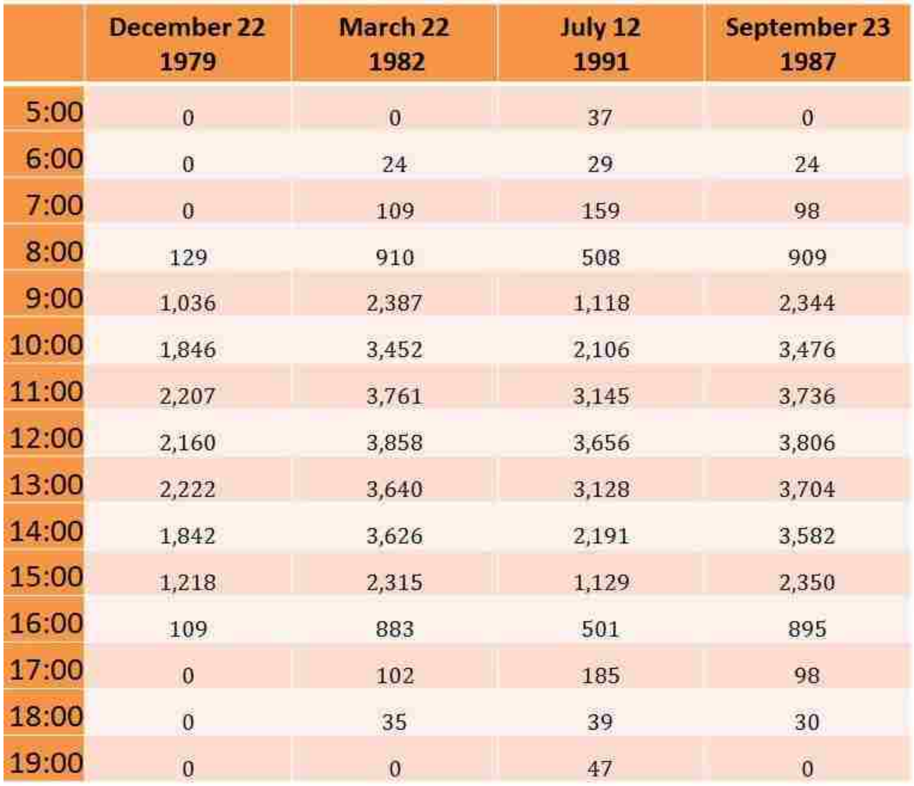

	December 22 1979	March 22 1982	July 12 1991	September 23 1987
5:00	0	0	37	0
6:00	0	24	29	24
7:00	0	109	159	98
8:00	129	910	508	909
9:00	1,036	2,387	1,118	2,344
10:00	1,846	3,452	2,106	3,476
11:00	2,207	3,761	3,145	3,736
12:00	2,160	3,858	3,656	3,806
13:00	2,222	3,640	3,128	3,704
14:00	1,842	3,626	2,191	3,582
15:00	1,218	2,315	1,129	2,350
16:00	109	883	501	895
17:00	0	102	185	98
18:00	0	35	39	30
19:00	0	0	47	0

The tables demonstrate that the NCSETF is capable of producing the targeted 1,000 suns concentration during several hours of the simulated days. Furthermore, the data portrays that nearly 4,000 suns concentration is achievable for the ideal hour of alignment at solar noon on multiple days. A graphical representation of the data presented in Table 4.5 is depicted by Figures 4.38 and 4.39. Figure 4.40 portrays the obtained concentration at the middle of detector, centered directly below the down beam reflector, for each of the simulated hours.

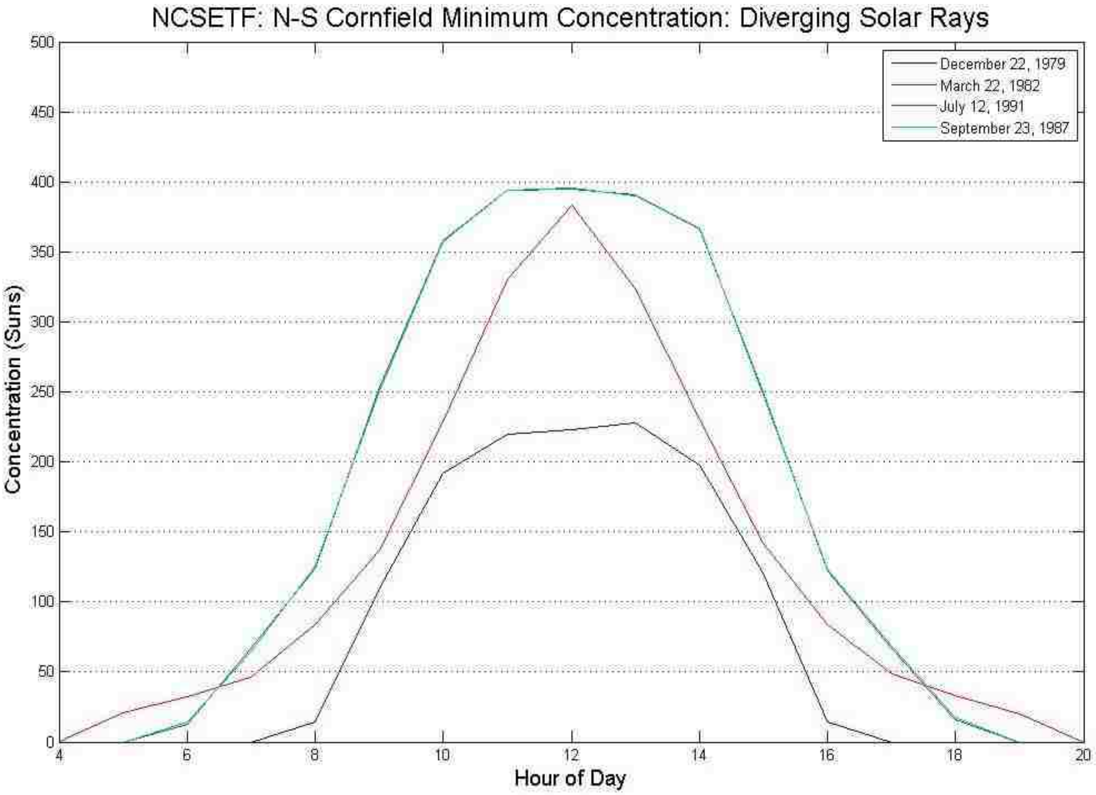

Figure 4.38 Simulated minimum concentration: N-S cornfield with diverging rays

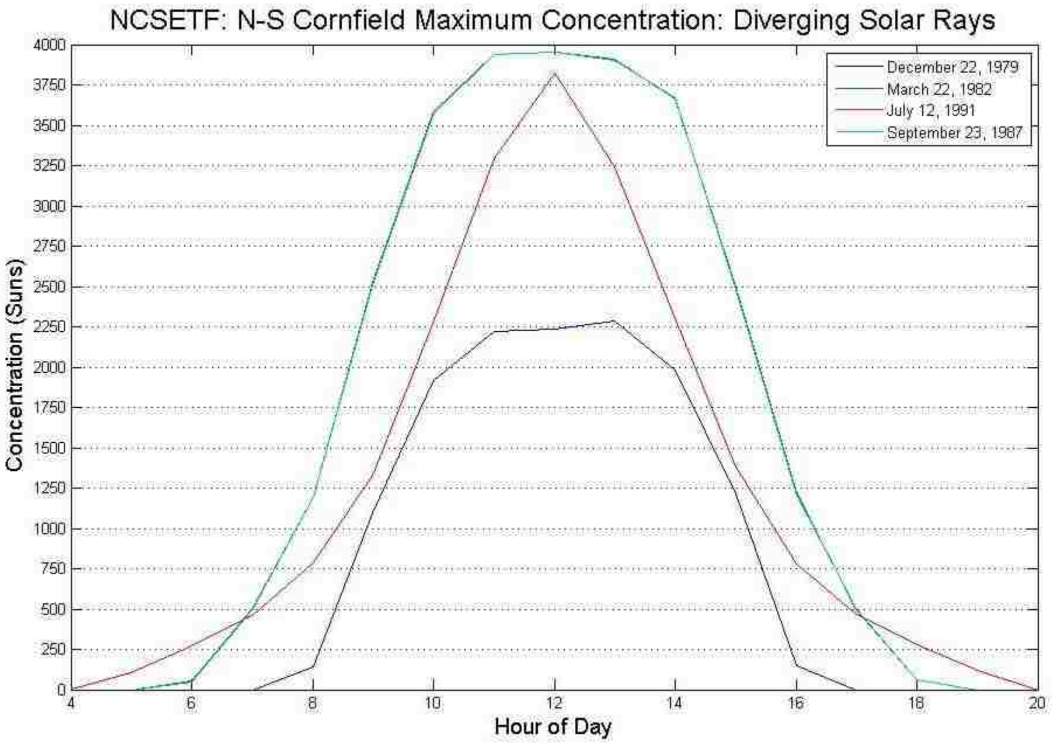

Figure 4.39 Simulated maximum concentration: N-S cornfield with diverging rays

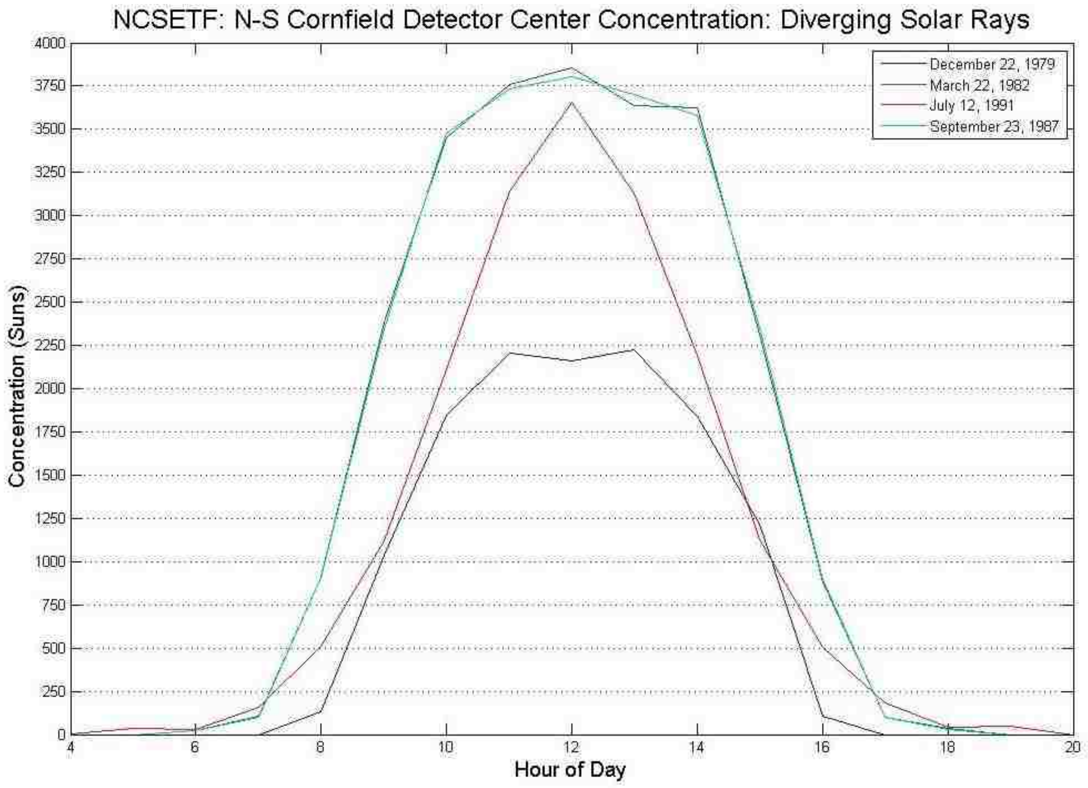

Figure 4.40 Simulated detector center concentration: N-S cornfield with diverging rays

Several trends are established by these concentration curves. The targeted 1,000 suns concentration is achievable as early as 9:00 a.m. and is maintained until 3:00 p.m. for each of the days simulated. Comparing Figures 4.39 and 4.40, the conclusion can be drawn that the concentration at the center of the detector is nearly the maximum obtainable concentration. The differences in concentration become more pronounced for off-noon hours, when the concentrated spot slightly shifts around the detector center due to the simulated shape of the heliostats. At solar noon, however, the detector center concentration is nearly identical to the maximum concentration. This is logical, since the tower, sun source, and center of the heliostat field are co-linear, the dish shaped heliostats are nearly entirely in focus for that hour.

In terms of concentration, one of the most profound observations is that higher levels are achieved for the spring and fall equinoxes than the winter and summer simulation days. A reasonable justification pertains to the focusing conditions of the dish shaped heliostats. For the December 22, 1979 simulations the angular difference between the sun position vector and the target position vector in the plane of reflection is small for each heliostat, rendering them almost entirely in focus. The optical losses, however, are largest for the December 22, 1979, as displayed in Figure 4.37, which greatly effects the achievable concentration. For the July 12, 1991 simulation the angular difference between the sun position vector and the target position vector in the plane of reflection is large for each heliostat because the sun is high in the sky. Therefore, focusing conditions are the worst for the July 12, 1991 implementations in comparison to the other modeled days due to the simulated shape of the heliostats. The spring and fall equinoxes present a balance between optical efficiency of the heliostat field and the focusing conditions of the simulated heliostats. Resultantly, higher levels of concentration are obtained for the spring and fall equinoxes in comparison to the winter and summer simulations. A true non-imaging heliostat as presented by Chen [33] would likely have different focusing conditions, and consequently may not demonstrate the same patterns in terms of achievable concentration over the course of the year.

4.6 Observations of Simulations

When comparing the trends over the course of the simulated days several observations can be made in regards to the output of the facility. Higher concentration levels are achieved for days with lower elevation angles, up to the point in which optical losses outweigh the focusing conditions of the dish shaped heliostats. Days where the sun demonstrates similar height characteristics have similar outputs in terms of concentration and spot formations on the detector. The utilization of parallel rays as a sun source allows for levels of concentration to be obtained that are infeasible. This is due to the divergence characteristics of the sun's rays, resulting from the angular diameter of the sun in the sky. The error propagation due to parallel rays is more pronounced for hours in which the angular difference in the plane of reflection between the sun position vector and the target position vector for each heliostat is minimized. This id due to the fact that optical coma is minimized, allowing for unrealistic levels of concentration to be achieved. Optical aberrations due to the simulated shape of the heliostats are much greater for off-noon hours, causing the focal point of the concentrated rays to shift around the origin of the detector.

In terms of attainable power and concentration for the NCSETF, the simulated results demonstrate the achievability of the targeted 1 MW power and 1,000 suns concentration for several hours over the course of the days modeled. Simulating the divergence characteristics of the sun's rays has a pronounced effect on the spot shape and concentration, but little effect on the accumulated power and optical efficiency of the facility.

The discrepancy between the simulated concentration of the NCSETF and that demonstrated in traditional power tower systems, as presented in Table 1.1, can justifiably be attributed to a variety of factors. The smooth parabolic heliostats simulated in the model of the NCSETF are capable of producing tighter convergence characteristics than the faceted heliostats as described by Chen [33]. Faceted heliostats are limited to a spot size no smaller than the individual mirror tiles. During optimal focusing conditions, when off-axis coma of the simulated heliostats is minimized as presented in Figure 4.14, smooth parabolic heliostats are capable of achieving nearly point focusing and thus obtain high levels of concentration. The segmented approximation of mirror tile facets to the parabolic shape of the converging heliostats results in concentration losses [38]. Furthermore, other geometric imperfections may also attribute to the difference in concentration between that simulated for the NCSETF and that demonstrated in conventional tower systems. For example, facet misalignments as well as structural bending and deformation of the heliostats all lead to concentration losses of practical tower systems, but are not accounted for in the simulated model of the NCSETF.

In addition to geometric imperfections, tracking and pointing inaccuracies can have a drastic effect on achievable concentration [38]. The simulation of the NCSETF does not account for such pointing and tracking inaccuracies, and therefore the spot size is limited only by the divergence characteristics of the sun and optical coma. In real world implementations aiming and tracking deficiencies often arise that can be difficult to simulate. For example, wind loading on the heliostats can cause aiming imperfections that significantly reduce focusing conditions of the heliostat field and consequently concentration. A combination of all of these factors present a conceivable explanation for the difference in simulated maximum concentration of the NCSETF at 3,955 suns and that demonstrated in tower top systems capable of achieving 1,000 suns concentration.

CHAPTER 5

CONCLUSION & CONTINUING WORK

5.1 Conclusion

In conclusion, the motivation behind the design and development of a novel solar down beam test facility utilizing Newtonian optics was presented. The NCSETF was designed with a flat planar down beam mirror, offering several benefits in terms of a testing facility. The optical design allows for the entire power output of the facility to be utilized by a single experiment, or distributed over several experiments operating simultaneously. A planar down beam mirror also allows for the focusing conditions of the facility to be relatively similar to those of traditional solar power towers. Furthermore, a planar down beam mirror is relatively simple to design and construct. This fits in nicely with the overall motif of the facility, which is to utilize leased, non-permanent infrastructure to minimize capital costs. Additionally, thermal expansion issues are easier to address with a planar down beam reflector because the mirror can be constructed to deform uniformly without distorting the optics of the system.

A facility to be implemented in southern Nevada was then optically evaluated utilizing ray tracing techniques. As a result, the optical geometry and performance of the system presented apply specifically to conditions of a facility located in southern Nevada. The NCSETF design includes a relatively short down beam reflector height and a compact heliostat field constructed close to the tower. Simulations were implemented for both an idealized point source as well as a realistic sun source. The parallel rays demonstrate the focusing conditions of the simulated heliostats, and the diverging solar rays simulate a more realistic real world performance of the facility in terms of power outputs and concentrations.

The results of the simulated models establish the achievability of the targeted 1 MW power to be collected at ground level for several hours of the day over the course of the year. Additionally, the simulations demonstrate that with a realistic sun source, incorporating the divergence behavior of the sun's rays, the targeted 1,000 suns concentration is also achievable. Concentration distribution and contour plots are presented allowing for the effects of time of day, as well as time of year, on the concentration and power output of the facility to be realized. Furthermore, power output and efficiency plots have been established for the NCSETF taking into consideration the optical losses of the system; including cosine, blocking, shadowing, attenuation, and reflective losses.

5.2 Model Improvements

Due to the internal register limitations of ASAP®, the objects utilized to simulate non-imaging heliostats had to be adapted from true non-imaging heliostats. This was to accommodate the restriction on the number of input parameters that can be imported into ASAP® and assigned to variables. Focusing heliostats as described by Chen [33] require faceted mirror tiles, and therefore have different focusing characteristics than smooth parabolic shapes. The achievable concentration of a true non-imaging heliostat as presented by Chen [33] is limited primarily by the individual mirror tile facet size along with the divergence characteristics of the sun's rays. For example, if 1 m^2 mirror tiles were utilized the spot size on the detector could be no smaller than 1 m^2. The smooth parabolic shape utilized to simulate heliostats in ASAP® does not portray this concentration limitation, as depicted in Figure 4.14. Breault Research Organization, the developers of ASAP®, are aware of the internal register limitations in modeling the NCSETF. Future releases of the software may look to accommodate the input of additional variables, allowing more realistic non-imaging heliostats to be simulated within the model.

Model improvements should be targeted towards simulating the focusing characteristics of true non-imaging heliostats as presented by Chen [33]. One way to accomplish this may be to export the optical geometry on an hourly basis to a Computer Aided Design (CAD) environment, and then import the geometry into ASAP® via the ASAP® Initial Graphics Exchange Specifications (IGES) translator smartIGES™. Although a very tedious process, it may not require the assignment of all the variables as implemented in this thesis. It would, however, require the additional step of creating a CAD drawing for each of the simulated hours. Implementation of such an improvement would allow for an even more realistic performance of the NCSETF to be demonstrated.

5.3 Future System Analysis

Future system analysis should be focused around modifications of the optical geometry. The most significant analysis should be targeted towards optimization of the heliostat field layout. The NCSETF model was developed to accommodate a variety of conditions. The programming approach to the development of the model was to make it both versatile and robust. As a result, the optical geometry of the system can easily be modified and the effects realized. Future work should examine modifications of optical geometry parameters such as heliostat dimensions, heliostat field layouts, and down beam reflector heights as well as orientations. Additionally, the effects of varying focal points should also be investigated.

The simulations presented assume the pointing accuracies of the heliostats are 100%. In real world applications a pointing accuracy of 100% is not realistically achievable. Wind gusts for example can cause the orientations of the heliostat to fluctuate. Future system analysis should incorporate a margin of error for the achievable pointing accuracies, and the subsequent effects on concentration and spot shape should be analyzed. Furthermore, the impact of the actual tower structure on the optical performance of the facility due to the effects of shading and blocking should also be explored. When a final depiction of the tower is developed, this can be accomplished utilizing the ASAP® smartIGES™ translator to import a CAD representation of the tower into the ASAP® simulations.

APPENDIX A

NOMENCLATURE

AP	aim point
ceil	rounding operator to round up to the nearest day integer
DNI	direct normal irradiance (W/m^2)
D_{tx}	distance from heliostat to target along x-axis (m)
f_e	fractional position of the ellipsoidal upper vertex to the aim point (m)
f_h	fractional position of the vertex of the hyperboloid from the height of the aim point (m)
f_1	distance from the tower reflector to the aim point (m)
f_2	distance from the tower reflector to the secondary concentrator (m)
H_a	heliostat azimuth angle (˚)
HF_L	heliostat field length (m)
HF_W	heliostat field width (m)
hour	array containing the number of hours in the month selected for simulation
H_{xc}	heliostat center x-axis coordinate (m)
H_{yc}	heliostat center y-axis coordinate (m)
H_z	heliostat zenith angle (˚)
H_{zc}	heliostat center z-axis coordinate (m)
I_a	common intermediate angle (˚)
index	base parameter establishing the number of days in the year up to the time of the specified month
I_z	angle between the target and the sun (˚)
L_{fac}	heliostat facet length (m)

L_m	length of the heliostat mirror (m)
month	selected simulation month
n	array containing the day of the year for every hour of the month simulated
N_{helios}	number of heliostats in field
NL_{helios}	number of heliostat rows
NW_{helios}	number of heliostat columns
R	arbitrary simulation sun source distance (m)
RC	receiver concentrator
R_{ha}	angle of rotation to achieve heliostat azimuth angle in ASAP (˚)
R_{hz}	angle of tilt to achieve heliostat zenith angle in ASAP (˚)
R_{max}	maximum last row distance of heliostats in field (m)
R_{min}	minimum first row distance of heliostats in field (m)
R_{space}	heliostat row spacing (m)
S_{AD}	angular diameter of the sun (0.5˚)
S_h	selected simulation hour
S_{HAR}	half angle of the sun (radians)
S_r	radius of the elliptical grid sun source (m)
$SUN_{Diameter}$	diameter of image of the sun on the detector produced by a single heliostat (m)
T_a	target azimuth angle (˚)
T_{arot}	angle of rotation to achieve target position vector (˚)
TR	tower reflector
T_{tilt}	angle of tilt to achieve target position vector (˚)
T_{xc}	target center x-axis coordinate (m)
T_{yc}	target center y-axis coordinate (m)

T_z	target zenith angle (˚)
T_{zc}	target center z-axis coordinate (m)
V_{radC}	vertex radius of curvature (m)
W_{fac}	heliostat facet width (m)
W_m	width of heliostat mirror (m)
δ	declination of the sun (˚)
δ_{min}	minimum declination of the sun (˚)
ω	hour angle (˚)
φ	latitude (˚)
ϕ	longitude (˚)
α_{sm}	minimum elevation angle at solar noon (˚)
α_s	solar altitude angle (˚)
γ_s	solar azimuth angle (˚)
θ_z	solar zenith angle (˚)

APPENDIX B

SPO Algorithm

Input: ϕ, φ, S_h, month, DNI

Step 1:

```
if (month = January)
    data = csvread ('January_DNI.csv')
     index = 0;

else if (month = February)
    data = csvread ('February_DNI.csv')
    index = 31;

else if (month = March)
    data = csvread ('March_DNI.csv')
    index = 59;

else if (month = April)
    data = csvread ('April_DNI.csv')
    index = 90;

else if (month = May)
    data = csvread ('May_DNI.csv')
    index = 120;

else if (month = June)
    data = csvread ('June_DNI.csv')
    index = 151;

else if (month = July)
    data = csvread ('July_DNI.csv')
    index = 181;

else if (month = August)
    data = csvread ('August_DNI.csv')
    index = 212;

else if (month = September)
    data = csvread ('September_DNI.csv')
    index = 243;

else if (month = October)
    data = csvread ('October_DNI.csv')
```

```
        index = 273;

else if (month = November)
        data = csvread ('November_DNI.csv')
        index = 304;

else if (month = December)
        data = csvread ('December_DNI.csv')
        index = 334;
```

Step 2:

```
hour = 1: length(data);

$n = \text{index} + \text{ceil}\left(\frac{\text{hour}}{24}\right);$

$B = (n-1)\left(\frac{360}{365}\right);$

$\delta = \left(\frac{180}{\pi}\right)(0.006918 - 0.399912\cos(B) + 0.070257\sin(B) - 0.006758\cos(2B)$
        $+ 0.000907\sin(2B) - 0.002697\cos(3B)0.00148\sin(3B));$
```

Step 3:

```
$\omega = -180 + 15(\text{hour} - 24(n - (\text{index} + 1)));$

$\theta_z = \cos^{-1}\left(\cos(\phi)\cos(\delta)\cos(\omega) + \sin(\phi)\sin(\delta)\right);$
```

Step 4:

```
for i = 1:length($\omega$)
    if $\omega$(i) < 0
        $\gamma_s = -\left|\cos^{-1}\left(\frac{\cos(\theta_z)\sin(\phi) - \sin(\delta)}{\sin(\theta_z)\cos(\phi)}\right)\right|;$
    else
        $\gamma_s = \left|\cos^{-1}\left(\frac{\cos(\theta_z)\sin(\phi) - \sin(\delta)}{\sin(\theta_z)\cos(\phi)}\right)\right|;$
    end
end
```

Output: DNI, hour, δ , $\theta_{\mathrm{z}}\left(\mathrm{S_h}\right)$, $\gamma_{\mathrm{s}}\left(\mathrm{S_h}\right)$

APPENDIX C

HROPV Algorithm

```
Input:  $\theta_z, \gamma_s, S_h, N_{helios}, H_{xc}, H_{yc}, H_{zc}, T_{xc}, T_{yc}, T_{zc}$

Step 1:
    For $i = 1 : N_{helios}$
        $D_{tx}(i) = H_{xc}(i) - T_{xc}$;

    Step 2:
        if $H_{zc}(i) = 0$
            $T_t(i) = \tan^{-1}\left(\frac{T_{yc}}{H_{xc}(i) - T_{xc}}\right)$;
            $V_{radC}(i) = 2\sqrt{T_{yc}^{2} + \left(H_{xc}(i) - T_{xc}\right)^{2}}$;
        else
            $L_s(i) = \sqrt{H_{zc}(i)^{2} + \left(H_{xc}(i) - T_{xc}\right)^{2}}$;
            $T_t(i) = \tan^{-1}\left(\frac{T_{yc}}{L_s(i)}\right)$;
            $V_{radC}(i) = 2\sqrt{T_{yc}^{2} + \left(L_S(i)\right)^{2}}$;
        end

    Step 3:
        $T_z(i) = 90 - T_t(i)$;
        $T_{tilt}(i) = -T_t(i)$;

    Step 4:
        if $H_{zc}(i) = 0$
```

```
        $T_a(i) = 0;$
        $T_{arot}(i) = 0;$
    else if $H_{zc}(i) > 0$
        $T_a(i) = \tan^{-1}\left(\frac{H_{zc}}{D_{tx}(i)}\right);$
        $T_{arot}(i) = 90 - T_a(i);$
    else
        $T_a(i) = \tan^{-1}\left(\frac{H_{zc}}{D_{tx}(i)}\right);$
        $T_{arot}(i) = -[90 + T_a(i)];$
    end
```

Step 5:

```
    for j = 1:length(hour)
$I_z(j,i) = \cos^{-1}\left(\cos(\theta_z(j))\cos(T_z(i)) + \sin(\theta_z(j))\sin(T_z(i))\cos(\gamma_s(j) - T_a(i))\right);$
        $I_a = \sin^{-1}\left(\sin(\theta_z(j))\frac{\sin(\gamma_s(j) - T_a(i))}{\sin(I_z(j,i))}\right);$
```

Step 6:

```
$H_z(j,i) = \cos^{-1}\left(\cos(T_z(i))\cos\left(\frac{I_z(j,i)}{2}\right) + \sin(T_z(i))\sin\left(\frac{I_z(j,i)}{2}\right)\cos(I_a(j,i))\right);$
        $H_a(j,i) = \sin^{-1}\left(\sin\left(\frac{I_z(j,i)}{2}\right)\frac{\sin(I_a(j,i))}{\sin(H_z(j,i))}\right) + T_a(i);$
    end
```

```
    Step 7:
        $R_{hz}(S_h, i) = -90 + H_z(S_h, i)$;
        $R_{ha}(S_h, i) = -H_a(S_h, i)$;
    end
Output: $R_{hz}(S_h)$, $R_{ha}(S_h)$, $V_{radC}$
```

APPENDIX D

NSCHFL Algorithm

```
Input: $\phi$, $\delta_{\min}$, $R_{\min}$, $R_{\max}$, $L_m$, $L_{fac}$, $W_m$, $W_{fac}$

Step 1:
    $\alpha_{sm} = 90 - \phi + \delta_{\min};$
    $R_{space} = \frac{L_m}{\tan(\alpha_{sm})};$

Step 2:
    $HF_L = R_{\max} - R_{\min};$
    $HF_W = HF_L;$

Step 3:
    $N_{helios} = \mathrm{floor}\left(\frac{HF_L}{R_{space}}\right);$
    $NW_{helios} = \mathrm{floor}\left(\frac{HF_W}{W_m}\right);$

Step 4:
    $H_{zp}(1) = -\left(\frac{HF_W}{2}\right);$
    $H_{xp}(1) = R_{\min};$

Step 5:
    for i = 2: $NW_{helios}$
        $H_{zp}(i) = H_{zp}(i-1) + W_m;$
```

```
    end
```

Step 6:

```
    for j = 2: $NL_{helios}$
        $H_{xp}(j) = H_{xp}(j-1) + R_{space}$;
    end
```

Step 7:

```
    for i = 1: $NW_{helios}$
        for j = 1: $NL_{helios}$
            $H_{zc}(i,j) = H_{zp}(i)$;
        end
    end
```

Step 8:

```
    for j = 1: $NL_{helios}$
        for i = 1: $NW_{helios}$
            $H_{xc}(i,j) = H_{xp}(j)$;
            $H_{yc}(i,j) = 0$;    (Assuming heliostats placed at ground level to limit import parameters)
        end
    end
```

Step 9:

```
    $H_{xc}$ = reshape [$H_{xc}$, 1 row];
```

```
        $H_{xc}$ = reshape [$H_{xc}$ , 1 row];
        $H_{xc}$ = reshape [$H_{xc}$ , 1 row];
**Output:**  $L_{m}$ , $L_{fac}$ , $W_{m}$ , $W_{fac}$ , $H_{xc}$ , $H_{yc}$ , $H_{zc}$
```

REFERENCES

[1] King, Sir David. Foreword. *Future Energy*. By Goodwin A.R.H., et al. Amsterdam, Netherlands: Elsevier, 2008. Print.

[2] Hsieh, Jui Sheng. Introduction. *Solar Energy Engineering.* Englewood Cliffs, NJ: Prentice-Hall, Inc., 1986. Print.

[3] "CSP – How it Works." *Solar Power and Chemical Energy Systems.* Web. 4 Apr. 2010. <http://www.solarpaces.org/CSP_Technology/csp_technology.htm>.

[4] "Concentrating Solar Power Prospects of the Southwest United States." *Concentrating Solar Power Resource Maps.* National Renewable Energy Laboratory (NREL). Web. 4 Apr. 2010. < http://www.nrel.gov/csp/maps.html>.

[5] "Concentrating Solar Power." *Solar Energy Technologies Program.* U.S. Department of Energy. Web. 4 Apr. 2010. <http://www1.eere.energy.gov/solar/csp_program.html>.

[6] "Concentrating Solar Power." *Solar Energy Technologies Program.* U.S. Department of Energy and National Renewable Energy Laboratory (NREL), 2010. Web. 4 Apr. 2010. < http://www1.eere.energy.gov/solar/pdfs/47281.pdf>.

[7] "Green Energy – Microtherm® Insulation in Concentrated Solar Power (CSP)." *High Temperature Insulation.* Microtherm Thermal Insulation Solutions, 2011. Web. 9 Apr. 2010. < http://www.microtherm.uk.com/high/EXEN/site/concentrated-solar-power.aspx>.

[8] "Linear Concentrator Solar Power Plant Illustration." *Solar Multimedia.* U.S. Department of Energy and National Renewable Energy Laboratory, 1996. Web. 9 Apr. 2010. <https://www.eeremultimedia.energy.gov/solar/graphics/linear_

concentrator_solar_power_plant_illustration>.

[9] "Linear Fresnel Diagram." *Concentrating Solar Power Technologies 1: Introduction to Alternatives.* Bright Hub Inc. Web. 9 Apr. 2010. < http://www.brighthub.com/environment/renewable-energy/articles/65170/image/67188/>.

[10] "Dish/Engine Systems for Concentrating Solar Power." *Energy Basics, Renewable Energy.* U.S. Department of Energy. Web. 9 Apr. 2010. < http://www.eere.energy.gov/basics/renewable_energy/dish_engine.html>.

[11] Pye, J. "Concentrating Solar Power Systems." *The Australian National University Solar Thermal Group* (2010). Web. 27 Apr. 2010. < http://solar-thermal.anu.edu.au/high-temperature/concentrating-solar-power-systems/>.

[12] "Power Tower Systems for Concentrating Solar Power." *Energy Basics, Renewable Energy.* U.S. Department of Energy. Web. 8 May 2010. < http://www.eere.energy.gov/basics/renewable_energy/power_tower.html>.

[13] Stine, William B., and Michael Geyer. Central Receiver Systems. *Power from the Sun.* Power From The Sun.net, 2001. Web. 8 May 2010. < http://www.powerfromthesun.net/Book/chapter10/chapter10.html>.

[14] Kolb, Gregory J., et al. "Heliostat Cost Reduction Study." *Sandia National Laboratories.* (2007): 1-158. Print.

[15] Rabl, Ari. "Tower Reflector for Solar Power Plant." *Solar Energy.* 18 (1976): 269-271. Print.

[16] Yogev, A., et al. "Solar 'Tower Reflector' Systems: a New Approach for High-Temperature Solar Plants." *Int. J. Hydrogen Energy.* 23.4 (1998): 239-245. Print.

[17] Segal, Akiba, and Michael Epstein. "The Optics of the Solar Tower Reflector." *Solar Energy*. 69(Suppl.) (2000): 229-241. Print.

[18] Garty, Haim, and Michael Epstein. "Solar Research Facilities Unit." *Scientific Activities: Solar Research Facilities.* Weizmann Institute of Science, 2010. Web. 15 Jul. 2010. <http://www.weizmann.ac.il/acadaff/Scientific_Activities/2010/Solar_Research_Facilities.html>.

[19] Epstein, Michael. "Beam-Down Tower System." *Weizmann Institute of Science, Solar Research Facilities Unit.* (2008). Power Point Presentation.

[20] Debesh, Terry. "The Canadian Institute for the Energies and Applied Research." *Center for Energy Research.* Weizmann Institute of Science, 2011. Web. 16 Mar. 2011. < http://www.weizmann.ac.il/weizsites/solarenergy/>.

[21] Chhabara, Rajesh. "CSP Innovation: Technologies that crash the cost barrier." *CSP Today*, 1 April 2010. Web. 19 Jun. 2010. <http://social.csptoday.com/industry-insight/csp-innovation-technologies-crash-cost-barrier>.

[22] Prior, B. "A Small Concentrating Solar 100kW Demo Site (beam-down technology)." *Masdar Visit: Solar Projects in Abu Dhabi.* Greentech Media, Inc., 2011. Web. 16 Mar. 2011. <http://www.greentechmedia.com/articles/read/update-on-the-masdar-initiative-from-abu-dhabi/>.

[23] Tamaura, Yutaka, et al. "A Novel Beam-Down System for Solar Power Generation with Multi-Ring Central Reflectors and Molten Salt Thermal Storage." *Tokyo Institute of Technology, Research Center for Carbon Recycling and Energy.* 1-8. Web. 5 Nov. 2010. <ftp://ftp.crs4.it/pub/References/SolarPaces2006/A5/A5-S2-TAMAURA.pdf>.

[24] Garcia, Pierre, Alain Ferriere, and Jean-Jacques Bezian. “Codes for Solar Flux Calculation Dedicated to Central Receiver System Applications: a Comparative Review.” *Solar Energy*. 82 (2008): 189-197. Print.

[25] “Cosine loss.” *Cheap, Open Source Heliostats.* 14 Nov. 2010. Web. 14 Dec. 2010. <http://www.heliostats.org/2010/11/cosine-loss.html>.

[26] Stine, William B., and Michael Geyer. The Sun’s Energy. *Power from the Sun.* Power From The Sun.net, 2001. Web. 8 May 2010. < http://www.powerfromthesun.net/Book/chapter02/chapter02.html>.

[27] Breault Research Organization, Inc. *The ASAP Primer*. Tucson, AZ: Breault Research Organization, Inc., 2006. Web. 15 Nov. 2010. <http://www.uotek.com.tw/usgs1/store/F3/Primer_English.pdf>.

[28] Wilcox, S. and W. Marion. *Users Manual for TMY3 Data Sets.* National Renewable Energy Laboratory (NREL), 2008. Web. 14 Dec. 2010. <http://www.nrel.gov/docs/fy08osti/43156.pdf>.

[29] Duffie, John A., and William A. Beckman. *Solar Engineering of Thermal Processes.* 3rd ed. Hoboken, NJ: John Wiley & Sons, Inc., 2006. Print.

[30] “Renewable Energy Resources.” *3M United States: Products, Brands and Technologies.* 3M, 2011. Web. 16 Mar. 2011. <http://solutions.3m.com/wps/portal/3M/en_US/Renewable/Energy/Resources/Press_Releases/?PC_7_RJH9U52308NR50I0NISNKB32G3_assetId=1273668905876>.

[31] Leonard, Timothy M. *Heliostat Reflection Equations.* New Mexico: Enhancement Electronics, Inc., 2003. Print.

[32] Weisstein, Eric W. “Spherical Trigonometry.” *Wolfram MathWorld.* Wolfram Research, Inc., 2011. Web. 19 Feb. 2011. < http://mathworld.wolfram.com/SphericalTrigonometry.html>.

[33] Chen, Y.T., et al. “Non-Imaging, Focusing Heliostat.” *Solar Energy*. 71.3 (2001): 155-164. Print.

[34] Siala, F.M.F. and M.E. Elayeb. “Mathematical Formulation of a Graphical Method for a No-Blocking Heliostat Field Layout.” *Renewable Energy.* 23 (2001): 77-92. Print.

[35] Sanchez, Marcelino, and Manuel Romero. “Methodology for Generation of Heliostat Field Layout in Central Receiver Systems Based on Yearly Normalized Energy Surfaces.” *Solar Energy.* 80 (2006): 861-874. Print.

[36] Falcone, P.K. *A Handbook for Solar Central Receiver Design.* Sandia National Laboratories, 1986. Print.

[37] “Coma, Optical.” *The Encyclopedia of Science Optics & Optical Phenomena.* Web. 8 Sept. 2011. < http://www.daviddarling.info/encyclopedia/C/coma_optical.html>.

[38] Steinfeld, Aldo, and Robert Palumbo. “Solar Thermochemical Process Technology.” *Encyclopedia of Physical Science & Technology.* 15 (2001): 237-256. Print.

VITA

Graduate College
University of Nevada, Las Vegas

Ryan J. Hoffmann

Degree:
Bachelor of Science, Computer Science and Mathematics, 2008
University of Montana

Thesis Title: Modeling of a Novel Solar Down Beam Test Facility Utilizing Newtonian Optics

Thesis Examination Committee:
Chairperson, Dr. Yitung Chen, PH. D.
Committee Member, Dr. Robert Boehm, PH. D.
Committee Member, Dr. Suresh B. Sadineni, PH. D.
Graduate Faculty Representative, Dr. Allen Johnson, PH. D.